Phase space analysis of inclusive charged current proton production in MicroBooNE

by

Munerah Alrashed

B.S., King Faisal University, 2008

M.S., King Faisal University, 2013

AN ABSTRACT OF A DISSERTATION

submitted in partial fulfillment of the
requirements for the degree

DOCTOR OF PHILOSOPHY

Department of Physics
College of Arts and Sciences

KANSAS STATE UNIVERSITY
Manhattan, Kansas

2019

Abstract

Using the full five-dimensional phase space, measuring the relative fraction of ν_μ charged current events containing a proton in the final state originates from quasielastic, $2p2h$, resonance, and deep inelastic sub-nuclear scattering processes within the context of the GENIE cross section model. These studies indicate that the data support the picture that charged current scattering is dominated by a relatively small number of incoherent nucleon-level processes. GENIE successfully predicts, within the estimated experimental uncertainties, the relative contributions of each subnuclear process. This analysis of MicroBooNE data establishes the presence of a $2p2h$ contribution to the cross section to a significance of 7.3 σ.

Phase space analysis of inclusive charged current proton production in MicroBooNE

by

Munerah Alrashed

B.S., King Faisal University, 2008

M.S., King Faisal University, 2013

A DISSERTATION

submitted in partial fulfillment of the
requirements for the degree

DOCTOR OF PHILOSOPHY

Department of Physics
College of Arts and Sciences

KANSAS STATE UNIVERSITY
Manhattan, Kansas

2019

Approved by:

Major Professor
Tim Bolton

Copyright

Abstract

Using the full five-dimensional phase space, measuring the relative fraction of ν_μ charged current events containing a proton in the final state originates from quasielastic, $2p2h$, resonance, and deep inelastic sub-nuclear scattering processes within the context of the GENIE cross section model. These studies indicate that the data support the picture that charged current scattering is dominated by a relatively small number of incoherent nucleon-level processes. GENIE successfully predicts, within the estimated experimental uncertainties, the relative contributions of each subnuclear process. This analysis of MicroBooNE data establishes the presence of a $2p2h$ contribution to the cross section to a significance of 7.3 σ.

Contents

List of Figures

List of Tables

Acknowledgments

I would like to express my deepest appreciation to my advisor Prof. Bolton for his patience, motivation, and immense knowledge. His guidance helped me all the time. His motivation gave me the energy to do something better. I have learned a lot from him, I came to Kansas State University with a good physics background. However, he taught me how and when I can use this existing knowledge. This work would not have been possible without his efforts.

A special thanks go to my parents, my brothers and my sisters for supporting me along the path to my Ph.D.

Dedication

To my parents

Chapter 1

Introduction

This thesis presents an analysis of inclusive muon neutrino charged current proton production (ν_μCC-p) from neutrino scattering on argon nuclei at the MicroBooNE liquid argon time projection chamber (LArTPC) experiment. The MicroBooNE experiment is operating at the Fermilab Booster Neutrino Beam (BNB) with a mean ν_μ energy of 800 MeV. The analysis consists of a comparison of MicroBooNE data to predictions from the GENIE event generator[1] over the full five-dimensional phase space of the muon-leading proton final state, where "leading" refers to the highest kinetic energy (KE) in the events where multiple protons are present.

Next-generation neutrino experiments (such as DUNE[2, 3, 4] and HyperK[5]) seek to determine subtle properties of neutrinos that depend on differences in the oscillation properties of neutrinos and antineutrinos. Other such experiments (for example, the SBN program at Fermilab[6]) test the consistency of the three-generation model of neutrinos embedded in the mixing matrix. A crucial tool in these endeavors is a high fidelity map between neutrino energy, the quantity most directly encodes oscillation phenomena, and the observable energy in the neutrino detector. This map typically incorporates detailed models of the neutrino beam flux, the neutrino detector response, and the neutrino interaction model.

Practical needs dictate the use of heavy nuclei in detectors, and neutrino energies needed to observe oscillations lie in the $0.2 - 5$ GeV energy range, These considerations imply that interaction models must be constructed as convolutions of phenomenological sub-models of neutrino-nucleon scattering and of nuclear medium effects, which are typically implemented as Monte Carlo event generators.

The DUNE and SBN LArTPC experiments employ almost exclusively the GENIE event generator. While GENIE has been validated and tuned with a number of measurements from the T2K, Minerνa, and MiniBooNE experiments, which predominantly employ carbon targets, only limited tests have been performed to date using neutrino-argon scattering. The present thesis adds a further test of GENIE's

modeling of scattering from argon by examining inclusive charged-current proton production at MicroBooNE. It takes particular advantage of the high LArTPC acceptance to examine, for the first time, this final state over its full five-dimensional phase space.

1.1 Outline of Thesis

The work in this present thesis is structured as follows: Chapter 2 presents an overview of neutrino physics and neutrino oscillations. Then, Chapter 3 discusses the neutrino interactions. Next, Chapter 4 describes the MicroBooNE detector and its main components, which are used for the measurements. After that, Chapter 5 discusses the Booster Neutrino Beam (BNB) and briefly describes the Booster proton beam, its target, and its composition. Next, Chapter 6 discusses event reconstruction. Then, Chapter 7, the core of my thesis, presents inclusive ν_μ charged current proton production (ν_μCC-p). Systematic uncertainties are estimated in Chapter 8. Finally, Chapter 9 summarizes the results.

Chapter 2

Neutrino Physics and Oscillations

Neutrinos are of fundamental importance. This Chapter reviews the remarkable physics of neutrino particles and their role in the standard model (SM) of elementary particle physics in Section 2.1. An introduction to the neutrino oscillations concept is offered in Section 2.2.

2.1 Introduction to Neutrinos

The neutrino was envisaged by Pauli in December 1930 to explain the energy spectrum of β-decay, in which a neutron decays into a proton and an electron. The electron energy spectrum of this decay was observed to be continuous experimentally, although the conservation of energy and momentum would require the electron energy to have a fixed value,

$$E = \frac{m_A^2 - m_{A'}^2 + m_{e^-}^2}{2m_A}, \tag{2.1}$$

where m_A, $m_{A'}$, and m_{e^-} are the parent nuclear mass, the daughter nuclear mass, and the electron mass, respectively. E is monoenergetic in the equation above [1]. Thus, the nuclear β-decay process could not be explained by the emission of an electron by a parent nucleus. Therefore, the conservation rules governing the momentum and energy of the initial and final particles seemed to be violated in the β-decay.

Pauli proposed that under the condition of energy-momentum conservation the only possibility to explain the conundrum of radioactive beta decay, was to assume that there exists a neutral light particle emitted in the β-decay together with the electron, accounting for the anomalous energy spectrum [11, 12, 13]. The next fundamental contribution to improve the idea of the neutrino was made by Fermi, who put forward a theory of β-decay in 1934 [9], explaining the experimental observations successfully.

In the SM, neutrinos are massless, and they carry a lepton quantum number and have no electric charge. Since the neutrino is electrically neutral, the question arises whether the neutrino has a distinct

[1] This present thesis employs the system of units $\hbar = c = 1$.

antiparticle, "Dirac", or neutrino is an own antiparticle, "Majorana". In brief, the main difference between Dirac and Majorana particles is that the Dirac case is realized when there exists a lepton charge carried by the neutrinos, conserved by the particle interactions, while massive neutrinos can be Majorana particles if their interactions violate lepton number [14].

Neutrinos in the SM of electroweak interactions are left-handed partners of the charged leptons doublets under SU(2) symmetry.

$$\nu_{L\ell} = \begin{pmatrix} \nu_\ell \\ \ell \end{pmatrix}, \tag{2.2}$$

where $\ell = e$, μ, τ, which identify charged leptons. Here, left-handed referrs to chirality state of a lepton, which is correlated with the projection of lepton spin along the lepton direction of motion. Neutrinos experience charged current (CC) interactions via an exchange of a $W^{\pm}$ boson, which in the SM is described by the Lagrangian [38],

$$\mathcal{L}_{cc} = -\frac{g}{2\sqrt{2}} \sum_{\ell} W_{\mu}^{+} \overline{\nu}_{L\ell} \gamma^{\mu} (1 - \gamma^{5}) \ell^{-} + h.c, \tag{2.3}$$

where g is the gauge coupling constant. Also, neutrinos can interact weakly via the exchange of a Z^0 boson, neutral current interactions.

In 1956, the neutrino was first experimentally detected by Reines and Cowan. Since then it has been extensively investigated by different experiments.

2.2 Neutrino Oscillations

The observable transformation of one neutrino type, or "flavor" into another, after traveling the distance, is called "neutrino oscillation". The oscillation phenomena arises from mixing between the flavor and mass eigenstates of neutrinos, which indicates neutrinos have mass and non-zero mixing. Neutrino oscillations was investigated in long-baseline neutrino experiments in Japan and the USA. The first strong evidence of neutrino flavor transformation was obtained by the Super-Kamiokande (Super-K) experiment [15], then SNO1 [16], and SNO2 [17] experiments, although Ray Davis's Homestake experiment was the first experiment observed the effects of neutrino oscillation. Moreover, other neutrinos sources such as atmosphere, nuclear reactors, and particle accelerators have all been found to exhibit neutrino flavor oscillation. The theoretical possibility, the concept of neutrino mixing was first suggested by Pontecorvo, who imagined that a massive neutrino could oscillate in time over distance into its own anti-particle[18].

The neutrino flavor eigenstates can be written as a linear superposition of the eigenstates of the total Hamiltonian (mass eigenstates) as follows,

$$\nu_\ell = \sum_\ell U_{\ell i} \nu_i, \tag{2.4}$$

where ν_ℓ is a flavor eigenstate with flavor ℓ, ν_i is a mass eigenstate i, and U is the unitary mixing matrix, called the Pontecorvo, Maki, Nakagawa, and Sakata (PMNS) matrix.

If there are only two neutrino oscillations, the mixing matrix is given by

$$U_{\ell i} = \begin{pmatrix} \cos\theta & \sin\theta \\ -\sin\theta & \cos\theta \end{pmatrix}, \tag{2.5}$$

where θ is the mixing angle.

Then, the probability for $|\nu_\ell\rangle$ to $|\nu_\beta\rangle$ transitions is given by,

$$P_{(|\nu_\ell\rangle \to |\nu_\beta\rangle)} = \sin^2 2\theta \sin^2(1.27\frac{\Delta m^2 L}{E_\nu}), \tag{2.6}$$

where Δm^2 is the neutrino mass difference in eV^2, L is the distance traveled by the neutrino in km, and E is the neutrino energy in GeV, while the appearance probability is as follows

$$P_{(|\nu_\ell\rangle \to |\nu_\ell\rangle)} = 1 - \sin^2 2\theta \sin^2(1.27\frac{\Delta m^2 L}{E_\nu}). \tag{2.7}$$

If there are three neutrino oscillations, the three neutrino mixing matrix is given by

$$U_{\alpha i} = \begin{pmatrix} 1 & 0 & 0 \\ 0 & c_{23} & s_{23} \\ 0 & -s_{23} & c_{23} \end{pmatrix} \begin{pmatrix} c_{13} & 0 & s_{13}e^{-i\delta} \\ 0 & 1 & 0 \\ -s_{13}e^{-i\delta} & 0 & c_{13} \end{pmatrix} \begin{pmatrix} c_{12} & s_{12} & 0 \\ -s_{12} & c_{12} & 0 \\ 0 & 0 & 1 \end{pmatrix}, \tag{2.8}$$

where $c_{ij} = \cos\theta_{ij}$, $s_{ij} = \sin\theta_{ij}$, θ_{ij} are the mixing angles, δ are the conjunction parity (CP)-violating phases δ_{CP}. Here, in the first matrix, the mixing angle θ_{23} is relevant for oscillations of atmospheric neutrinos, approximately 45° [62], in the second matrix, the mixing angle θ_{13} is relevant for a reactor neutrino experiment at short baselines, approximately 9° [64], and in the third matrix, the mixing angle θ_{12} is relevant for solar neutrino oscillations, approximately 33.9° [63]. In the second matrix, if neutrino oscillation violates CP symmetry, the factor δ_{CP} is non-zero. A non-zero δ_{CP} has not yet been observed. DUNE and HyperK will mainly address the issue of CP-violation.

Chapter 3

Neutrino Interactions

Understanding neutrino interactions with matter is of critical importance in precision neutrino oscillation experiments. This Chapter discusses briefly the impact of nuclear environment effects in Section 3.1 and in details, the most important neutrino interactions of neutrino-nucleon scattering at the MicroBooNE energy regime: quasielastic charged-current (QE) interaction in Section 3.3, resonance production (RES) in Section 3.4, charged-current deep inelastic scattering (DIS) in Section3.5, and two nucleons correlated process (MEC) in Section 3.6.

3.1 The Nuclear Environment Effect

Neutrinos interact with bound nucleons within a nuclear target, so that leads to arising uncertainties from a variety of nuclear environmental effects. Generally, nuclear effects can be classified into initial state effects and final state effects.

1. Initial state effects arise due to the fact Fermi motion, which causes fluctuations in the initial kinematics.

2. Final state effects arise due to that the hadronic final states produced inside a nuclear medium being propagated through the nuclear medium undergoing Fermi motion. They experience collisions before exiting. Therefore, both their kinematics and identity can be altered [61].

These nuclear effects are present in different channels for all nuclei, which results in challenges to understand each of these channels as discussed briefly in Sections 7.1-8.3.

3.2 Moun-Proton Kinematics

In the case of at least one proton and one muon in the final state and neglecting nuclear environment effects five kinematics can be characterized completely the final state. For example, the following can be

used to identify the momentum vectors:

- The muon kinetic energy T_μ;
- The muon scattering angle variable $\cos\theta_\mu$;
- The proton kinetic energy T_p;
- The proton scattering angle variable $\cos\theta_p$;
- The difference in the muon azimuthal angle and the proton azimuthal angle $\Delta\varphi_{\mu p} = \varphi_\mu - \varphi_p$.

Only the azimuthal angle difference appears because of the cylindrical symmetry of the neutrino beam.

The neutrino energy can be evaluated from the lepton and hadron energies observable in the final state after the neutrino has interacted. Figure 3.1 shows the true neutrino energy for different neutrino modes as described in the following sections, from the simulations for beam-induced neutrino interactions in the MicroBooNE experiment.

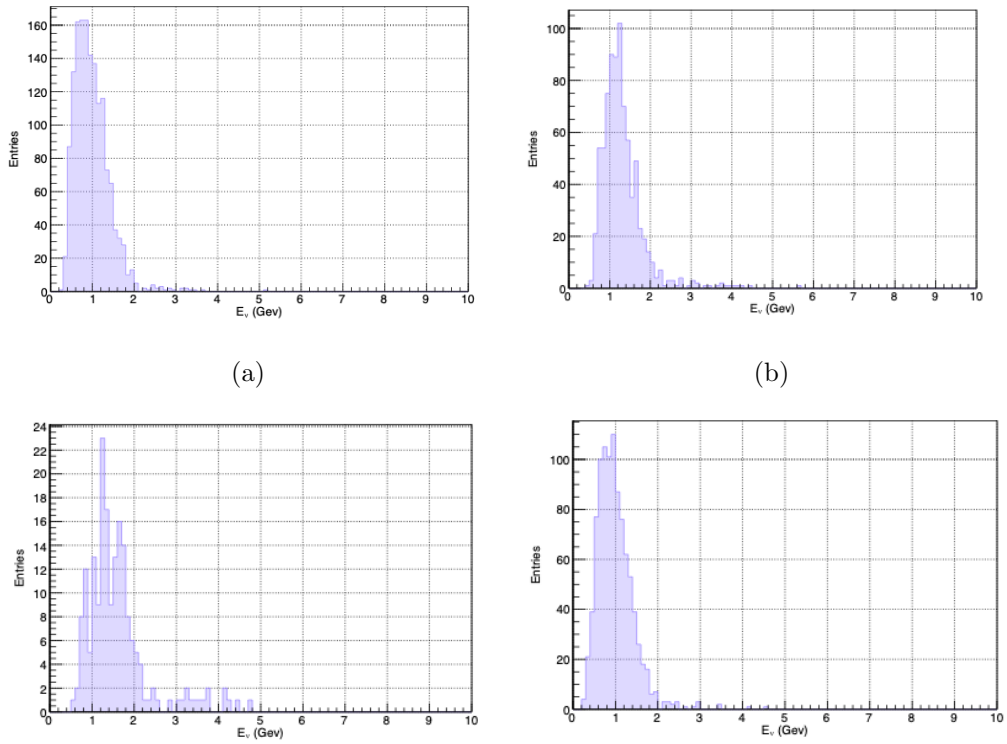

Figure 3.1: True neutrino energy with different neutrino modes: (a) QE, (b) RES, (c) DIS, and (d) MEC interactions.

3.3 Quasi-Elastic Interactions

For neutrino energies less than ∼2 GeV, neutrino-nucleon interactions are dominated by QE scattering. In a charged current neutrino QE interaction, the target neutron is converted to a proton.

$$\nu_\ell n \to \ell^- p, \tag{3.1}$$

In the case of an antineutrino scattering, the target proton is converted into a neutron.

$$\overline{\nu_\ell} p \to \ell^+ n, \tag{3.2}$$

where ℓ is a lepton flavor, n is a neutron and p is a proton. An example of QE event topology in MicroBooNE experiment is displayed in Fig. 3.2.

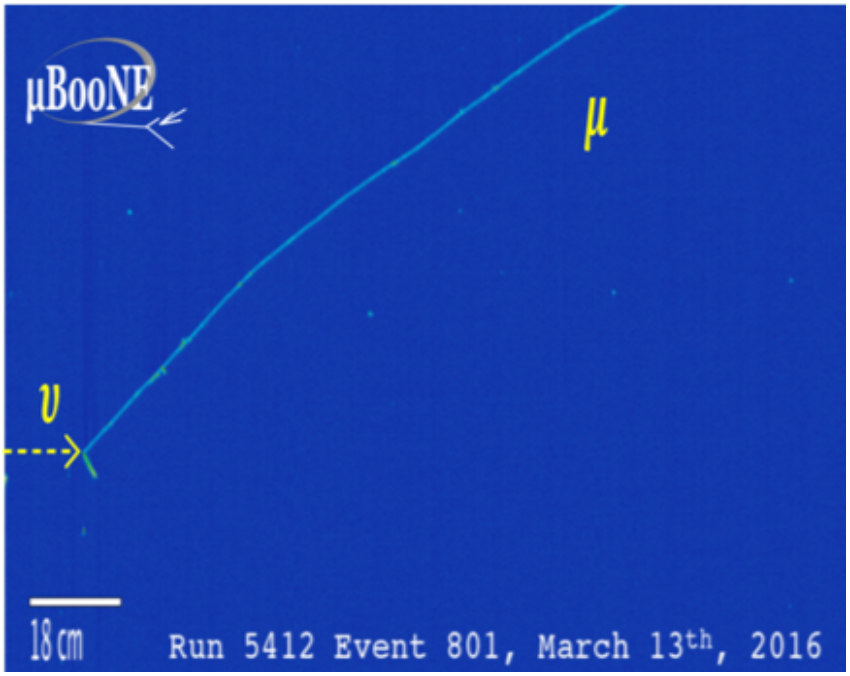

Figure 3.2: Shows the event display of the collection plane with ν_μ CC QE candidate event from the MicroBooNE experiment [47].

Neutrinos can elastically scatter off an entire nucleon liberating a nucleon from the target [50] rather than its constituent partons, creating a hole in the remnant nucleus. Accordingly, the name of this process is 1p-1h (one particle, one hole). Figure 3.3 shows a Feynman diagram for QE interactions.

The simulation used in this thesis employs the GENIE neutrino generator, set up with the Llewellyn-Smith parameterization for the CCQE interactions [39] the relativistic Fermi gas (RFG) model for the

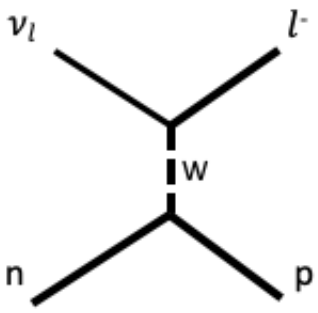

Figure 3.3: Feynman diagram for QE interactions.

nucleus [40]. Figure 3.4 shows the reconstruction of a simulated 500-MeV CC ν_μ quasi-elastic interaction.

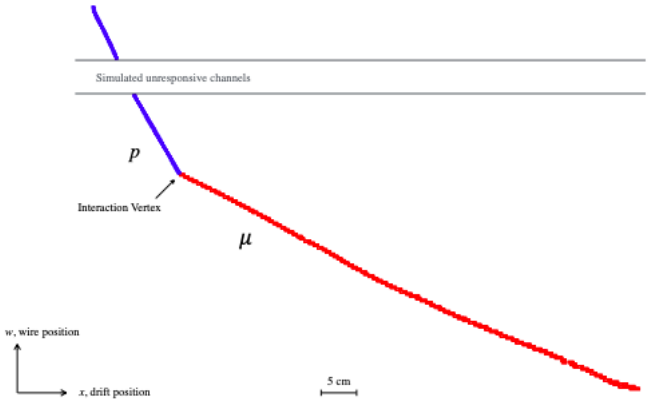

Figure 3.4: The reconstruction of a simulated 500 MeV CC ν_μ quasi-elastic interaction. The target particles for the reconstruction are the muon and proton. A gap in the reconstructed proton track is observed due to the presence of unresponsive channels, which are included in the simulation [28].

From another point of view, the QE process can be completely described in terms of the seven unknown momentum vector components (the muon and proton momentum vectors and the neutrino energy) that are reduced to three by the four energy-momentum conservation constraints when the nuclear environment effect is neglected. This immediately implies from the condition of zero overall transverse momentum,

$$|\Delta\varphi_{\mu p}| = \pi, \tag{3.3}$$

$$|\vec{p}_P| \sin\theta_P = |\vec{p}_\mu| \sin\theta_\mu, \tag{3.4}$$

where $\vec{p}_p$ and $\vec{p}_\mu$ the proton and muon momentum vectors.

Furthermore, the elastic scattering condition implies

$$E_p = \frac{E_\mu \left(E_\mu - p_\mu \cos\theta_\mu\right) + M^2 - m^2/2}{M - E_\mu + p_\mu \cos\theta_\mu}, \tag{3.5}$$

where M is the nucleon mass. Hence, the proton momentum vector is completely correlated with the muon momentum vector; and T_μ and $\cos\theta_\mu$ predict T_p and $\cos\theta_p$.

3.4 Resonance Production

In a resonant interaction (RES), the neutrino has enough energy to excite the target nucleon to a resonance state. Some possible reactions are,

$$\nu_\mu n \to \mu^- \Delta^+, N^{*+} \to \mu^- p\pi^0, \tag{3.6}$$

$$\nu_\mu p \to \mu^- \Delta^{++} \to \mu^- p\pi^+, \tag{3.7}$$

where Δ and N^* are excited baryon states. An example of RES event topology in MicroBooNE is shown in Fig. 3.5.

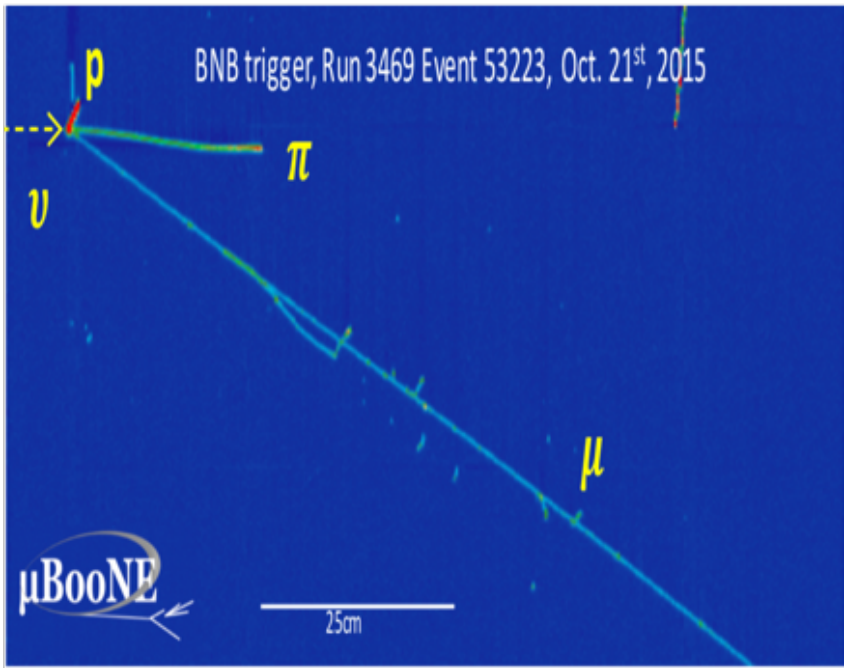

Figure 3.5: Shows the event display of the collection plane with ν_μCC RES candidate event from the MicroBooNE experiment [60].

In this case, the neutrino interaction produces a baryon resonance Δ (N^*) and immediately decays, most often to a pion and nucleon. Figure 3.6 shows a Feynman diagram for RES interactions.

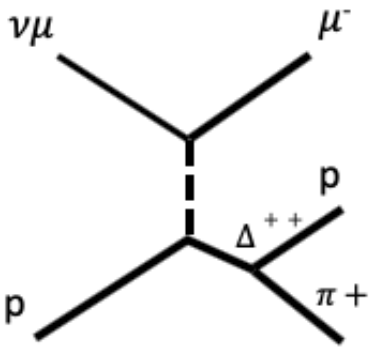

Figure 3.6: Feynman diagram for a RES interaction.

The simulation used in this thesis employs the GENIE neutrino generator, set up with the Rein-Sehgal model [41] for resonance production and the Bodek-Ritchie RFG model [42] for the interaction of the nucleon within the nucleus. Figure 3.7 shows the reconstruction of a simulated 1.1 GeV CC ν_μ interaction with resonant charged-pion production [28]. Figure 3.8 shows the reconstruction of a simulated 1.4-GeV CC ν_μ interaction with resonant neutral-pion production.

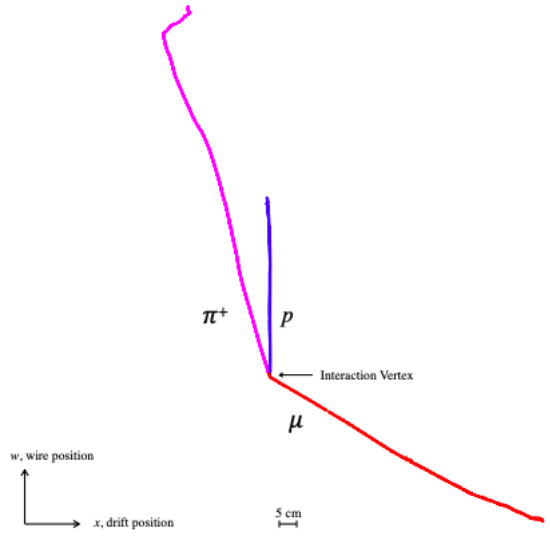

Figure 3.7: The reconstruction of a simulated 1.1 GeV CC ν_μ interaction with resonant charged-pion production. Target particles for the reconstruction are the muon, proton and charged pion [28].

Restricting to the $\Delta \to p\pi$ resonance, one has ten unknown momentum vector components (the muon, proton, and pion momentum vectors and the neutrino energy) and five constraints (energy-momentum and the Δ mass). Following the QE case, one can completely predict the Δ energy and momentum

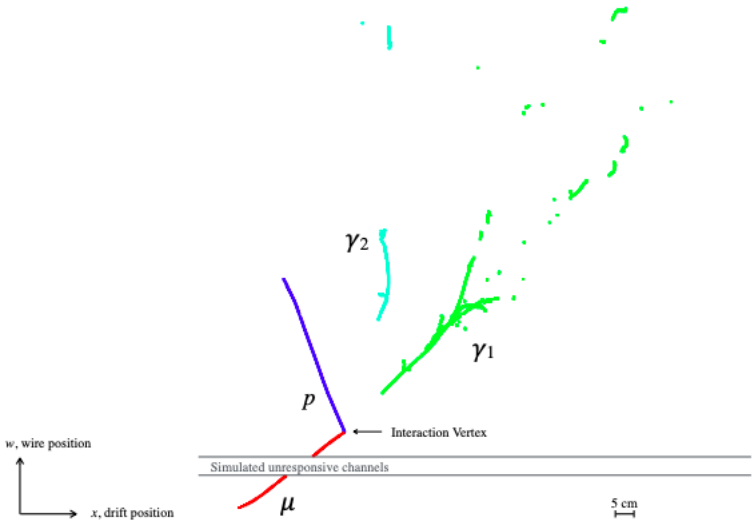

Figure 3.8: The reconstruction of a simulated 1.4-GeV CC ν_μ interaction with resonant neutral-pion production. Target particles for the reconstruction are the muon, proton and two photons from π^0 decay. The label γ^1 identifies the target photon with the largest number of true hits, while γ^2 identifies the photon with fewer true hits [28].

vector from the muon momentum vector:

$$|\Delta\varphi_{\mu\Delta}| = \pi, \tag{3.8}$$

$$|\vec{p}_\Delta| \sin\theta_\Delta = |\vec{p}_\mu| \sin\theta_\mu, \tag{3.9}$$

$$E_\Delta = \frac{E_\mu \left(E_\mu - |\vec{p}_\mu| \cos\theta_\mu\right) + \frac{1}{2}\left(M_\Delta^2 + M^2 - m^2\right)}{M - E_\mu + |\vec{p}_\mu| \cos\theta_\mu}. \tag{3.10}$$

The proton momentum in the Δ rest frame can express in terms of a fixed known momentum p^*

$$p^* = \frac{\sqrt{\left(M_\Delta^2 - (M + m_\pi)^2\right)\left(M_\Delta^2 - (M - m_\pi)^2\right)}}{2M_\Delta} \tag{3.11}$$

$$\simeq 224 \text{ MeV}. \tag{3.12}$$

Boosting back to the lab frame one obtains for proton momentum components along and perpendicular to the Δ direction

$$p_{\shortparallel} = \frac{E_\Delta}{M_\Delta} p^* \cos\theta^* + \frac{|\vec{p}_\Delta|}{M_\Delta}\sqrt{p^{*2} + M^2},$$

$$p_{\perp 1} = p^* \sin\theta^* \cos\varphi^*,$$

$$p_{\perp 2} = p^* \sin\theta^* \sin\varphi^*,$$

where θ^* and φ^* are the decay angles for the proton in the Δ rest frame; $p_{\shortparallel}$ is the proton momentum

component along the Δ direction in the lab frame, $p_{\perp 1}$, $p_{\perp 2}$ are the proton momentum components perpendicular to $\vec{p}_\Delta$ either in or out of the neutrino-muon scattering plane (in either frame). The measurable parallel and perpendicular proton momentum components satisfy the constraint

$$\frac{p_{\perp 1}^2 + p_{\perp 2}^2}{p^{*2}} + \left(\frac{p_{\shortparallel} - \frac{|\vec{p}_\Delta|}{M_\Delta}\sqrt{p^{*2}+M^2}}{\frac{E_\Delta}{M_\Delta}p^*} \right)^2 = 1. \tag{3.13}$$

More intuitively, for a "high" momentum Δ ($|\vec{p}_\Delta| \gg p^*$), the Δ kicks off the proton at an angle with respect to its flight direction of order p^*/p_Δ, which implies that the proton transverse momentum will remain fairly correlated with that of the muon. For a "slow" momentum Δ, this correlation will be lost, but the proton momentum will fall in a fairly narrow range around p^*. The smearing will persist all the way down to $|\vec{p}_\Delta| = 0$ due to the natural decay width $\Gamma_\Delta = 117$ MeV.

3.5 Deep Inelastic Scattering

In deep inelastic scattering (DIS), the neutrino has enough energy to interact with the single nucleon components, the quarks, and to break up the nucleon, producing a lepton and a hadronic system in the final state, which is the dominant interaction mode for high-energy neutrinos (> 5 GeV). The DIS interaction, presencented in this thesis, results in non-resonant proton plus hadron in the final state:

$$\nu_\mu d \to \mu^- u \to \mu^- p Y, \tag{3.14}$$

$$\nu_\mu \bar{u} \to \mu^- \bar{d} \to \mu^- p Y', \tag{3.15}$$

where Y and Y' are arbitrary hadronic final states.

Deep inelastic scattering has been used to validate the SM and probe nucleon structure. For the BNB energy DIS process relatively rare. An example of DIS event topology in MicroBooNE is shown in Fig. 3.9. Figure 3.10 shows a Feynman diagram for DIS interactions.

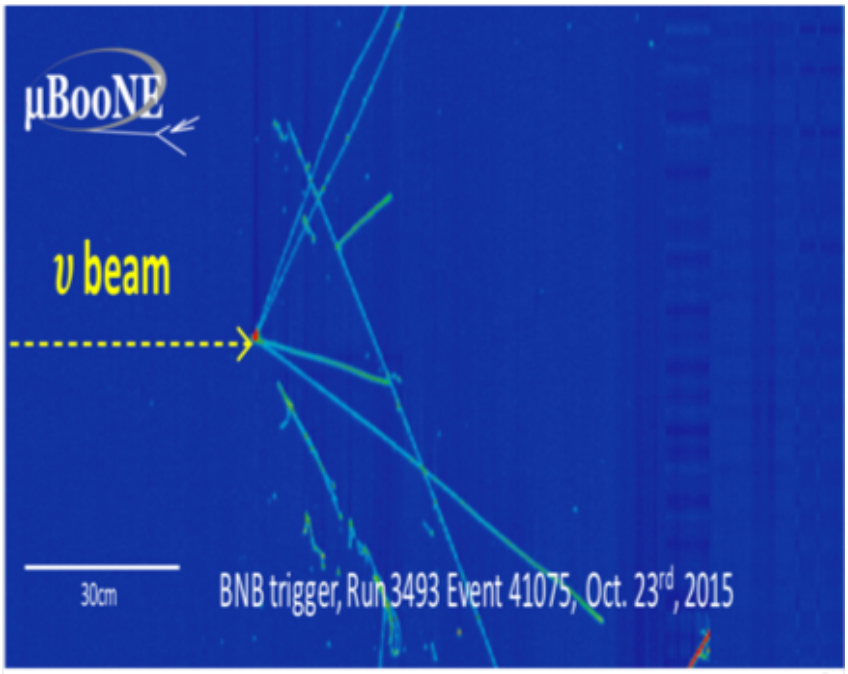

Figure 3.9: Shows the event display of the collection plane with ν_μ CC DIS candidate event from the MicroBooNE experiment [60].

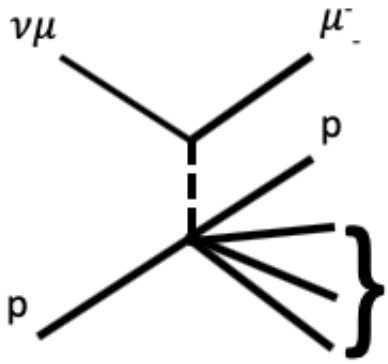

Figure 3.10: Feynman diagram for DIS interactions.

The simulation used in this thesis employs the GENIE neutrino generator, set up with the Bodek-Yang model [43] for DIS. The DIS process can be completely described in terms of the kinematic invariants, the inelasticity $y = \frac{p_N \cdot q}{p_N \cdot p_\nu}$, the 4-momentum transfer $Q^2 = -q^2 = (p_\nu - k_\mu)^2$, and the Bjorken scaling variable $x = \frac{Q^2}{2p_N \cdot q}$. Here, p_ν is the 4-momentum of the muon neutrino, p_N is the 4-momentum of the target nucleon, which is at rest in the lab frame, and k_μ is the 4-momentum of the outgoing muon. The Bjorken scaling variable plays a prominent role in deep inelastic neutrino scattering, where the target can carry a portion of the incoming energy-momentum of the struck nucleus [50].

3.6 2p-2h

In a 2p-2h process, the neutrino can scatter off a nucleon that is a part of a correlated two nucleon pair within the nucleus. The short-range correlation nucleon pair results in the 2p-2h process, instead of a single nucleon emission from the QE interaction as discussed in section 3.3. Nuclear theorists believe that the 2p-2h process is governed by meson exchange current, (MEC); and MEC is used to label this process in this thesis.

$$\nu_\mu np \rightarrow \mu^- pp, \tag{3.16}$$

An example of MEC event topology in the MicroBooNE experiment is displayed in Fig. 3.11. Figure 3.12 shows a Feynman diagram for MEC interactions.

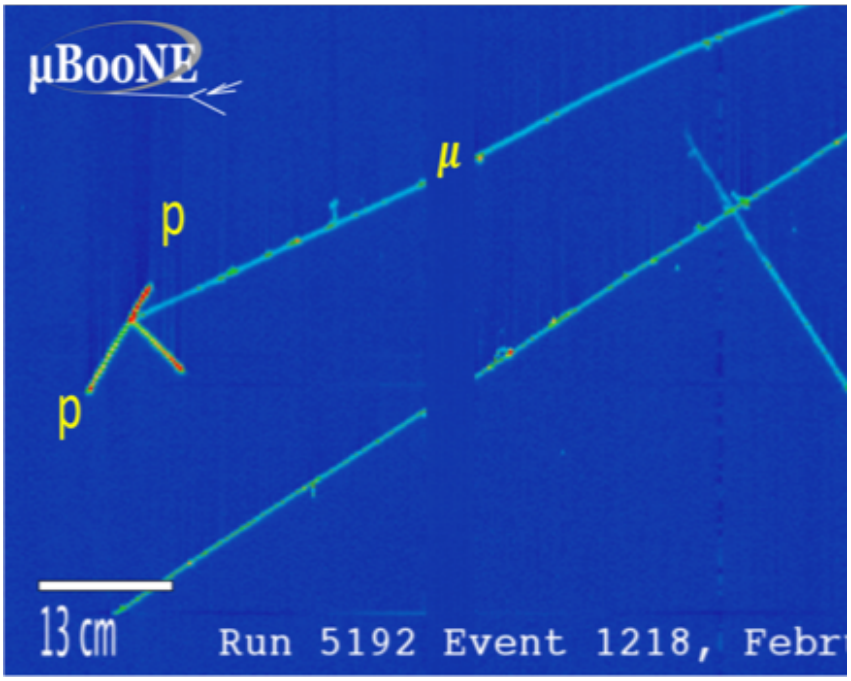

Figure 3.11: Shows the event display of the collection plane with ν_μ CC MEC candidate event from the MicroBooNE experiment [60].

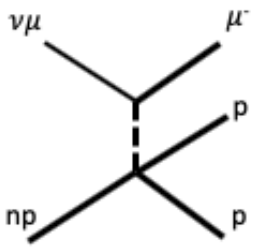

Figure 3.12: Feynman diagram for MEC interactions.

The simulation used in this thesis employs the GENIE neutrino generator, set up with an empirical 2p-2h process treatment [44]. This analysis will shed light on the 2p-2h process.

Chapter 4

The MicroBooNE Detector

4.1 Introduction

MicroBooNE (The Micro Booster Neutrino Experiment) is a liquid argon time projection chamber (LArTPC) experiment designed for short baseline neutrino physics, located at the Fermi National Accelerator Laboratory (Fermilab). MicroBooNE uses the Booster Neutrino Beam (BNB). The MicroBooNE detector began operating in October 2015, observing neutrinos between a few tens of MeV to a few GeV. MicroBooNE aimes to clarify the nature of the low energy excess of ν_e-like events observed by the MiniBooNE experiment in 2009 [24], and to refine sensitivity estimates for next generation detectors such as the Deep Underground Neutrino Experiment (DUNE). Figure 4.1 shows a schematic diagram of the MicroBooNE LArTPC.

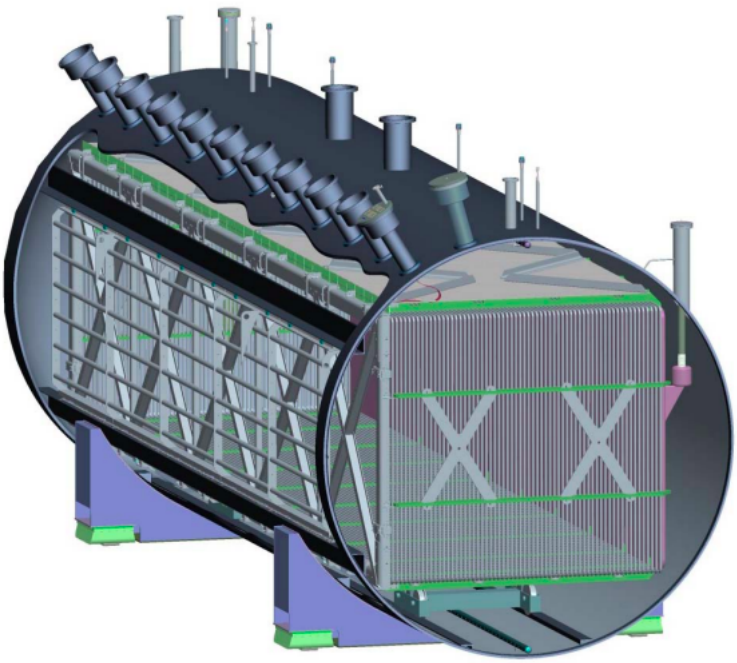

Figure 4.1: Schematic diagram of the MicroBooNE LArTPC [20].

The main scientific objective of MicroBooNE is to investigate the nature of the low energy excess of ν_e-like events observed by MiniBooNE by utilizing superior photon-electron identification. MiniBooNE, a mineral oil Cherenkov detector, is unable to distinguish Cherenkov rings, shown in Fig. 4.2, from electromagnetic showers that originate from either an electron or a photon.

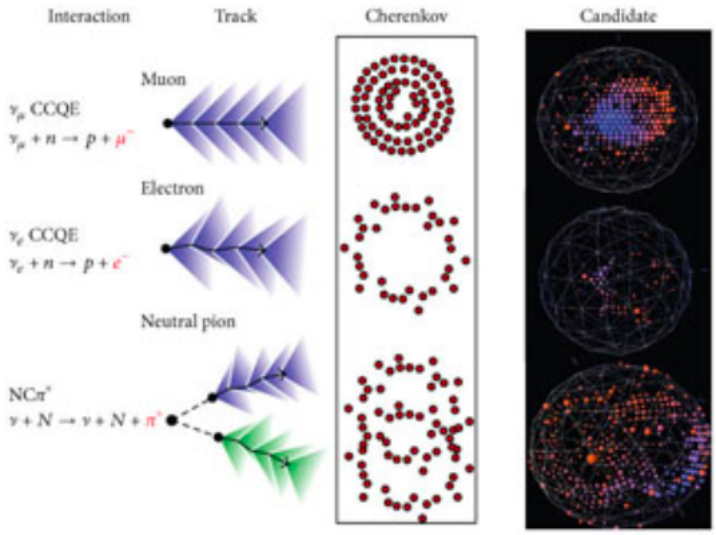

Figure 4.2: MiniBooNE particle reconstruction from top to bottom, a moun neutrino charged-current quasielastic (CCQE) interaction, an electron neutrino CCQE interaction, and a neutral current, neutral pion production (NC1π^-) interaction. The second and third columns show the characteristics of tracks and Chernkov rings, and the last column shows the displays of candidate events [51].

On the other hand, MicroBooNE has two significant reconstruction techniques to distinguish between electron and photon particles in its detector. The first technique is the property of photon particles in LAr. Photon particles can not be detected directly, they will travel approximately 14 cm (the radiation length) in liquid argon until the most probable interaction processes for photons in LAr, Compton scattering or pair production, occurs, in which charged particles are produced [52]. The second technique is the charge per unit length (the dE/dx profile). At the beginning of electron and photon showers, a photon produced in LAr usually converts to an e^+ e^- pair, which ionizes at twice the rate of a single electron. These two significant reconstruction techniques give the MicroBooNE detector a superior capability for separation of signal electrons from the background of photon conversions.

The two main components of the MicroBooNE detector are the LArTPC and the light collection system, which are both immersed in liquid argon contained within a single-walled cryostat with a 170-tonne capacity as will be discussed in Section 4.2 and 4.3, respectively in this chapter. This present thesis analyzes a subset of data taken by MicroBooNE.

4.2 Time Projection Chamber

The MicroBooNE detector consists of a rectangular LArTPC active volume with dimensions of 2.56 m(horizontal)× 2.325 m(vertical) × 10.368 m(longitudinal) placed in a cylindrical cryostat. It sits on-axis with the BNB, 470 m from the neutrino beam target. The mass of liquid argon in the active volume, defined as the portion of the argon encompassed by the TPC, is 90 tonnes.

The LArTPC is composed of three major structures: the cathode, the field cage, and the anode, as shown in Fig. 4.3.

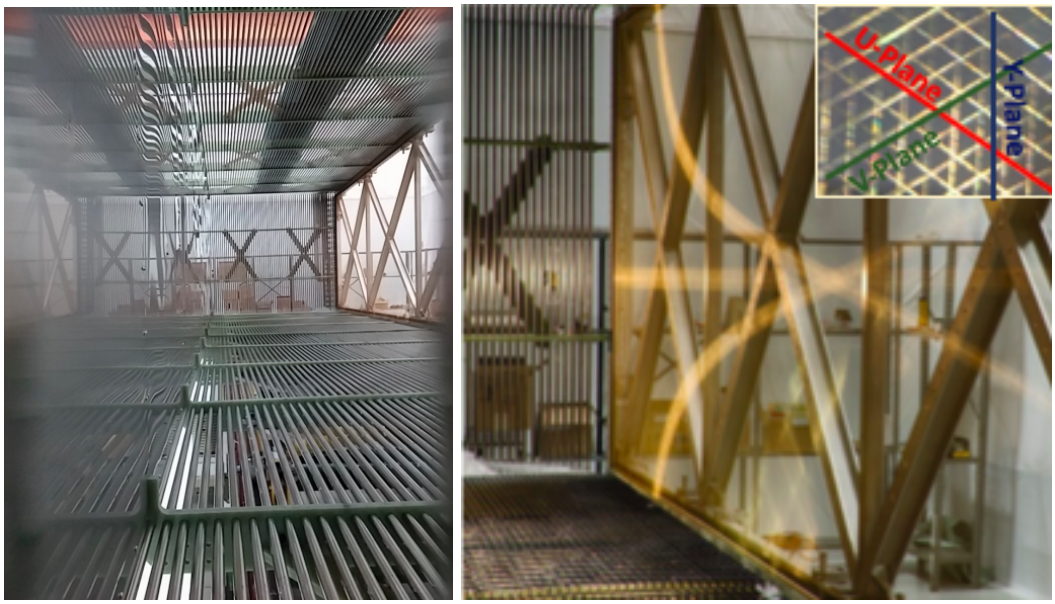

(a) (b)

Figure 4.3: (Left) The cathode plane as viewed from the upstream end of the LArTPC and the field cage bounded by the anode and cathode planes. (Right) The three anode plane sense wires are shown. Insert shows the anode plane wire orientations the U, V, and Y (60°, −60°, and 0° w.r.t. vertical) [20].

The cathode and the anode planes define the beam-left and beam-right sides of the LArTPC active volume. The field cage structure consists of stainless steel tubes. It steps down the voltage toward the anode, creating a uniform electric field across the entire width of the detector. Figure 4.4 shows a cartoon of the MicroBooNE LArTPC operational principle. Charged particles traversing in the bulk of the TPC leave traces of ionization electrons, which are drifted to the anode plane under a uniform electric field, 273 V/cm.

The anode planes are a successive array of 3 mm wire spacing. They are oriented at angles of 60°, −60°, and 0° with respect to the vertical as shown in Fig. 4.3. The first two planes are referred to as the induction planes and the wire plane farthest from the cathode plane is referred to as the collection

plane. Further details may be found in [20]. In the induction planes, the drift electrons pass through the wire plane and induced bipolar signals, while in the collection plane the electron trajectory ends at the wire, so collecting the charge of the drifting electrons results in a unipolar signal.

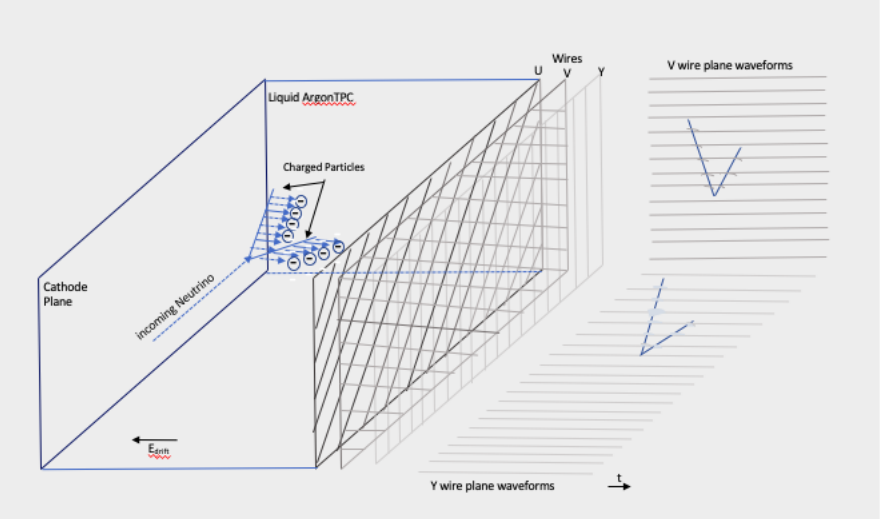

Figure 4.4: A schematic representation of the LArTPC technology [20].

4.3 The Light Collection System

Scintillation light, produced by excited argon atoms, is detected by the MicroBooNE light collection system, which is an array of 32 photomultipliers (PMTs) immersed in the liquid argon and located behind the anode plane (which is 86% transparent to the light) as shown in Fig. 4.5.

Figure 4.5: PMT rack array located behind the anode wire planes and mounted on the MicroBooNE cryostat wall [20].

The liquid argon scintillation light has a typical spectrum peaked at a wavelength of 128 nm. The scintillation light signal is important for rejecting cosmic background. Also, it can be used to provide a trigger signal for the readout and data acquisition (DAQ) systems, and it can provide event timing since scintillation light arrives within tens of nanoseconds. This feature helps wire signals to determine the

drift time of the ionization particles because of the millisecond length of the TPC readout time.

The data acquisition (DAQ) system takes as input the triggered TPC and PMT readouts and translates the raw data format into ROOT files, one for each trigger which are then stored on tape.

Chapter 5

The Booster Neutrino Beam

The main source of neutrinos for the MicroBooNE experiment is Fermilab's Booster Neutrino Beamline (BNB). Protons with 8 GeV of kinetic energy (8.89 GeV/c momentum) are extracted from the BNB and directed towards a beryllium target. This produces secondary particles. With decays of the secondary particles, a neutrino beam energy ∼800 MeV is reached, which is then pushed ahead to the MicroBooNE detector. This Chapter describes the booster proton beam in Section 5.1, proton target and focusing horn in Section 5.2, and beam composition in Section 5.3.

5.1 The Booster Proton Beam

The Booster proton beam begins with a beam of negative hydrogen ions H^- produced by using a Cockcroft–Walton generator. These are pulsed through a linear accelerator machine (LINAC), in which alternating electromagnetic fields are used to accelerate the H^- ions from 750 keV to 400 MeV [33]. Protons gain access to the 474 m circumference booster synchrotron, which runs at a rate of 15 Hz. That accelerates the protons up to 8.89 GeV. At this stage, protons are bunched in the "beam spills" (structured in 81 bunches, each ∼2 ns wide and 19 ns apart) containing 5×10^{12} protons spaced in a 1.6 µs time window per spill. The protons are directed towards a target.

Protons intensity (protons-per-pulse) is measured by two toroids upstream of the target, which are part of a larger beam monitoring system. Additionally, the Booster proton beam characteristics are monitored by beam position monitors, a multi-wire chamber, and a resistive wall monitor. These systems measure beam width, position, and time and intensity of the beam spills, respectively.

5.2 Proton Target and Focusing Horn

The proton beam hits the beryllium target, of which is a cylinder 71.1 cm long and 0.51 cm in radius. Key features associated with the use of beryllium are thermal conductivity, low density, and low activation properties. As a result, beryllium minimizes the remnant radioactivity issues in the event due to proton exposure and minimizes the beam power load on the target cooling system. Also, it yields a high pion production. It is installed inside a set of magnetics, called a horn.

The horn is made of an aluminum alloy. It is a pulsed with a toroidal electromagnet with a 174 kA in both neutrino and anti-neutrino mode as shown in Fig. 5.1. When protons hit the target, secondary mesons are produced, including the primarily charged pions and charged kaons. Almost 100% of the charged pions decay to neutrino and muon, and 63% of the charged kaons decay to neutrino and muon. As a result, the primary source of neutrinos and anti-neutrinos comes from these secondary mesons. Tuning the direction of the magnetic field inside the magnet focusing horn produced the positive or the negatively charged mesons.

Then, the focused charged pions and kaons pass through 49.87 m decay region, which is a steel pipe. After that, there is a concrete collimator, in which the secondary mesons are stripped to leave just the neutrinos. These neutrinos then travel a distance of 470 m toward the MicroBooNE detector.

5.3 Beam Composition

The predicted composition of the BNB flux is dominated by ν_μ as shown in Fig. 5.1, which are produced by π^+ decay. Indeed, pions are the largest number of particles produced in the beryllium target. The predicted neutrino beam composition at BNB with the horn in neutrino mode is shown in Table 5.1 [33].

Table 5.1: Summarizes the predicted neutrino beam composition at BNB with the horn in neutrino mode [33].

Head	ν_μ	$\overline{\nu}_\mu$	ν_e	$\overline{\nu}_e$
Frac. of the Total	93.6%	5.86%	0.52%	0.05%

The neutrino flux prediction at the MicroBooNE detector utilizes the BNB Monte Carlo simulation developed by the MiniBooNE collaboration [33]. The MiniBooNE framework includes a well-constrained beamline simulation based on GEANT4. Figure 5.1 shows the neutrino flux split in the contributions

from the four neutrino states as modeled by the MiniBooNE beam simulation [33] and calculated for the MicroBooNE detector. The flux uncertainties were estimated for this analysis for the present thesis and are detailed in Section 8.2.

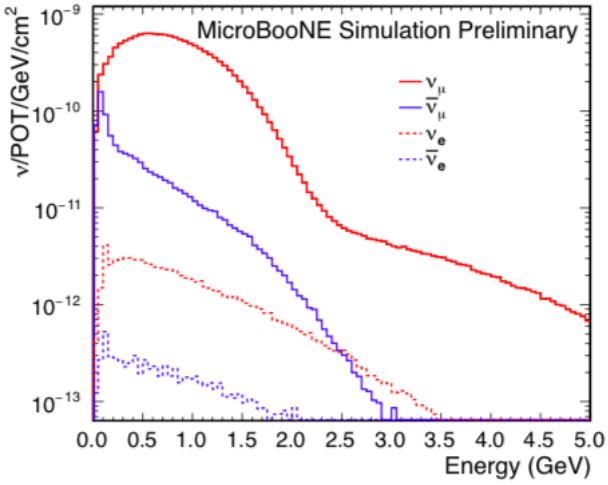

Figure 5.1: Neutrino flux prediction at MicroBooNE for four neutrino states as modelled by the MiniBoonNE beam simulation applied to MicroBooNE [46].

Chapter 6

Event Reconstruction

The DAQ system takes the triggered TPC and PMT readouts as input and translates the binary data format recorded by the detector. These are used as the input for the reconstruction algorithms. The present thesis used fully automated reconstruction algorithms, the Pandora Software Development Kit for pattern recognition [28]. This Chapter presents the optical reconstruction in Section 6.1, hit reconstruction in Section 6.2, and TPC reconstruction in Section 6.3.

6.1 Optical reconstruction

The optical systems supplies triggering information to an electronic readout system as discussed in Section 4.3, and it can contribute to the reconstruction. The scintillation light is shifted into the localized visible light using tetraphenyl butadiene (TPB). The optical reconstruction accumulates the raw waveform from the individual PMTs and combines them to create "flashes". The localized visible light can be correlated with specific tracks in the detector, which is called "flash-track matching". "Flash-track matching" leads to identification and reconstruction of the tracks that are in time with the beam spill [20].

6.2 Hit reconstruction

After signal processing and noise suppression from the detector electronics [48], the next step is performed by fitting Gaussians to the average deconvolved signal shape in each peak of the waveform. These are called hits. Each of these extracted hits from these digital waveforms is input to the Pandora algorithm software. Hits can be characterized by the definite drift time, the RMS, and the charge deposited, which correspond to the mean, width, and the integral of the fitted Gaussian, respectively.

6.3 TPC Reconstruction

These extracted hits discussed in Section 6.2 are separated into three different lists, one for each anode plane, and passed through a large number of decoupled algorithms. Each algorithm aims at a specific event topology. Another further algorithm groups hits together into clusters, in two-dimensions, in each readout plane. 3D reconstruction algorithms take these clusters in the three planes as input, and aim to reconstruct the three-dimensional objects which in Pandora are called "PFParticles"; PF stands for Particle Flow for the reconstructed particles. Each PFParticle corresponds to a track or a shower. Furthermore, Pandora pattern recognition has an ability to create a hierarchy of reconstructed PFParticles, which identifies parent-daughter relationships. This is powerful for the reconstruction of complicated neutrino interactions [28].

Two Pandora multi-algorithm reconstruction modes have been created for use in the analysis of MicroBooNE data. These are the primary algorithms for this analysis:

- PandoraCosmic is optimized for the reconstruction of cosmic-ray muons and their daughter delta rays.
- PandoraNu is optimized for the reconstruction of neutrino interactions.

Chapter 7

Inclusive ν_μ Charged Current (CC) Proton Production

7.1 Introduction

Consider final states with one muon, one "leading proton" (the highest energy one in the event), and anything else:

$$\nu_\mu \mathrm{Ar} \rightarrow \mu^- p X. \tag{7.1}$$

The notation X means "anything else". This is referred to as inclusive charged current proton production ("inclusive CC-proton").

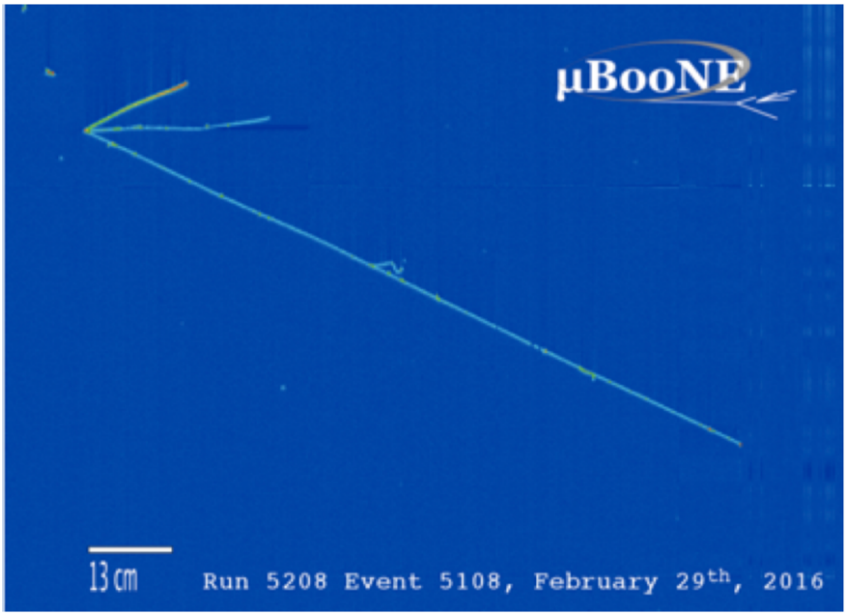

Figure 7.1: Shows the event display of the collection plane with muon and proton in the final state as the signal definition for inclusive CC proton production model [47].

The goals of this analysis are to first test the general hypothesis GENIE employs to describe this process, and then, assuming the consistency of the hypothesis, optimize GENIE's description. This test and optimization directly supports anomalous electron-neutrino-like production searches at MicroBooNE, which generally look for some variant of the reaction

$$\nu_X \mathrm{Ar} \rightarrow e^- p X. \tag{7.2}$$

This measurement differs from other ν_μ CC currently under consideration at MicroBooNE, which either have no requirement on pX ("CC-inclusive") [19], or have X containing no other reconstructable objects ("CC-QE") [32] or X containing no other protons or reconstructable pions ("CC-1$p0\pi$ ") [31] or X containing at least one additional reconstructable proton and no reconstructable pions ("CC-2$p0\pi$") [31].

The inclusive CC-proton final state is the most common at MicroBooNE. In GENIE at truth level, approximately 66.6% of CC events have a proton with kinetic energy above the ∼50 MeV detection threshold. Production should be dominated by the quasielastic ("QE") process at the sub-nuclear level,

$$\nu_\mu n \rightarrow \mu^- p, \tag{7.3}$$

with further contributions from resonant Δ (and N^*) production ("RES"),

$$\nu_\mu n \rightarrow \mu^- \Delta^+ \rightarrow \mu^- p \pi^0, \tag{7.4}$$

$$\nu_\mu p \rightarrow \mu^- \Delta^{++} \rightarrow \mu^- p \pi^+, \tag{7.5}$$

and two-nucleon scattering processes, referred to as $2h2p$ or ("MEC") for short,

$$\nu_\mu np \rightarrow \mu^- pp. \tag{7.6}$$

MEC contributions were neglected in early versions of GENIE, but a consensus has developed that they are important as discussed in Section 3.6. Finally, there is the "everything else" category labelled "DIS", typically modelled as non-resonant multi-hadron production the framework of the quark-parton model

for the neutrino scattering followed by a hadronization model:

$$\nu_\mu d \to \mu^- u \to \mu^- p Y, \tag{7.7}$$

$$\nu_\mu \bar{u} \to \mu^- \bar{d} \to \mu^- p Y', \tag{7.8}$$

where Y and Y' are arbitrary hadronic final states.

Models of CC-proton production, e.g. GENIE, assume that it can be described by an incoherent sum of the contributing sub-processes:

$$\sigma_G\left(\mu p X\right) = \sigma_{QE}\left(\mu p X\right) + \sigma_{MEC}\left(\mu p X\right) + \sigma_{RES}\left(\mu p X\right) + \sigma_{DIS}\left(\mu p X\right). \tag{7.9}$$

There are subtleties in this picture, but it is practical and universally used.

A major complication is that identical final states can be produced by different processes, especially if final state effects (FSI) are incorporated. For example, while the simplest QE event would produce a transverse-momentum-conserving coplanar μp final state, a QE event in which the proton scatters on its way out of the nucleus would not show this topology, and could in fact appear very similar to a MEC event that has a very low energy second proton. If the QE+FSI and MEC processes end up producing the same final state, then interference effects could be present; and it may be inherently impossible to distinguish the mechanisms. Even without interference, it could be practically impossible on an event-by-event basis to classify an event as QE or MEC.

Despite these complications, there is some evidence that the naive categorization of events by their primary neutrino interaction type is useful. A statistical classification remains possible in any case, and for some kinematic ranges, this classification can be very effective. For example, a class of QE events does exhibit transverse momentum conservation. As described below, this analysis will test this idea more completely. It will also, within the GENIE framework, experimentally determine the relative contribution of each sub-process.

Since the MEC, RES, and DIS topologies all have at least, in principle, two hadrons in the final state, a natural question about the approach taken here is why only the leading proton is examined. At a fundamental level, the μp combination is used as a probe of the final state. This is a less inclusive probe than the muon alone, but it brings several benefits:

1. The addition of a proton to the muon strongly suppresses the cosmic ray (CR) background over the full phase space. One additional requirement on muon-proton acolinearity yields further reduc-

tion. The residual CR contamination can be characterized with off-beam events and empirically determined in the data.

2. The lack of restrictions on other final state objects means that "neutrino backgrounds", which would otherwise need to be calculated in a model-dependent way, are much reduced. These largely consist of neutral current (NC) πp events at the percent level.

3. The two-track final state efficiency is inherently greater than that for ≥ 3 tracks simply because of efficiencies to the first-order factor, and $\epsilon_1\epsilon_2 > \epsilon_1\epsilon_2\epsilon_3$. Efficiencies for finding π^0 are less than for charged tracks.

4. MicroBooNE has powerful proton identification capabilities. Since charged kaon and deuteron production are very small, particle identification reduces to distinguishing a proton from a much lighter pion or muon. Protons at MicroBooNE essentially never produce a minimum ionizing particle (MIP) signature, since this requires proton momentum $p > 2.8$ GeV.

5. The "second" proton in a MEC event is often below the detection threshold and in any case does not uniquely identify an event as MEC. A combination of muon and leading proton measurements might yield MEC sensitivity that complements that of two-proton analysis [31].

6. If single π^+ production is dominated by resonance decay, it follows essentially from time-reversal that π^+ resonantly scatter from argon nuclei, making them difficult to detect. The pion hadronic interaction length is less than its predicted range in liquid argon for all kinetic energies above 120 MeV.

This analysis is intended to both test and optimize GENIE, and not to provide corrected data to the community. It is primarily aimed at supporting neutrino oscillation physics for both MicroBooNE and DUNE. On MicroBooNE, most GENIE tuning relies almost exclusively on using external experimental data from mainly carbon targets. This approach has been explicitly rejected by DUNE's review committees, who emphasize that only argon data is suitable for developing cross section models that support oscillation physics with LArTPC detectors. The results of this analysis provide a GENIE tune that is optimized directly with MicroBooNE data (the only such tune). The results of this analysis further validate the use of GENIE in estimating the physics sensitivity of DUNE.

7.2 Kinematics

One can completely characterize the $\mu^- p$ final state by five kinematic variables:

- The muon kinetic energy T_μ;
- The muon scattering angle variable $\cos\theta_\mu$;
- The proton kinetic energy T_p;
- The proton scattering angle variable $\cos\theta_p$;
- The difference in the muon azimuthal angle and the proton azimuthal angle $\Delta\varphi_{\mu p} = \varphi_\mu - \varphi_p$.

Only the azimuthal angle difference appears due to the cylindrical symmetry of the neutrino beam. This set of five variables will be referred to as $\vec{\Omega}$.

If only $\mu^-$and p are in the final state, then the neutrino energy E_ν is also determined. The presence of additional final state particles X imply that a given $\vec{\Omega}$ can be produced by a range of E_ν.

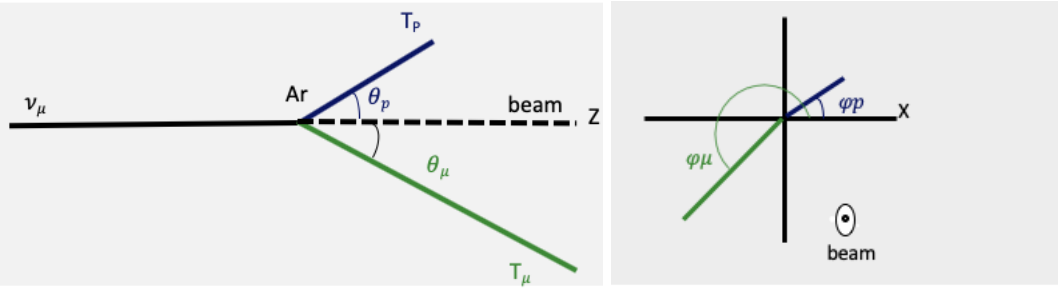

(a) (b)

Figure 7.2: Cartoon of MicroBooNE coordinate system shows the definition of some kinematic variables the azimuthal angle φ, the polar angle θ and for muon track (green) and proton track (blue). The neutrino beam runs along the z-axis.

7.3 Data and Simulation Samples

All data and Monte Carlo samples are produced with MCC8, which refers to the version of MicroBooNE software.

7.3.1 Data

This analysis uses a subset of data recorded from February to April 2016. This sub-sample corresponds to an exposure of the MicroBooNE detector of 4.87×10^{19} protons-on-target (POT).

Two different data modes are used in this study:

- The "on-beam data", which is taken only during periods when a beam spill from the BNB is actually on.
- The "off-beam data", which is taken with the same conditions as on-beam data, but during periods when no beam was received.

7.3.2 Simulation

This analysis used several sub-samples of Monte Carlo events.

- BNB + cosmic sample. Each event has a simulated ν interaction inside the MicroBooNE cryostat, where the neutrino flavors are weighted according to the BNB neutrino flux composition, and simulated cosmic rays hitting the detector in the same readout window. This analysis focused on ν_μ neutrino interaction.
- Dirt sample. Each event has a simulated ν interaction outside the MicroBooNE cryostat. The products can enter the MicroBooNE TPC and occasionally mimic a neutrino interaction.
- Detector Systematic samples. The events are BNB neutrino plus CORKSIKA cosmic throughout the cryostat. These samples assist in estimating systematic uncertainty associated with the MicroBooNE detector in the simulation. The procedure is to compare the standard simulation called central value with simulation with a variant detector model.

Neutrino events have been generated using LArSoft v04.36.00.03, including the GENIE Neutrino Monte Carlo generator version 2.8.6 [1] and cosmic rays have been generated using the CORSIKA Monte Carlo generator version 7.4003 [21].

7.4 Event Selection

Event selection consists of three main steps: (1) CC events selection following the inclusive CC analysis [19], (2) proton identification following the strategy of the CC-2-protons and one muon in the final state analysis [31], and application of a cut on the acolinearity between the muon and leading proton candidate for further cosmic ray (CR) background suppression.

- The CC inclusive selection: The inclusive CC ν_μ selection described in [19], used for this inclusive CC proton production analysis. The measurement is presented as a function of reconstructed muon kinematics, where all the event vertices are required to be inside the fiducial volume. All

candidate tracks are required to have at least 5 hits in the collection plane. This requirement is for high-quality reconstruction, and for the PID method exclusion of the first and last hits on the track. The signal topology for a ν_μ CC inclusive measurement is the presence and identification of a neutrino-induced muon track with or without accompanying other particles.

- The proton candidate must satisfy the condition $\chi^2_p < 88$, where χ^2_p tests the hypothesis that a stopping track in the detector is consistent with a proton using the profile of $dEdx$ vs. residual range, while the moun candidate must satisfy $\chi^2_p > 88$. More details can be found in [31]. The moun and leading proton candidates must be completely contained in the TPC. All kinetic energies are determined from range, so all candidate tracks are chosen to be contained tracks.

- The cosine of the acolinearity angle < -0.95: This suppresses events with a "broken track" as shown in Fig. 7.3, usually a single muon that has been split into two objects by Pandora (often due to the presence of dead wires). Broken tracks have a three-dimensional opening angle $\Phi_{\mu p}$, defined in Eq. 7.10, which is very close to π.

$$\cos\Phi_{\mu p} = \cos\theta_\mu . \cos\theta_p + \sin\theta_\mu . \sin\theta_p \cos\Delta\varphi_{\mu p}, \tag{7.10}$$

where $\Phi_{\mu p}$ is the acolinearity angle. That is, the tracks are exactly back-to-back.

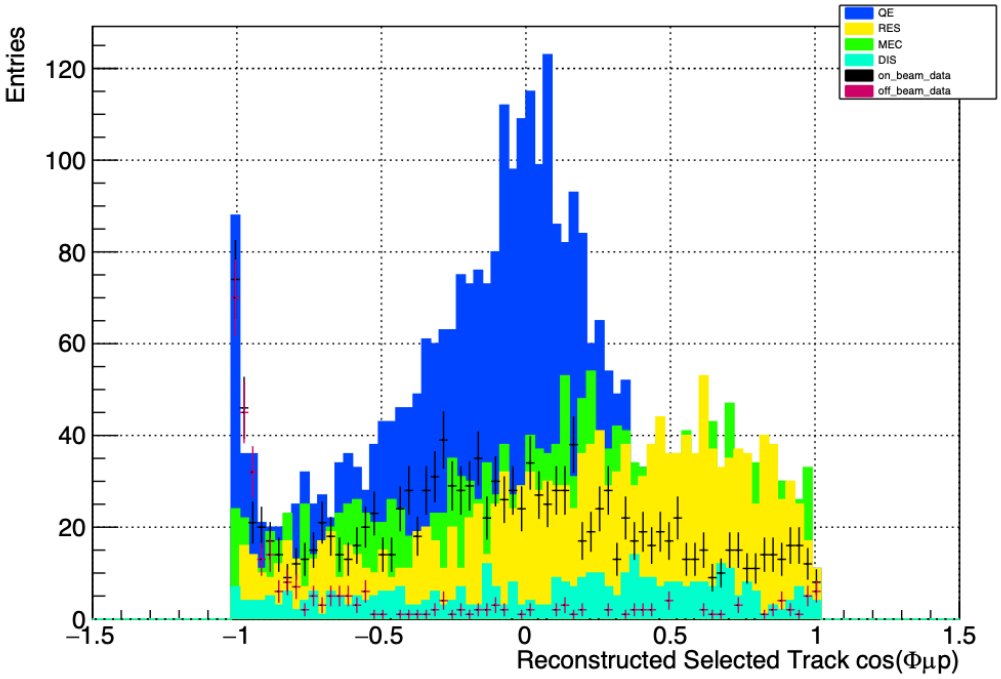

Figure 7.3: Distribution of $\cos\Phi_{\mu p}$ for on-beam data(black) and off-beam data (red), and for simulated QE, RES, DIS, and MEC events. The sharp peak at $\cos\Phi_{\mu p} = -1$ is attributed to "broken tracks".

Table 7.1 shows the fraction of events passing the selection criteria, and Table 7.2 shows the number of events passing the selection criteria.

Table 7.1: The fraction of events passing the selection criteria.

Selection	QE	RES	DIS	MEC
CC inclusive	0.41	0.29	0.08	0.22
contained tracks	0.40	0.29	0.08	0.23
PID cuts	0.43	0.23	0.06	0.28
The cosine of the acolinearity angle < -0.95	0.43	0.24	0.06	0.28

Table 7.2: The number of events passing the selection criteria.

Selection	On-beam data	Off-beam data
CC inclusive	3558	1427
contained tracks	2993	1190
PID cuts	1431	306
The cosine of the acolinearity angle < -0.95	1301	181

Figure 7.4 shows projections of the acceptance and Fig. 7.5 shows projections of the efficiency estimated from the Monte Carlo simulation. Here, acceptance is defined as the ratio of the number of detectable events to the total number of CC events, where "detectable" is defined by the conditions $T_\mu > 100$ MeV and $T_p > 50$ MeV (using generated versions of the kinematic variable from the MC simulation); and

efficiency is defined as the ratio of the number of events satisfying all selection criteria (using reconstructed kinematic variables in the MC simulation) to the number of detectable events. The muon and proton energy thresholds are, approximately, 100 and 50 MeV, respectively. The muon energy acceptance falls of at higher values due to the containment criterion. More details are shown in Appendix C.1 Fig. C.1 - C.2.

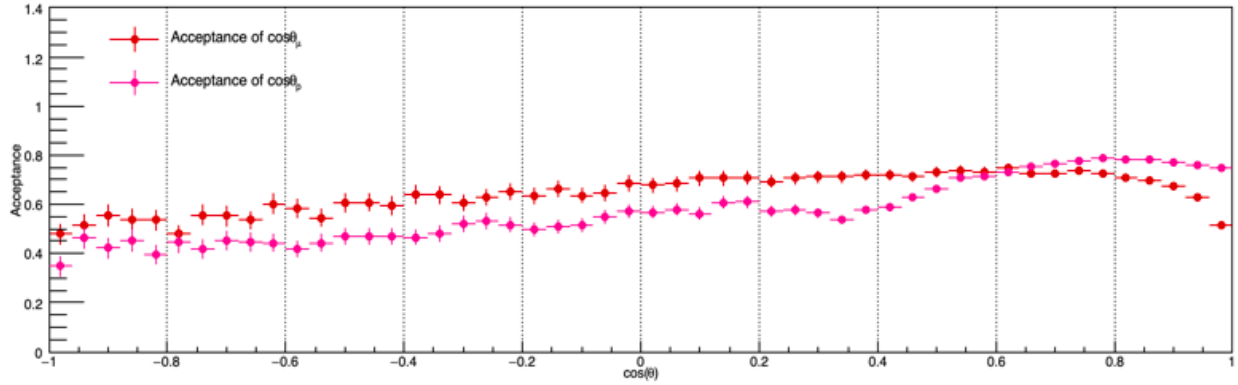

(a)

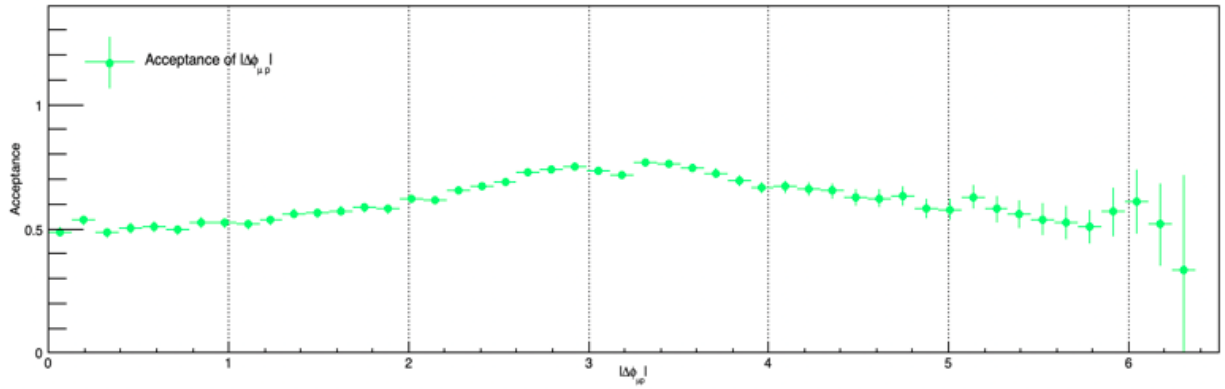

(b)

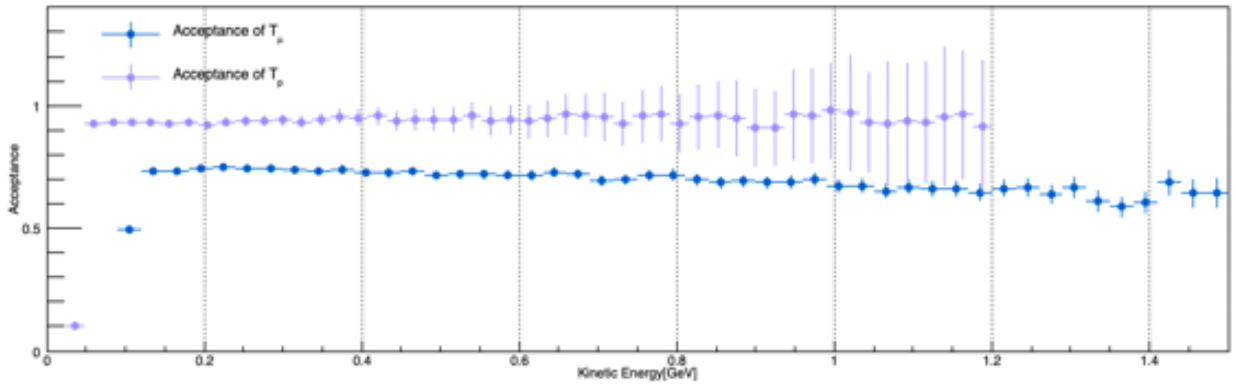

(c)

Figure 7.4: (a) Acceptance as a function of muon kinetic energy T_μ, and proton kinetic energy T_p, (b) acceptance as a function of muon scattering angle variable $\cos\theta_\mu$, and the proton scattering angle variable $\cos\theta_p$, and (c) acceptance as a function of the difference in the muon azimuthal angle and the leading proton azimuthal angle $|\Delta\phi_{\mu p}|$.

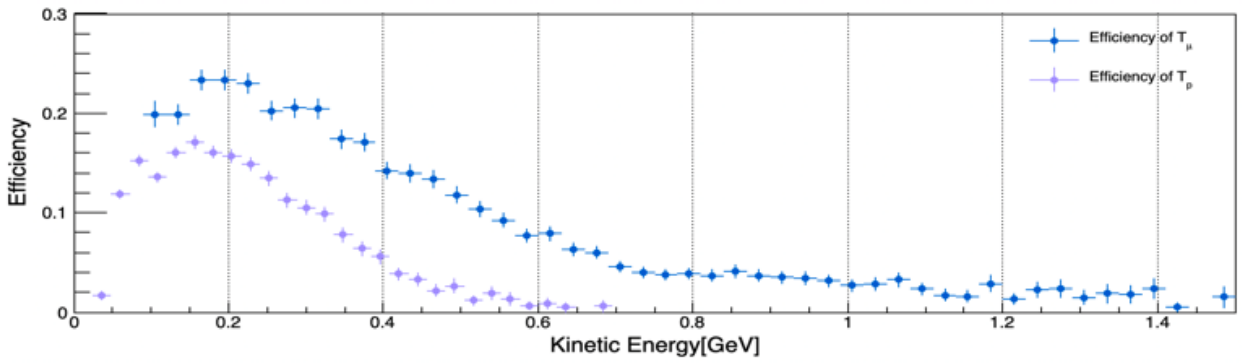

(a)

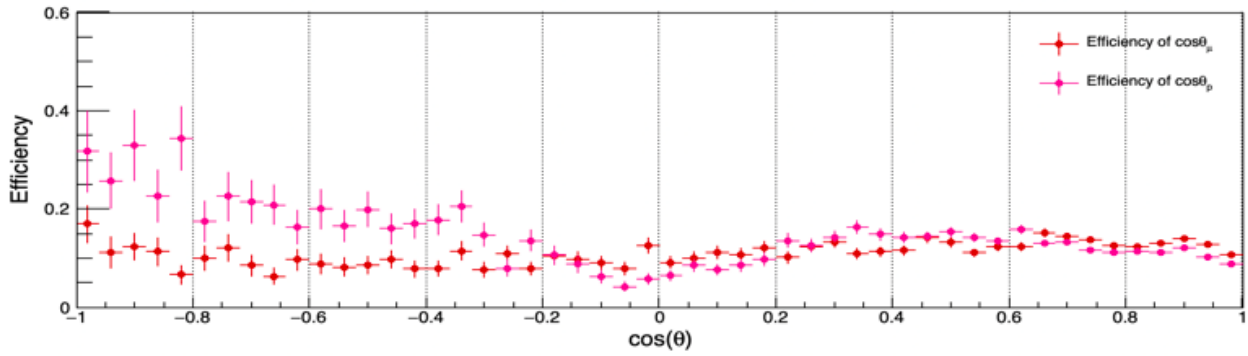

(b)

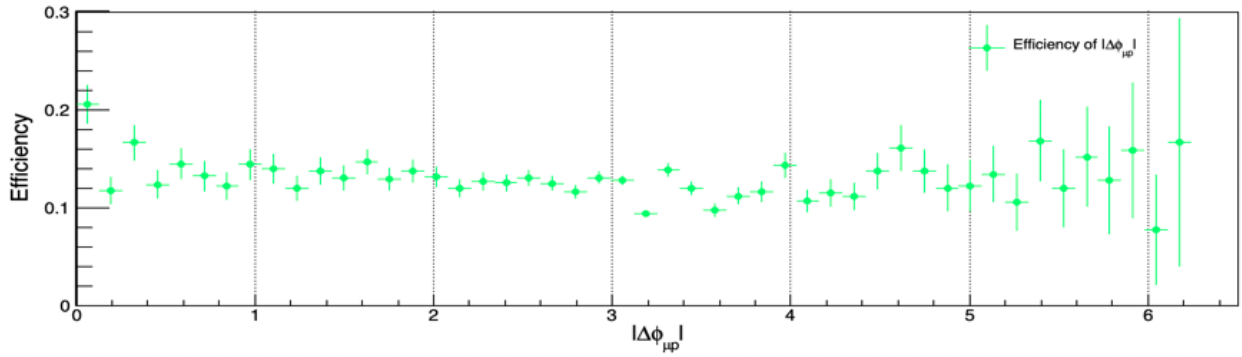

(c)

Figure 7.5: (a) Efficiency as a function of muon kinetic energy T_μ, and proton kinetic energy T_p, (b) efficiency as a function of muon scattering angle variable $\cos\theta_\mu$, and the proton scattering angle variable $\cos\theta_p$, and (c) efficiency as a function of the difference in the muon azimuthal angle and the leading proton azimuthal angle $|\Delta\phi_{\mu p}|$.

7.5 Analysis Strategy: Direct Comparison to Observables

Most MicroBooNE analyses attempt to extract total cross sections and differential cross sections in one or two variables after efficiency correction, unfolding for resolution, and normalizing by flux. The hope is that these measurements would constrain processes like those mentioned above once outside theorists analyze them.

An alternative analysis would attempt to use all measurements from an event and a model, such as GENIE, to fit for the relative contributions, of QE, MEC, RES, and DIS, bypassing the efficiency, unfolding, and even normalization steps. In the simplest example, one might simply allow the relative contributions to vary according to some normalization parameters A_{QE}, A_{MEC}, A_{RES}, and A_{DIS}, defined below

$$\sigma_G\left(\mu pX; E, \vec{\Omega}\right) \rightarrow \sigma'_G\left(\mu pX; E, \vec{\Omega}\right) \tag{7.11}$$

$$= A_{QE}\sigma_{QE}\left(\mu pX; E, \vec{\Omega}\right) + A_{MEC}\sigma_{MEC}\left(\mu pX; E, \vec{\Omega}\right)$$

$$+ A_{RES}\sigma_{RES}\left(\mu pX; E, \vec{\Omega}\right) + A_{DIS}\sigma_{DIS}\left(\mu pX; E, \vec{\Omega}\right) \tag{7.12}$$

$$\equiv \sum_q A_q \sigma_q \left(\mu pX; E, \vec{\Omega}\right) \tag{7.13}$$

Where each cross section depends on all the kinematic variables given. Within a given model (version of GENIE), $A_{QE} = A_{MEC} = A_{RES} = A_{DIS} = 1$. The basic idea is to use the joint distribution of all five variables to adjust A_{QE}, A_{MEC}, A_{RES}, and A_{DIS} to produce a new model that describes the data best.

Much of the same physics can be accessed by removing the absolute normalization, which is largely determined by the imprecisely known flux, and fitting the number of events in a discrete five-dimensional bin of $\vec{\Omega}$ referred to as $\Delta\vec{\Omega}_i$. The number of expected events from process q can be expressed as

$$n_{q,i} = A_q \sum_X \int dE' \phi\left(E'\right) \int d\vec{\Omega}' R_q\left(\vec{\Omega}', \Delta\vec{\Omega}_i\right) \frac{d\sigma_q\left(\mu pX; E', \vec{\Omega}'\right)}{d\vec{\Omega}'}, \tag{7.14}$$

where E' is the neutrino energy, $\phi\left(E'\right)$ is the flux, $\frac{d\sigma_q\left(\mu pX; E', \vec{\Omega}'\right)}{d\vec{\Omega}'}$ is the differential cross section for the kinematics $\vec{\Omega}'$ for process q, and $R_q\left(\vec{\Omega}', \Delta\vec{\Omega}_i\right)$ is the probability that an event with kinematics $\vec{\Omega}'$ in process q lands in bin $\Delta\vec{\Omega}_i$.

One can also compute the number of events in bin i for process q in a particular model via Monte

Carlo techniques, generating a set of simulated events for each process q in bin i, $m_{q,i}$:

$$m_{q,i} = \rho \sum_X \int dE\phi\left(E'\right) \int d\vec{\Omega}' R_q\left(\vec{\Omega}', \Delta\vec{\Omega}_i\right) \frac{d\sigma_q\left(\mu pX; E', \vec{\Omega}'\right)}{d\vec{\Omega}'}, \tag{7.15}$$

with ρ the expected MC-to-data ratio. This implies

$$n_{q,i} = A_q \frac{m_{q,i}}{\rho}. \tag{7.16}$$

Define N_q as the total number of events observed for process q in data, and M_q as the total number of MC events for the same process:

$$N_q = \sum_i n_{q,i} = A_q \frac{M_q}{\rho}. \tag{7.17}$$

One can use these expressions to replace A_q with the number of events attributed to process q in the sample:

$$A_q = \frac{\rho N_q}{M_q}, \tag{7.18}$$

and so

$$n_{q,i} = N_q \frac{m_{q,i}}{M_q}. \tag{7.19}$$

One then fits for the number of events N_q of each type q found within the overall sample events; these are the "observables". This is a type of "template" fit.

From these, one can also obtain the fraction of any event type f_q:

$$f_q = \frac{N_q}{\sum_{q'} N_{q'}}. \tag{7.20}$$

Most results in this analysis will be given in terms of these event fractions, as they are somewhat simpler to interpret.

With the fitted N_q, one can compute A_q, the scaling factor to be applied to the cross section model to best match the data. Since the data-to-MC normalization factor ρ is common for all processes, one can use one of them, QE for example, to extract the relative scaling factors

$$\frac{A_q}{A_{QE}} = \frac{N_q}{N_{QE}} \frac{M_{QE}}{M_q}, \tag{7.21}$$

which may be less sensitive to systematic uncertainties in flux.

Provided that a set of A_q lead to a successful fit to the data, one can also produce measured values

of the sub-process cross sections, at least over the acceptance of the measurement. For example,

$$\langle \sigma_{QE} \rangle = A_{QE} \langle \hat{\sigma}_{QE} \rangle \,, \tag{7.22}$$

where $\langle \sigma_{QE} \rangle$ is the extracted cross section and $\langle \hat{\sigma}_{QE} \rangle$ is the model cross section. The physical μpX cross section can likewise be extracted:

$$\langle \sigma_{\mu pX} \rangle = A_{QE} \langle \hat{\sigma}_{QE} \rangle + A_{RES} \langle \hat{\sigma}_{RES} \rangle + A_{DIS} \langle \hat{\sigma}_{DIS} \rangle + A_{MEC} \langle \hat{\sigma}_{MEC} \rangle \,. \tag{7.23}$$

For these purposes, the model cross sections are simply used as interpolating functions.

A more sophisticated variant of this method would be to allow only parameters internal to the cross section models, denoted as $\vec{\mu}$, to vary. That is, starting with a nominal set of cross section parameters $\vec{\mu}_0$, find the best values of $\vec{\mu}$ using the observed distribution of $\vec{\Omega}$. GENIE has many ($\sim$35) such parameters; for example, the CC-QE axial vector mass M_A^{CCQE} would be one element of $\vec{\mu}$. The grand ambition would be to find the $\vec{\mu}$ that best fits MicroBooNE data, along with the accompanying error matrix on $\vec{\mu}$. This would, in turn, define the best possible model of GENIE for MicroBooNE data, and it would meaningfully quantify how much GENIE parameters could be varied. Or, keeping an open mind, the exercise might show that no parameter adjustment can make GENIE describe the data.

7.6 Fitting Method

The data is organized into $4^5 = 1024$ bins in $\vec{\Omega}$, using a scheme where each of the elements in $\vec{\Omega}$, $(T_\mu, T_p, \cos\theta_\mu, \cos\theta_p, \Delta\varphi_{\mu p})$, is placed in one of four bins. The bin boundaries, summarized in Table 7.3, are chosen to contain equal numbers of events in each one-dimensional projection in the Monte Carlo (see Appendix B), using the nominal flux$\otimes$cross section$\otimes$detector model for the experiment. Here "$\otimes$" indicates the convolution process. For simplicity, the five-dimensional histogram is "flattened " into a 1024 element one-dimensional histogram, denoted as "X_D" for data as shown in Fig. 7.6.

Table 7.3: Bin definitions for inclusive CC proton production 5D phase space.

Head	Bin 1	Bin 2	Bin 3	Bin 4
T_μ	[0.0, 0.20)	[0.20,0.30)	[0.30, 0.46)	[0.46, 2.0)
T_p	[0.0, 0.09)	[0.09,0.15)	[0.15,0.21)	[0.21, 1.5)
$\cos\theta_\mu$	[-1.0, 0.48)	[0.48, 0.75)	[0.75, 0.89)	[0.89, 1.0)
$\cos\theta_p$	[-1.0, 0.42)	[0.42, 0.66)	[0.66, 0.85)	[0.85, 1.0)
$\lvert\Delta\varphi_{\mu p}\rvert$	[0.0, 2.17)	[2.17, 2.98)	[2.98, 3.28)	[3.28, 6.3)

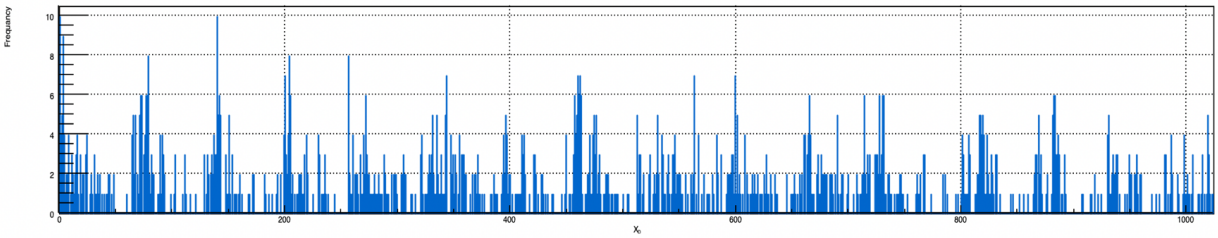

Figure 7.6: The index histogram for on-beam data, "X_D".

7.6.1 Inclusive CC contributions

Histograms with the same binning as the data are produced using the Monte Carlo simulation for each of the four dominant sub-nuclear cross section elements. These "template" histograms are denoted "X_{QE}", "X_{RES}", "X_{DIS}", and "X_{MEC}" for quasielastic, resonance, deep inelastic, and $2h2p$ processes, respectively. Figure 7.7 shows "X_{QE}", "X_{RES}", "X_{DIS}", and "X_{MEC}" templates, respectively as described in Appendix B.

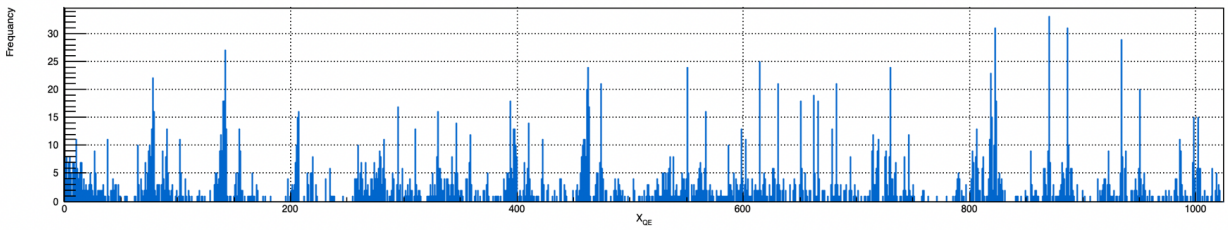

(a)

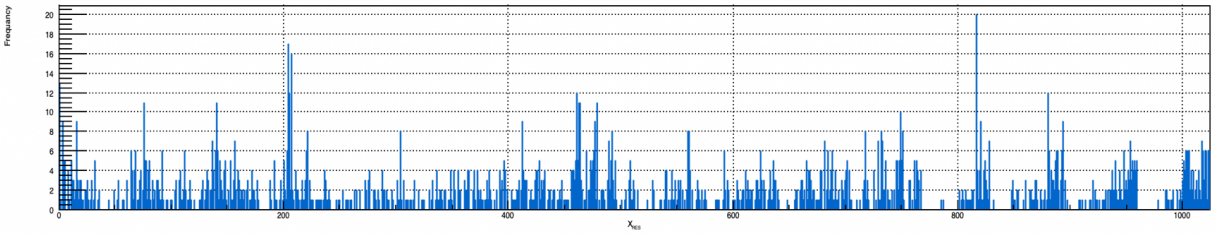

(b)

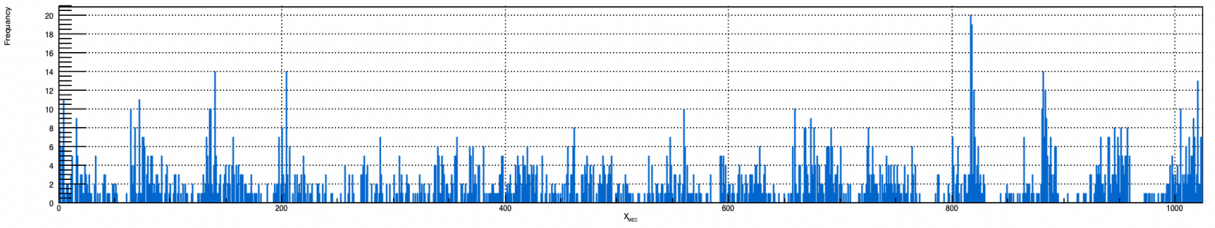

(c)

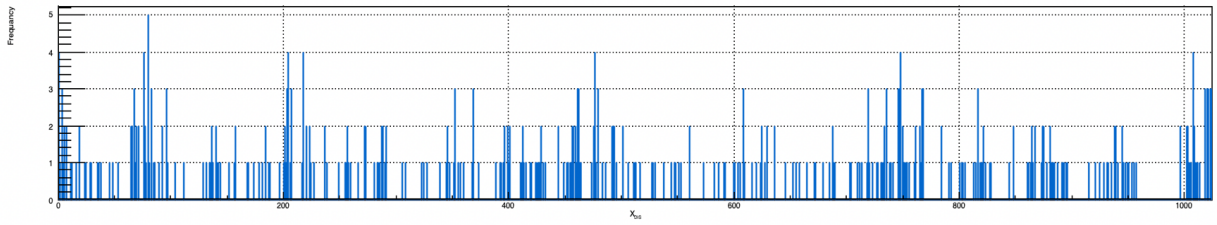

(d)

Figure 7.7: The index histogram for simulated (a) QE events "X_{QE}", (b) RES events "X_{RES}", (c) DIS events "X_{DIS}", and (d) MEC events "X_{MEC}".

7.6.2 Cosmic ray backgrounds

Cosmic ray interactions can occasionally mimic the μpX final state. The distribution of these events can be determined using off-beam data, allowing an empirical determination of a 1024 element cosmic ray template histogram "X_{CR}" as shown in Fig. 7.8. This histogram has a distinct structure compared to those of the neutrino processes, which allows the level of CR events in the data to be directly extracted along with the neutrino contributions.

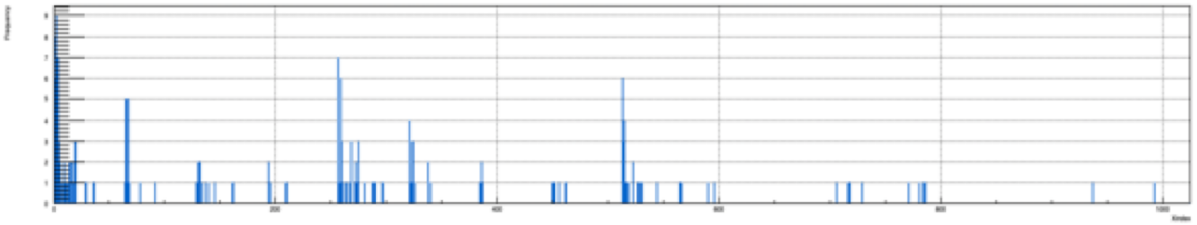

Figure 7.8: The index histogram for "CR", "X_{CR}".

7.6.3 Neutral current contribution

Neutral current (NC) events producing a $\pi^- p$ final state can enter the sample since the pion and muon exhibit similar energy loss and MCS scattering behavior. Final state pions produced at MicroBooNE have hadronic interaction lengths in the $10 - 100$ cm range and often inelastically scatter before they range-out or exit. This tends to suppress the NC contribution. The estimated level is less than 1% of all events from GENIE. No attempt is made to extract it from the data, but its contribution to systematic uncertainty is taken into account.

7.6.4 "Dirt" contribution

Muons produced by neutrino interactions in the material upstream of the cryostat could in principle mimic the μpX final state. The distribution of these "dirt" events can be estimated by simulation and used to produce a "dirt template" X_{DR} as shown in Fig. 7.9 . This is used for systematic checks.

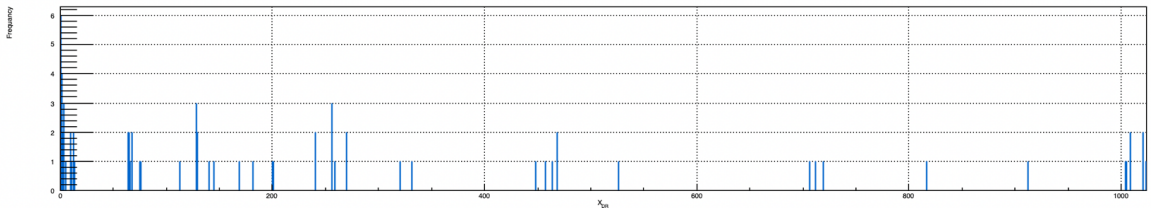

Figure 7.9: The index histogram for "Dirt", "X_{DR}".

7.6.5 Likelihood fit to index histogram

The predicted number of events for each bin of the data histogram "X_D" is taken to be

$$\mu_i = \left(f_{QE} \frac{m_{QE,i}}{M_{QE}} + f_{RES} \frac{m_{RES,i}}{M_{RES}} + f_{DIS} \frac{m_{DIS,i}}{M_{DIS}} + f_{MEC} \frac{m_{MEC,i}}{M_{MEC}} + f_{CR} \frac{m_{CR,i}}{M_{CR}} \right) N_D, \tag{7.24}$$

In this expression, $m_{QE,i}$ is the number of MC events of type QE in bin i, $M_{QE} = \sum_i m_{QE,i}$ is the total number of QE events selected in all bins, and N_{QE} is the fit parameter for the total number of QE events

found in the data. Similar definitions apply to the other terms, with the exception that $m_{CR,i}$ is the number of off-beam CR events in bin i, and M_{CR} is the total number of off-beam CR events, and N_D is the total number of events in the data histogram. The model prediction thus has five free parameters.

The parameter μ_i is assumed to be the mean value of a Poisson distribution describing the probability of observing n_i data events in bin i

$$P\left(n_i|\mu_i\right) = \frac{\mu_i^{n_i}}{n_i!}e^{-\mu_i}. \tag{7.25}$$

These probabilities are used to form an effective χ^2 from the likelihood ratio:

$$\chi^2 = -2\sum_i \left(\ln P\left(n_i|\mu_i\right) - \ln P\left(n_i|n_i\right)\right), \tag{7.26}$$

and $N_{QE}, N_{RES,}N_{DIS}, N_{MEC}$, and N_{CR}, along with their statistical covariance matrix, are estimated by minimizing the χ^2 function with respect to these parameters via the MINUIT program.

7.6.6 Validation: χ^2 tests on templates

The ability to separate the various mechanisms in the fit depends on the process templates being distinct. A χ^2 comparison test (available in ROOT) between pairs of MC templates is used to quantified these template. This comparison tests the hypothesis that two histograms derive from the same underlying true distribution. There are no free parameters. The number of degrees of freedom (ndf) is taken to be the number of bins that have at least one entry. Note that for this purpose, a high χ^2 or low p value is "good".

Tables 7.4 -7.5 summarize this study in Tune 1 and Tune 3, respectively. The QE templates differ from all others to very high statistical significance. The DIS templates are least distinct, but this is likely due to the low available statistics. Keeping the DIS term in the fit allows for a more empirical, statistically dominated treatment of this contribution; and, with an eye towards higher statistics in the future, electing to keep it.

Table 7.4: χ^2 distance test shows these templates are distinguishable, and p-value in Tune 1.

Head	χ^2 distance	ndf	p-value
"QE-RES"	2012.89	870	3.69×10^{-92}
"QE-DIS"	1446.22	773	2.11×10^{-43}
"QE-MEC"	2118.92	877	2.78×10^{-104}
"RES-MEC"	935.61	803	0.79×10^{-3}
"RES-DIS"	737.02	803	0.95
"MEC-DIS"	805.52	715	0.10×10^{-1}

Table 7.5: χ^2 distance test shows these templates are distinguishable, and p-value in Tune 3.

Head	χ^2 distance	ndf	p-value
"QE-RES"	2640.37	913	2.72×10^{-167}
"QE-DIS"	1822.78	827	8×10^{-77}
"QE-MEC"	2084.26	856	6.7×10^{-104}
"RES-MEC"	889.393	766	0.12×10^{-2}
"RES-DIS"	780.122	745	0.18
"MEC-DIS"	605.06	745	0.9

7.6.7 Validation: Truth level studies

The fit procedure was tested in summer 2018 using truth level quantities and application of cuts that roughly match the full reconstruction level analysis [58]. There are two tests. The focus of these studies was to test whether they could distinguish between three cross-section contributions, QE+RES+MEC, and four contributions, QE+RES+DIS+MEC. A closure test was performed along the way.

These tests implement efficiency with two different models: a "step function" efficiency curve with zero efficiency for $T_\mu \left|\cos\theta_\mu\right| < 70$ MeV or $T_p \left|\cos\theta_p\right| < 70$ MeV, and a 100% efficiency for other cases. This condition approximately corresponds to the acceptance for muons with ≥ 50 CP hits and protons with ≥ 15 CP hits. Assuming "perfect" particle identification, this scheme allowed one to use $750,000$ MC events for $10,000$ simulated "data" events.

Table 7.6: Fit results based on a "step function" efficiency model with perfect particle ID.

Head	No DIS	With DIS	Input
QE/Total	0.397 ± 0.010	0.394 ± 0.010	0.396
Res/Total	0.394 ± 0.016	0.311 ± 0.021	0.311
DIS/Total	0	0.096 ± 0.017	0.082
MEC/Total	0.209 ± 0.014	0.200 ± 0.014	0.211
$\mathcal{L}$	-12740.2	-12759.4	
χ^2	915.2	873.7	
non-zero bins	878	878	

The results of three vs. four contribution fits are shown in Table 7.6. This time, all the output parameters are within 1 standard deviation of the known inputs. The χ^2 comparison to data is 41 units better with the single extra degree of freedom of the DIS contribution, and $2\Delta\mathcal{L} = 38.4$ between the two models. These numbers are consistent with a 38σ DIS signal. On the other hand, the p-value for the "no DIS" fit is still an acceptable 17%. One way to interpret this is that the procedure cannot "discover" DIS with any significance, but it can optimize the model including DIS with high significance.

In a further step, a more realistic efficiency curve based off the work in [57] is implemented. This

more realistic model exhibits much lower overall efficiency, allowing usage of only standalone GENIE, and a sample of only $\sim$70,000 MC events for the 10,000 "data" events.

Table 7.7: Fit results for parameterized energy-dependent detection efficiencies, and perfect particle identification.

Head	No DIS	DIS	Input
QE/Total	0.423 ± 0.009	0.416 ± 0.009	0.415
Res/Total	0.273 ± 0.013	0.201 ± 0.017	0.255
DIS/Total	0	0.105 ± 0.018	0.064
MEC/Total	0.303 ± 0.012	0.272 ± 0.013	0.266
$\mathcal{L}$	-17825.8	-17843.2	
χ^2	1222.59	1166.78	
non-zero bins	879	879	

The results are shown in Table 7.7. This model has more difficulty in accurately reproducing the input parameters. DIS/RES confusion exists, although DIS+RES (or QE+MEC) is unaffected. The more realistic efficiency curves further lessen in particular the differences in the distributions for RES and DIS. The overall goodness of fit is poorer, but one can trace this directly to the fact that the fit does not incorporate the effects of fluctuations in the number of MC events. This was not important in the first study which had a 75/1 MC/data event ratio. However, the fit still strongly prefers a four contribution model over a model without DIS, and MEC remains clearly separable from QE and the combination of RES+DIS.

7.6.8 Validation: Closure tests

In the closure test, the Monte Carlo is divided into two independent parts, one part representing MC events and another one representing a fake data set. For more details see Appendix B. The closure test confirms the promise of the full 5D fit formalism, which means extracted observed events without bias. It also verifies the procedure works. i.e, the fit output is consistent with known input. Table 7.8 summarizes this study.

Table 7.8: The result of fitting the production model of simulated QE, RES, DIS, and MEC events to fake data.

Head	Output		Input
QE/Total	0.412	±0.014	0.427
Res/Total	0.242	±0.013	0.236
DIS/Total	0.043	±0.006	0.06
MEC/Total	0.256	±0.013	0.276
$\mathcal{L}$	-1699.66		
χ^2	723.112		
Non-zero bins	943		

Because of the fitting model to model itself, χ^2 is very low.

7.6.9 Validation: Blinded closure tests

Further checks on the procedure were performed at the full reconstruction level. It is straightforward to take the QE, RES, DIS, MEC, and CR templates and create "fake data" with arbitrary mixtures of the processes. This step was performed by one member of the analysis team (TB), who kept the selected fractions blinded from the primary analyzer (MA) for a set of "fake experiments". The "fake data" is created by using the GENIE templates for "shape", but scaling the number of GENIE events up or down in each bin. The scaled numbers then used a Poisson mean value to create "fake experiments". The result of this exercise is summarized in Tables 7.9 and 7.10. The fit procedure successfully extracted the input parameters without significant bias.

Table 7.9: The results of fitting the production model of simulated QE, RES, DIS, and MEC events plus off-beam data to simulated data for the blind closure test.

Head	**Test1**			**Test2**			**Test3**		
	Output		Input	Output		Input	Output		Input
QE/Total	0.389	±0.023	0.376	0.434	±0.025	0.4198	0.535	±0.026	0.542
Res/Total	0.202	±0.025	0.193	0.180	±0.026	0.215	0.323	±0.028	0.321
DIS/Total	0.0526	±0.015	0.0560	0.065	±0.017	0.060	0.082	±0.017	0.068
MEC/Total	0.219	±0.026	0.239	0.283	±0.027	0.278	0.030	±0.017	0.028
Cosmic/Total	0.137	±0.012	0.135	0.034	±0.008	0.028	0.029	±0.007	0.041

Table 7.10: The results of fitting the production model of simulated QE, RES, DIS, and MEC events plus off-beam data to simulated data for the blind closure test.

Head	**Test4**			**Test5**		
	Output		Input	Output		Input
QE/Total	0.343	±0.023	0.326	0.291	±0.021	0.288
Res/Total	0.228	±0.028	0.198	0.274	±0.027	0.274
DIS/Total	0.204	±0.021	0.209	0.0366	±0.015	0.062
MEC/Total	0.201	±0.028	0.227	0.361	±0.028	0.344
Cosmic/Total	0.024	±0.008	0.039	0.035	±0.008	0.032

7.6.10 Validation: Fitting the model to off-beam data

As a test, fitting the GENIE model is to off-beam data, excluding the CR contribution. Since there are no neutrino events in the off-beam data, this test picks out the neutrino events types that are most similar to CR. Perhaps not surprisingly, these are the QE events. Table 7.11 summarizes this study.

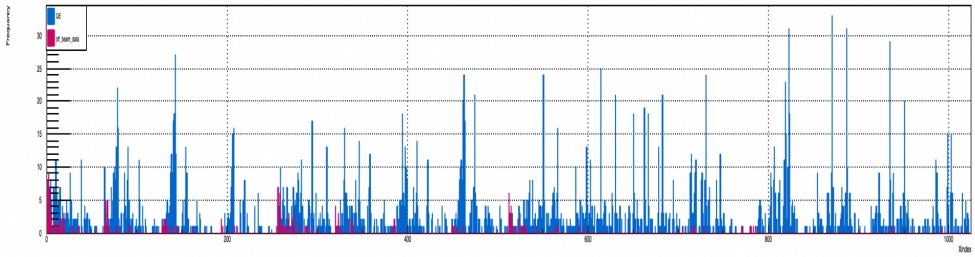

Figure 7.10: The index histogram of fitting the production model of simulated QE, RES, DIS, and MEC events to off-beam data.

As shown in Fig. 7.11 if the full index histogram of the fitting of the production model of simulated QE, RES, DIS, and MEC events to off-beam data is divided into four columns of 256 bins. The left group of 64 bins are low energy muon plus low energy proton ("LEE" region), in which the CRs are most present. In this region $\cos\theta$ is less than zero. An expected result is seen since the CRs tend to concentrate at $\cos\theta$ less than zero, where the lowest $\cos\theta$ bins span the interval $\approx (-1, +0.4)$ for both tracks, and include $\cos\theta \approx 0$ events.

Figure 7.11: The sub-histograms of fitting the simulated QE events to off-beam data, where the cosmic background most likely affects the "QE" simple in the production model.

Table 7.11: The result of fitting the production model of simulated QE, RES, DIS, and MEC events to off-beam data.

Head	Output	
QE/Total	0.468	±0.07
Res/Total	0.139	±0.06
DIS/Total	0.174	±0.06
MEC/Total	0.175	±0.06
$\mathcal{L}$	470.4	
χ^2	130.59	
Non-zero bins	937	

Moreover, fitting the production model of simulated QE, RES, DIS, and MEC events to off-beam data does not describe off-beam especially at high E_ν within a shape comparison in this analysis, in which the shape of "X_{CR}" template histogram is close to the shape of the "QE" template histogram, but it differs from others.

7.6.11 Validation: Fitting tune 3 with tune 1

The validation studies have employed "tune 1" of GENIE (v2.12.10 DefaultPlusMCWith NC, with "empirical MEC"). The closure tests are in some part "tune 1 vs. tune 1"; and one might argue that they demonstrate only self-consistency. Therefore, a closure test of "tune 1 vs. tune 3" (v2.12.10 ValenciaQEBergerSehgalCOHRES, with the "theory-driven" Valencia QE+MEC model in MCC8) is performed.

An immediate complication in this test is that the tune 3 MC sample was generated with GENIE bugs. These mainly appear to affect the QE part, and they appear to have a modest impact on many distributions. However, one should note that a "corrected tune 3" resulted in much better agreement between data and MC in the CC-inclusive analysis (with the caveat that the agreement is still not good). The situation thus appears murky.

Nevertheless, the test using tune 1 templates to fit tune 3 "fake data" uses performed proceeding. First results are shown in Table 7.12. The upshot is that the closure test fails. The fit gets the QE and DIS fractions right (and hence the sum of RES and MEC), but, while it lowers the MEC fraction considerably, it does not match the input fraction of 10.4%.

Table 7.12: The results of fitting the production model of simulated QE, RES, DIS, and MEC events in Tune 1 to Tune 3.

Head	Output		Input
QE/Total	0.508	±0.010	0.518
Res/Total	0.236	±0.010	0.307
DIS/Total	0.064	±0.006	0.069
MEC/Total	0.167	±0.010	0.105
$\mathcal{L}$	−10501.1		
χ^2	1110.13		

Tune 3 is radically different from tune 1 for MEC [55]. The tune 1 MEC fraction is 2.4× the tune 3 fraction; the tune 1 some RES fraction is 70% of the tune 3 fraction. The different levels would not be an issue for this method, except the MEC kinematic distributions also differ significantly between tunes 1 and tunes 3. In the fits, the templates must be reasonably close between model and "data" for the method to work, and the tune 1, tune 3 MEC difference looks too big to satisfy this requirement.

7.6.12 χ^2 tests for consistency with GENIE

The likelihood fit yields a set of best-fit parameters, denoted

$$\vec{h}_0 = (f_{QE0}, f_{RES0}, f_{DIS0}, f_{MEC0}, f_{CR0}) \,, \tag{7.27}$$

and a statistical covariance matrix for these parameters $\mathbf{E}^{(STAT)}$. Inclusion of flux, cross section, and detector related systematic errors described in Section 8 allows the construction of a total covariance matrix

$$\mathbf{E}_{TOT} = \mathbf{E}^{(STAT)} + \mathbf{E}^{(FLUX)} + \mathbf{E}^{(XSEC)} + \mathbf{E}^{(DET)}. \tag{7.28}$$

This matrix can be used to construct a χ^2 that tests the best fit hypothesis against other hypotheses, denoted

$$\vec{h}_0 = (f_{QE}, f_{RES}, f_{DIS}, f_{MEC}, f_{CR}) \,, \tag{7.29}$$

and thus

$$\chi^2_{TOT} = \left(\vec{h} - \vec{h}_0\right)^T \mathbf{E}^{-1}_{TOT} \left(\vec{h} - \vec{h}_0\right). \tag{7.30}$$

Two sets of alternative hypotheses will be considered: (1) the default GENIE prediction for $\vec{h}$ and (2) null hypothesis for each sub-process. For example, the null hypothesis for MEC is

$$\vec{h}_{0MEC} = (f_{QE}, N_{RES}, f_{DIS}, 0, f_{CR}) \,. \tag{7.31}$$

For the null tests the non-null parameters (e.g., for $\vec{h}_{0MEC}$, these are f_{QE}, f_{RES}, f_{DIS}, and f_{CR}) are allowed varying to minimize χ^2_{TOT}. This procedure yields a significance for a particular null hypothesis. For $\vec{h}_{0MEC}$, e.g., this would be

$$N_\sigma = \sqrt{\chi^2_{0MEC}}, \tag{7.32}$$

where χ^2_{0MEC} is the minimum value of χ^2_{TOT} obtained by varying the non-null parameters. For example, a value of $N_\sigma = 3$ for $\vec{h}_{0MEC}$ would rule out this hypothesis at "3 sigma".

7.7 Fit Results and Statistical Uncertainties

7.7.1 Process Fractions in Tune 1

Table 7.13 shows the result of fitting the production model of simulated QE, RES, DIS, and MEC events plus off-beam data to on-beam data. In this fitting result as shown in Fig. 7.12, bins for which the model production is zero, is ignored, the data is usually zero for this bin as well. The overall goodness of fit is poor taking into account only statistical errors. Section 9 describes goodness of fit that incorporates systematic uncertainties. The fitted CR fraction is an order of magnitude 5% indicating that influence (mostly in "QE" as discussed in Section 7.6.10) will be small.

Table 7.13: The results of fitting the production model of simulated QE, RES, DIS, and MEC events plus off-beam data to on-beam data.

Head	Output	
QE/Total	0.436	±0.025
Res/Total	0.179	±0.024
DIS/Total	0.055	±0.015
MEC/Total	0.259	±0.026
Cosmic/Total	0.056	±0.009
$\mathcal{L}$	650.146	
χ^2	1300	
Non-zero bins	956	

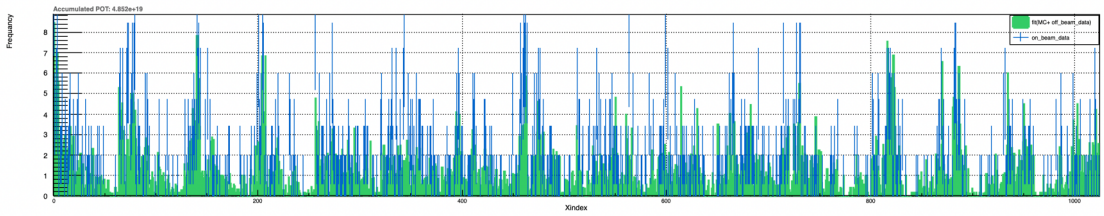

Figure 7.12: The index histogram of fitting the production model of simulated QE, RES, DIS, and MEC events plus off-beam data to on-beam data.

Figure 7.13 compares the full 1024-bin flattened histogram of data events to the best-fit prediction. The full histogram is divided into four 256-bin histograms for greater visibility. Each sub-histogram corresponds to a unique muon kinetic energy bin, and groups of 64 bins in each sub-histogram correspond to proton kinetic energy bins. For example, the first 64 bins of the top sub-histogram include the lowest kinetic energy muon and proton events (corresponding roughly to the MicroBooNE "low energy excess", or LEE, region). The last 64 bins in the bottom sub-histogram correspond to the highest kinetic energy muon and proton events.

Figure 7.13: The sub-histograms of fitting the production model of simulated QE, RES, DIS, and MEC events plus off-beam data to on-beam data.

A possible discrepancy between GENIE and on beam data in the resonance channel is observed as shown in Table 7.8 and Table 7.13. Table 7.14 summarized the significance χ^2 assume one degree of freedom of each of these processes ("QE", "RES", "DIS", and "MEC") contribution to the cross section. A "MEC" contribution appears with high statistical significance. In order to test the statistical significance of each contribution to the cross section, four fits would be performed with one contribution fix to zero.

Table 7.14: The results of fitting the production model of simulated QE, RES, DIS, and MEC events plus off-beam data to on-beam data and without the contribution of simulated "QE", "RES", "DIS", and "MEC" events to the cross section, respectively.

Head	Default		No QE		No RES		No DIS		No MEC	
QE/Total	0.436	±0.025	0.001	±0.5	0.485	±0.025	0.445	±0.025	0.501	±0.025
Res/Total	0.179	±0.024	0.364	±0.024	0.001	±0.5	0.193	±0.024	0.316	±0.024
DIS/Total	0.055	±0.015	0.111	±0.015	0.0792	±0.015	0.001	±0.5	0.093	±0.015
MEC/Total	0.259	±0.026	0.386	±0.026	0.351	±0.025	0.283	±0.026	0.001	±0.5
Cosmic/Total	0.056	±0.009	0.062	±0.009	0.057	±0.009	0.059	±0.009	0.0599	±0.009
$\mathcal{L}$	650.146		1230.67		735.921		667.206		782.666	
χ^2	1300		2461.34		1471.842		1334.412		1565.332	
$\sqrt{\triangle\chi^2}$			34.07σ		13.1σ		5.84σ		16.28σ	

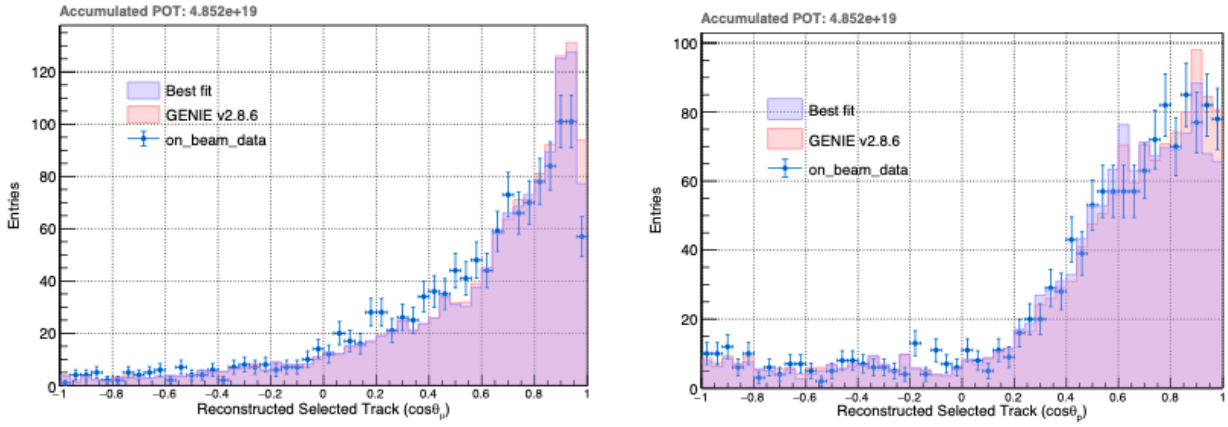

(a) (b)

Figure 7.14: Distributions of (a) $\cos\theta_\mu$ for simulated QE, DIS, and MEC events without RES plus off-beam as a result of projections to fitting result to on beam data (b) $\cos\theta_p$.

Figure 7.14 shows an effect of removing a sub-process, "RES". In this case, the RES event cluster at high $\cos\theta_\mu$ and at high $\cos\theta_p$.

7.7.2 Process Fractions in Tune 3

Fitting to data was also performed using Tune 3 templates as shown in Fig. 7.15. Results are given in Table 7.15.

Table 7.15: The results of fitting the production model of simulated QE, RES, DIS, and MEC events in Tune 3 plus off-beam data to on-beam data.

Head	Output	
QE/Total	0.535	±0.027
Res/Total	0.211	±0.026
DIS/Total	0.059	±0.016
MEC/Total	0.112	±0.021
Cosmic/Total	0.065	±0.009
$\mathcal{L}$	646.375	
χ^2	1292.75	
Non-zero bins	957	

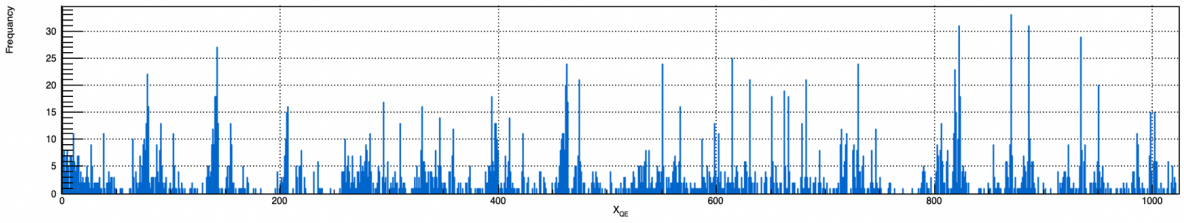

(a)

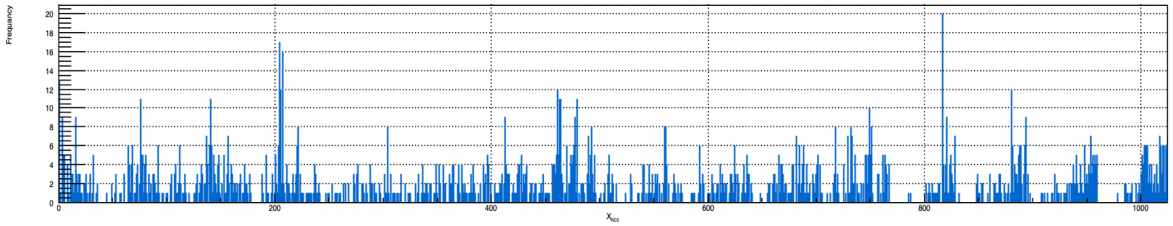

(b)

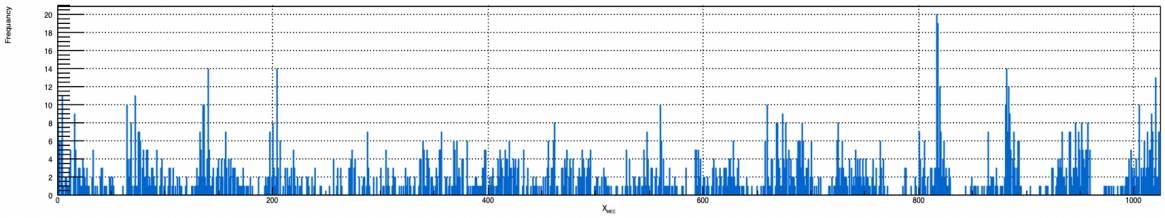

(c)

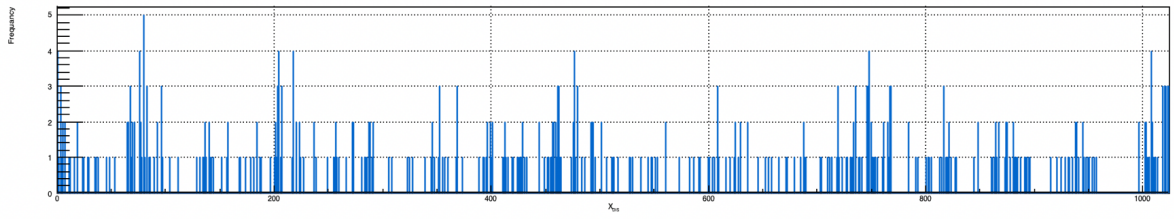

(d)

Figure 7.15: The index histogram for simulated (a) QE events "X_{QE}", (b) RES events "X_{RES}", (c) DIS events "X_{DIS}", and (d) MEC events "X_{MEC}" in tune 3.

Chapter 8

Systematic Uncertainties

8.1 Introduction

The three main categories of systematic uncertainties in the MicroBooNE experiment are beam flux, cross section, and detector systematics. The total covariance matrix $(E_{q,q'})_{TOT}$ is a sum of the statistical and systematic uncertainties:

$$(E_{q,q'})_{TOT} = E^{(STAT)}_{q,q'} + E^{(SYS)}_{q,q'}, \tag{8.1}$$

where $E^{(STAT)}_{q,q'}$ the covariance matrix is obtained from the MINUIT fitting result to the on-beam data, $E^{(SYS)}_{q,q'}$ is the total systematic covariance matrix, and q, q' refer to sub-process.

The total systematic covariance matrix is a sum of the flux, cross section and detector systematic uncertainties:

$$E^{(SYS)}_{q,q'} = E^{(FLUX)}_{q,q'} + E^{(XSEC)}_{q,q'} + E^{(DET)}_{q,q'}, \tag{8.2}$$

where $E^{(FLUX)}_{q,q'}$ the covariance matrix is obtained from the combination of flux unisims technique for non hadronic and the flux a multisim technique for hadronic production, $E^{(XSEC)}_{q,q'}$ the covariance matrix is obtained from the cross section unisims technique, and $E^{(DET)}_{q,q'}$ the covariance matrix is obtained from the detector unisims technique [56].

The covariance matrix for each of these three categories of systematic uncertainties between process types q and $q^{'}$ for all systematic source j and $j^{'}$ is

$$E_{q,q'} = \frac{1}{N_U} \sum_{i=1}^{N_U} \sum_{j=1}^{N_s} \sum_{j'=1}^{N_s} (f_{q,i,j} - f_{q,0})(f_{q',i,j'} - f_{q',0}), \tag{8.3}$$

where N_U is the number of the "universe", $f_{q,i,j}$ is the relative fraction of the process q within the systematic sources j and the universe i, and $f_{q,0}$ is the central value of the relative fraction of the process

q.

The correlation matrix for each of these three categories of systematic uncertainties between process types q and $q^{'}$ for all systematic source j and $j^{'}$ is

$$C_{q,q'} = \frac{E_{q,q'}}{\sqrt{E_{q,q}E_{q',q'}}}. \tag{8.4}$$

This chapter discusses the systematic uncertainties related to beam flux in Section 8.2, cross section in Section 8.3, and detector in Section 8.4, then it summarizes the systematic uncertainties in Section 8.6.

8.2 Flux Systematic Uncertainties

In order to estimate the flux systematic error, MicroBooNE utilizes the MiniBooNE framework as described in [33], and in Section 5.3.

The flux uncertainties can be classified into two categories:

1. Hadron production: secondary particles (π^+, π^-, K^+, and K^0) are produced when proton hits the beryllium target.

2. Non-hadron production: mismodeling of horn current distribution, horn current miscalibration, pion and nucleon total, inelastic, and quasielastic scattering cross section on beryllium [33].

In this analysis, the flux directly affects the values of A_q inferred from the fits to N_q. The N_q values themselves, or ratio quantities like A_q/A_{QE} could have a weaker, but non-negligible flux dependence. For example, a flux variation that resulted in more high E_ν events would affect the number of predicted DIS vs. RES events.

The procedures done to estimate the flux systematic uncertainties are:

- Considering the relative fraction of each nucleon level process model from the fitting result to on-beam data as the central value.

- Considering the new relative fraction of each nucleon level process model from the fitting result as the relative fraction of each nucleon level process within the hadronic parameters (π^+, π^-, K^+, and K^0) and non-hadronic parameter evaluated in universe i.

- Taking the difference in parameters relative to the central value of the relative fraction of each nucleon level process model result as an estimate of the hadron and non-hadron systematic uncertainties.

8.2.1 Hadron Production

The flux uncertainties are to be of the order of magnitude 2.5% for RES, MEC, and DIS fractions and almost small order of magnitude for the QE fraction as shown in Table 8.1 . This behavior is attributed to the distinct transverse momentum conserving signature of "QE" final states, which holds for any energy. The fit seems to make some use of the neutrino energy dependence (E_ν roughly tracks, for example, with $T_p + T_\mu$ and with $T_\mu\,(1 - \cos\theta_\mu)$).

The π^+ production parameters dominate the flux error budget, This is an expected result because most neutrino comes from π^+. Figure 8.1 shows a cartoon of neutrino beam sources.

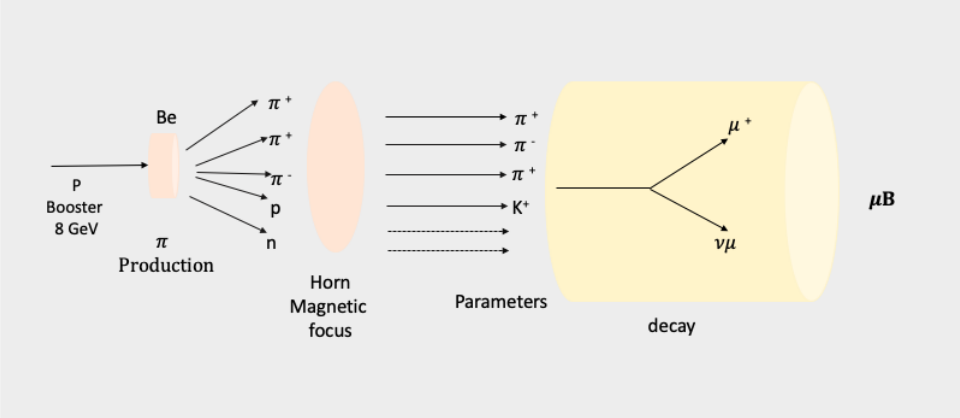

Figure 8.1: Cartoon of neutrino beam sources.

Other hadron production parameters have small effects. The largest of these is a 0.3% contribution to the DIS fraction from K^+, as might be expected since K^+ influence the higher E_ν events that contribute most to DIS. The beamline parameter contributions are all fairly small, with DIS affected most (0.8%).

Table 8.1: Flux uncertainties (the relative error) (hadron production and the total of hadron production parameters) for the relative fraction of each nucleon level process model.

Head	π^+	π^-	K^+	K^0	Total
QE/Total	0.279%	0.025%	0.027%	0.048%	0.286%
Res/Total	2.723%	0.044%	0.037%	0.091%	2.73%
DIS/Total	2.501%	0.121%	0.319%	0.106%	2.53%
MEC/Total	2.419%	0.055%	0.022%	0.127%	2.42%
Cosmic/Total	1.952%	0.042%	0.203%	0.033%	1.96%

The covariance matrix for flux uncertainty (hadronic production) between process type q and $q^{'}$ for all systematic source j and $j^{'}$ as defined in Eq. 8.3 is

$$(E_{q,q'})_{Hadronic} = \begin{bmatrix} 1.52\text{E-}06 & 1.60\text{E-}06 & -6.69\text{E-}09 & -3.832\text{E-}06 & 7.15\text{E-}07 \\ 1.60\text{E-}06 & 2.15\text{E-}05 & 2.94\text{E-}06 & -2.71\text{E-}05 & 1.02\text{E-}06 \\ -6.69\text{E-}09 & 2.94\text{E-}06 & 1.56\text{E-}06 & -4.52\text{E-}06 & 1.11\text{E-}08 \\ -3.83\text{E-}06 & -2.71\text{E-}05 & -4.51\text{E-}06 & 3.86\text{E-}05 & -1.31\text{E-}06 \\ 7.15\text{E-}07 & 1.02\text{E-}06 & 1.11\text{E-}08 & -1.31\text{E-}06 & 1.33\text{E-}06 \end{bmatrix} \tag{8.5}$$

The correlation matrix for K^+ production between process types q and $q^{'}$ for all systematic source j and $j^{'}$ as defined in Eq. 8.4 is

$$(\sigma_{i,j})_{K^+} = \begin{bmatrix} 1.0 & -0.23 & -0.97 & -0.66 & 0.75 \\ -0.23 & 1.0 & 0.06 & 0.50 & -0.62 \\ -0.97 & 0.06 & 1.0 & 0.64 & -0.72 \\ -0.66 & 0.50 & 0.64 & 1.0 & -0.94 \\ 0.75 & -0.62 & -0.72 & -0.94 & 1.0 \end{bmatrix} \tag{8.6}$$

The correlation matrix for π^+ production between process types q and $q^{'}$ for all systematic source j and $j^{'}$ as defined in Eq. 8.4 is

$$(\sigma_{i,j})_{\pi^+} = \begin{bmatrix} 1.0 & 0.28 & 0.02 & -0.50 & 0.51 \\ 0.28 & 1.0 & 0.51 & -0.94 & 0.19 \\ 0.02 & 0.51 & 1.0 & -0.59 & 0.02 \\ -0.50 & -0.94 & -0.59 & 1.0 & -0.18 \\ 0.51 & 0.19 & 0.02 & -0.18 & 1.0 \end{bmatrix} \tag{8.7}$$

For instance, the correlation matrix for π^+ production indicates there is a negative correlation between "MEC" and "RES" processes, with -0.94, which means shifting the "RES" process up caused turning the "MEC" process down.

The correlation matrix for π^- production between process types q and $q^{'}$ for all systematic source j and $j^{'}$ as defined in Eq. 8.4 is

$$(\sigma_{i,j})_{\pi^-} = \begin{bmatrix} 1.0 & 0.55 & -0.68 & -0.87 & 0.51 \\ 0.55 & 1.0 & -0.29 & -0.86 & 0.16 \\ -0.68 & -0.29 & 1.0 & 0.42 & -0.89 \\ -0.87 & -0.86 & 0.42 & 1.0 & -0.28 \\ 0.51 & 0.16 & -0.89 & -0.28 & 1.0 \end{bmatrix} \tag{8.8}$$

The correlation matrix for K^0 production between process types q and $q^{'}$ for all systematic source j and $j^{'}$ as defined in Eq. 8.4 is

$$(\sigma_{i,j})_{K^0} = \begin{bmatrix} 1.0 & 0.96 & -0.94 & -0.99 & 0.91 \\ 0.96 & 1.0 & -0.98 & -0.98 & 0.99 \\ -0.94 & -0.98 & 1.0 & 0.96 & -0.98 \\ -0.99 & -0.98 & 0.96 & 1.0 & -0.98 \\ 0.91 & 0.99 & -0.98 & -0.98 & 1.0 \end{bmatrix} \tag{8.9}$$

8.2.2 Non-Hadronic

Table 8.2 summarizes non-hadronic contributions to the flux uncertainty. These have small effects.

Table 8.2: Flux uncertainties (the relative error) (non-hadronic) for the relative fraction of each of the nucleon process models in systematic variations.

Head	Relative Error
QE/Total	0.117%
Res/Total	0.32%
DIS/Total	0.502%
MEC/Total	0.232%
Cosmic/Total	0.528%

The covariance matrix for flux uncertainty (non-Hadronic) between process types q and $q^{'}$ for all systematic source j and $j^{'}$ as defined in Eq. 8.3 is

$$(E_{q,q'})_{non-Hadronic} = \begin{bmatrix} 2.53\text{E-}07 & -2.57\text{E-}07 & 5.36\text{E-}08 & -1.88\text{E-}07 & 1.40\text{E-}07 \\ -2.57\text{E-}07 & 3.11\text{E-}07 & -5.31\text{E-}09 & 1.25\text{E-}07 & -1.37\text{E-}07 \\ 5.36\text{E-}08 & -5.32\text{E-}09 & 6.18\text{E-}08 & -1.32\text{E-}07 & 5.95\text{E-}08 \\ -1.88\text{E-}07 & 1.25\text{E-}07 & -1.32\text{E-}07 & 3.52\text{E-}07 & -3.02\text{E-}08 \\ 1.40\text{E-}07 & -1.37\text{E-}07 & 5.95\text{E-}08 & -3.02\text{E-}08 & 9.64\text{E-}08 \end{bmatrix} \tag{8.10}$$

8.2.3 Total Flux Error

The total covariance matrix for flux uncertainty between process type q and $q^{'}$ for all systematic source j and $j^{'}$ is

$$(E_{q,q'})_{FLUX} = \begin{bmatrix} 1.77\text{E-}06 & 1.34\text{E-}06 & 4.69\text{E-}08 & -4.02\text{E-}06 & 8.56\text{E-}07 \\ 1.34\text{E-}06 & 2.18\text{E-}05 & 2.94\text{E-}06 & -2.70\text{E-}05 & 8.87\text{E-}07 \\ 4.69\text{E-}08 & 2.94\text{E-}06 & 1.62\text{E-}06 & -4.65\text{E-}06 & 7.06\text{E-}08 \\ -4.02\text{E-}06 & -2.70\text{E-}05 & -4.65\text{E-}06 & 3.90\text{E-}05 & -1.34\text{E-}06 \\ 8.56\text{E-}07 & 8.87\text{E-}07 & 7.06\text{E-}08 & -1.34\text{E-}06 & 1.43\text{E-}06 \end{bmatrix} \tag{8.11}$$

For just clarifying the structure of the total covariance matrix above for flux uncertainty between process type q and $q^{'}$ for all systematic source is shown in Table 8.3.

Table 8.3: The total covariance matrix for flux uncertainty between process type q and $q^{'}$ for all systematic source.

QE/Total	1.77×10^{-6}	1.34×10^{-6}	4.69×10^{-8}	-4.02×10^{-6}	8.56×10^{-7}
Res/Total	1.34×10^{-6}	2.18×10^{-5}	2.94×10^{-6}	-2.70×10^{-5}	8.87×10^{-7}
DIS/Total	4.69×10^{-8}	2.94×10^{-6}	1.62×10^{-6}	-4.65×10^{-6}	7.06×10^{-8}
MEC/Total	-4.02×10^{-6}	-2.70×10^{-5}	-4.65×10^{-6}	3.90×10^{-5}	-1.34×10^{-6}
CR/Total	8.56×10^{-7}	8.87×10^{-7}	7.06×10^{-8}	-1.34×10^{-6}	1.43×10^{-6}
	QE/Total	Res/Total	DIS/Total	MEC/Total	CR/Total

The total correlation matrix for flux uncertainty between process types q and $q^{'}$ for all systematic source j and $j^{'}$ as defined in Eq. 8.4 is

$$(C_{q,q'})_{FLUX} = \begin{bmatrix} 1.0 & 0.216 & 0.028 & -0.484 & 0.538 \\ 0.216 & 1.0 & 0.493 & -0.926 & 0.184 \\ 0.028 & 0.493 & 1.0 & -0.584 & 0.007 \\ -0.484 & -0.926 & -0.584 & 1.0 & -0.180 \\ 0.538 & 0.184 & 0.007 & -0.180 & 1.0 \end{bmatrix} \tag{8.12}$$

A notable negative correlation exists between the RES and MEC elements of the flux systematic error matrix. This indicates that the RES and MEC fractions make use of the energy dependence of the interactions and that when RES goes up, MEC goes down. Other correlations are modest.

8.3 Cross section Model

A GENIE cross section model can produce a systematic uncertainty if it changes the shape, rather than just the normalization, of any of the X_p histograms, i.e.

$$X_p \rightarrow X_p + \delta X_p \neq (1 + \delta_p)\, X_p. \tag{8.13}$$

The procedures done to estimate the cross section systematic uncertainties are:

- Considering the relative fraction of each nucleon level process model from the fitting result to on-beam data as the central value.
- Considering the new relative fraction of each nucleon level process model from the fitting result as the relative fraction of each nucleon level process within the cross section parameters evaluated in universe i.
- Taking the difference in parameters relative to the central value of the relative fraction of each nucleon level process model result as an estimate of the cross section systematic uncertainties.

Table 8.4: Cross section uncertainties (error) produced by GENIE cross section parameters for the relative fraction of each nucleon level process model.

Head	QE/Total	Res/Total	DIS/Total	MEC/Total	Cosmic/Total
qema	-0.48×10^{-2}	0.22×10^{-2}	0.21×10^{-2}	0.50×10^{-5}	0.50×10^{-3}
qevec	0.22×10^{-2}	-0.10×10^{-2}	-0.81×10^{-3}	0.17×10^{-4}	-0.39×10^{-3}
IntraNukeNinel	-0.11×10^{-1}	0.58×10^{-2}	0.58×10^{-2}	0.10×10^{-2}	0.61×10^{-3}
IntraNukeNmfp	-0.70×10^{-2}	0.22×10^{-2}	-0.32×10^{-4}	0.71×10^{-2}	-0.23×10^{-2}
IntraNukePIabs	-0.44×10^{-2}	0.34×10^{-2}	0.32×10^{-2}	-0.22×10^{-2}	0.52×10^{-4}
IntraNukePIcex	0.11×10^{-2}	-0.17×10^{-2}	0.26×10^{-3}	0.50×10^{-3}	-0.15×10^{-3}
IntraNukePIel	-0.33×10^{-3}	0.23×10^{-2}	-0.60×10^{-4}	-0.19×10^{-2}	-0.49×10^{-4}
IntraNukePIinel	0.94×10^{-3}	0.31×10^{-2}	-0.69×10^{-3}	-0.34×10^{-2}	0.71×10^{-4}
NonResRvbarp1pi	0.11×10^{-2}	0.82×10^{-3}	-0.33×10^{-2}	0.12×10^{-2}	0.16×10^{-3}
NonResRvp2pi	-0.65×10^{-3}	-0.46×10^{-3}	0.19×10^{-2}	-0.61×10^{-3}	-0.18×10^{-3}
NonResRvp1pi	-0.47×10^{-4}	-0.58×10^{-3}	0.15×10^{-2}	-0.801×10^{-3}	-0.70×10^{-4}
ResDecayEta	0.15×10^{-3}	0.14×10^{-2}	-0.36×10^{-3}	-0.12×10^{-2}	0.37×10^{-4}
ResDecayGamma	-0.30×10^{-5}	0.28×10^{-4}	0.20×10^{-6}	-0.24×10^{-4}	-0.30×10^{-6}
ResDecayTheta	0.14×10^{-2}	-0.84×10^{-3}	0.69×10^{-2}	-0.11×10^{-2}	-0.12×10^{-3}
ccresAxial	0.32×10^{-2}	-0.44×10^{-2}	-0.44×10^{-2}	0.92×10^{-4}	0.34×10^{-3}
ccresVector	0.25×10^{-2}	-0.37×10^{-2}	0.69×10^{-3}	0.28×10^{-3}	0.25×10^{-3}
FormZone	0.88×10^{-4}	0.13×10^{-4}	0.99×10^{-3}	-0.24×10^{-2}	0.11×10^{-4}
DISCv2u	0.10×10^{-5}	-0.25×10^{-4}	0.59×10^{-4}	-0.28×10^{-4}	-0.64×10^{-5}
DISCv1u	-0.40×10^{-5}	0.23×10^{-4}	-0.49×10^{-4}	0.25×10^{-4}	0.60×10^{-5}
DISBth	-0.32×10^{-4}	0.25×10^{-4}	-0.17×10^{-4}	0.15×10^{-4}	0.10×10^{-4}
IntraNukeNabs	-0.84×10^{-2}	0.48×10^{-3}	0.12×10^{-2}	0.47×10^{-2}	0.20×10^{-2}
IntraNukeNcex	-0.70×10^{-2}	-0.44×10^{-3}	-0.13×10^{-2}	0.91×10^{-2}	-0.36×10^{-3}
IntraNukeNel	0.28×10^{-1}	-0.13×10^{-2}	-0.67×10^{-2}	-0.44×10^{-2}	-0.35×10^{-2}

Changing the probability for proton eleastic scattering ("IntraNukeNel") in the FSI model produces the biggest effect, lowering the QE fraction by 6.6% and raising the other fractions by corresponding amounts as shown in Table 8.4. The intuitive explanation for this is that enhanced scattering of the proton in the nuclear medium from a QE event shifts the kinematics away from the characteristic μp co-planar topology that the fit is able to exploit. Table 8.5 summarizes the contributions.

Table 8.5: Cross section uncertainties (the relative error) for the relative fraction of each nucleon level process model.

Head	Relative Error
QE/Total	7.91%
Res/Total	8.72%
DIS/Total	18.1%
MEC/Total	5.53%
Cosmic/Total	8.73%

The covariance matrix for cross section uncertainty between process types q and $q^{'}$ for all systematic source j and $j^{'}$ as defined in Eq. 8.3 is

$$(E_{q,q'})_{XSEC} = \begin{bmatrix} 0.113\text{E-}02 & -0.490\text{E-}03 & -0.260\text{E-}03 & -0.276\text{E-}03 & -0.104\text{E-}03 \\ -0.490\text{E-}03 & 0.113\text{E-}03 & 0.115\text{E-}03 & 4.91\text{E-}05 & -4.52\text{E-}05 \\ -0.260\text{E-}03 & 0.115\text{E-}03 & 5.28\text{E-}05 & 1.41\text{-}05 & 3.03\text{E-}05 \\ -0.276\text{E-}03 & 4.91467\text{E-}05 & 1.41\text{E-}05 & 0.188\text{E-}03 & 5.62\text{E-}06 \\ -0.104\text{E-}03 & 4.51825\text{E-}05 & 3.03\text{E-}05 & 5.62\text{E-}06 & 1.05\text{E-}05 \end{bmatrix} \tag{8.14}$$

The correlation matrix for cross section uncertainty between process types q and $q^{'}$ for all systematic source j and $j^{'}$ as defined in Eq. 8.4 is

$$(C_{q,q'})_{XSEC} = \begin{bmatrix} 1.0 & -0.871 & -0.773 & -0.571 & -0.647 \\ -0.871 & 1.0 & 0.689 & 0.204 & 0.564 \\ -0.773 & 0.689 & 1.0 & 0.098 & 0.633 \\ -0.571 & 0.204 & 0.098 & 1.0 & 0.082 \\ -0.647 & 0.564 & 0.633 & 0.082 & 1.0 \end{bmatrix} \tag{8.15}$$

In general, observed any cross section change increases the QE fraction tends to decrease the other fractions.

8.4 Detector Systematic Uncertainties

Generally, this analysis used the standard procedure for MCC8 detector systematic effects [53] as will discuss in Section 8.4.3. However, this procedure treats several sources of uncertainty in an incorrect way. Some corrections for bias that result from fixing a mistake are treated as systematic errors. In these cases, applying the corrections to the data and using an estimate of the uncertainty on the correction is for systematic error. Another problem is that upper bounds on effects are used as estimates of uncertainty. This is fine for small uncertainties, but for others it is important to try to maintain the concept of $\pm 1\sigma$ as a 68% confidence(frequentist)/credibility(Bayesian) interval. Therefore, the standard procedure is revaluated in Section 8.4.1.

8.4.1 MCC8 Error Recipe

Thirteen sources of uncertainty are considered:

1. Space charge effect (dataSCE), which is slow-moving positive ions in a detector due to, for instance, ionization from cosmic rays, leading to a distortion of the electric field within the detector [59]. The central value has been adjusted to the best knowledge of a space charge model, and variation samples attempt to capture the uncertainty in the model. This analysis is followed the standard procedure by convention.

2. Light yield (LArG4BugFix). The standard procedure is not correct, but it is benign. The variation sample fixes a mistake. It should become the new central value. Since the associated systematic errors are tiny, this analysis is followed the standard procedure by convention.

3. Longitudinal diffusion (DLup and DLdn), which is the diffusion of ionization electrons in the direction parallel to the TPC electric field. The physical effect of diffusion is to spread a distribution of drifting charge in time by an amount proportional to $\sqrt{\text{time}}$, which adds a drift-time dependent contribution to the width of a hit

$$\sigma_t^2 = \sigma_E^2 + Kt. \tag{8.16}$$

The physically relevant parameter K is related to the diffusion constant by

$$K = \frac{D_L}{2v_D^3}. \tag{8.17}$$

External experimental determination of D_L brings in uncertainties on drift speed v_D(and other effects) [54] that are not relevant for the MicroBooNE experiment, and which inflate the longitudinal diffusion systematic uncertainty. Schematically, the default method uses

$$K_{\mu B} = K_{ext}\frac{v_{D,\mu B}^3}{v_{D,ext}^3}, \tag{8.18}$$

and so

$$\frac{\delta K_{\mu B}}{K_{\mu B}} = \frac{\delta K_{ext}}{K_{ext}} \oplus 3\frac{\delta v_{D,\mu B}}{v_{D,\mu B}} \oplus 3\frac{\delta v_{D,ext}}{v_{D,ext}}. \tag{8.19}$$

The second and third terms in the error should not be present. K should be extracted directly from the data.

4. Transverse diffusion (DTup and DTdn), is diffusion of ionization electrons in a direction perpendicular to the TPC electric field. The standard procedure is not correct, the two variations shift the transverse diffusion constant D_T by different amounts in the same direction. "Down" is a larger shift than "up". The explanation is that the central value of D_T corresponds to using the wrong field, so part of this systematic involves correcting a mistake. Accordingly, this analysis used (DTup+DTdn)/2 to correct the results, and used (DTdn-DTup) to estimate the uncertainty on the correction. The effect is small.

5. Wire noise (noiseAmpUp and noiseAmpUp), which the amplitude of the noise simulated on the TPC wires. This analysis is followed the standard procedure by convention.

6. PMT noise (upPEnoise and dnPEnoise), which is the rate of the single photo electron noise simulated on the PMTs. This analysis is followed the standard procedure by convention.

7. Dynamically induced charge (withDIC), which is the charge sharing between anode wires in the LArTPC. The physical anode signal results from charge induced in the wire from a superposition of all drifting ionization charge associated with a particle track. For some track topologies, this superposition can produce cancellation effects that lead to lost hits and both lower tracking efficiency and reduced charged collection, particularly in the unshielded induction plane wires closest to the drift volume. The standard procedure in estimating this is not correct. This is another case of calling the correction of a mistake a systematic error, and this is quite consequential for MCC8 analyses. Furthermore, the implementation of the variation sample is incomplete. The DIC variant sample should become the new central value, and Pandora should be retuned on this sample. A variant model of DIC should have been produced. The DIC systematic should be the difference that results from the retuned Pandora acting on the two variant DIC models. Finally, DIC produces a one-way shift by comparing the result from assuming all charge goes to the nearest wire (central value) and the charge spreads over that wire and the ten nearest neighbors (variant), yet the standard treatment assumes the central value result and a $\pm$ swing about this value, which is impossible. This in fact produces a consequential bias. The main effect of ignoring induced charge as that the track reconstruction efficiency becomes $\cos\theta$ and ϕ dependent[36]: $\cos\theta = 1$ is unaffected, and the efficiency drops with as $\cos\theta \to 0$; $\cos\theta = 0$, $\phi = 0, \pi$ are maximally affected. This analysis follows this procedure : make a correction based on the withDIC sample to remove the bias, and, in view of the lack of retuning of Pandora, keep a still very conservative uncertainty

estimate on the correction of half the shift between central value and withDIC sample.

8. Wire response (squeezeResp), which a charge induction on the TPC wires is simulated using a set of response functions. This analysis is followed the standard procedure by convention.

9. Saturated channels (deadSaturatedChannels), channels that frequently become saturated as charge builds up on capacitors in the Application Specific Integrated Circuit (ASIC), resulting in deadtime, are turned off. The variant "exaggerates the effect to provide an upper bound". An upper bound is not a $\pm 1\sigma$. However, the associates systematic error is small, so the mistake is benign. This analysis is followed the standard procedure by convention.

10. Misconfigured channels (altDeadChannels), the misconfigured channels associated with ASICs that have a different gain and shaping time than desired are turned off. The standard procedure is not correct, but it is benign. This analysis is followed the standard procedure by convention

11. Light outside TPC (enhancedexttpcvis). The light yield outside the TPC by 50% is increased. This analysis is followed the standard procedure by convention.

12. Electron lifetime (lifetime10ms). The standard procedure is not correct. The variant sample reduces the lifetime to 10 ms, the lowest lifetime for the sample in the good run list, and assumes a systematic error that is the difference between infinite lifetime and this lifetime. However, only 5% of the runs have this lifetime, and for all others the lifetime is an inderminantly high constant value. This is also a one-way shift that can introduce a bias. The data is corrected by a shift equal to $(5 \pm 5)\,\%$ of the full effect, which more accurately takes into account the relative frequency of run conditions and maintains a conservative error on the fraction of the low lifetime run.

13. Recombination (birksrecomb). The standard procedure is not correct. The central value MC models electron-ion recombination using the modified box model with parameters fit to ArgoNeuT data. This variation substitutes the Birks model with parameters tuned to "ICARUS data". ArgoNeuT's and ICARUS's E-fields were close to 500 V/m; and the procedure quoted above can yield arbitrary results, including serious underestimates. Zero error, for example, is a possible outcome. A more consistent approach would be to create a variant sample from the ArgoNeuT parameters shifted by their errors and assume the difference between the central value and variant also hold for $E = 273$ V/cm. This analysis is followed the standard procedure by convention.

8.4.2 Summary of the Modifications to MCC8 Systematic Errors

For transverse diffusion, dynamically induced charge, and electron lifetime correcting the data is for bias and using an estimate of the uncertainty on the correction is for systematic error.

Table 8.6: The bias correction and adjusted systematic errors for transverse diffusion, induced charge and electron lifetime.

Source	**Bias Correction**	**Systematic Error**
Transverse diffusion	$\frac{1}{2}(\delta_{up} + \delta_{dn})$	$\lvert\delta_{up} - \delta_{dn}\rvert$
Induced charge	δ	$\lvert\frac{\delta}{2}\rvert$
Electron lifetime	0.05δ	$\lvert 0.05\delta\rvert$

8.4.3 Default Detector Systematic Uncertainties

The procedure is done to estimate the detector systematic uncertainties:

- Using the full MC data set is to create "QE ", "RES", "DIS ", "MEC" templates as shown in Fig. 7.7.
- Fitting to each of the systematic samples using these templates, treating them as on-beam data.
- Taking the difference in parameters relative to the central value result as an estimate of the systematic errors.

Then, it would be, by convention, added the relative error in quadrature. Table 8.7 summarized the detector systematic error (the relative error) for the relative fraction of each nucleon level process model.

Table 8.7: The default detector systematic uncertainties (the relative error) for the relative fraction of each nucleon level process model.

Head	CV	Absolute error	Relative error
QE/Total	0.412	0.061	14.7%
Res/Total	0.249	0.041	15.8%
DIS/Total	0.070	0.020	26.9%
MEC/Total	0.247	0.032	12.5%
Cosmic/Total	0.008	0.015	$*$104.7%

The detector systematic uncertainties shows a large variation in the relative fraction "DIS" process with 26.9%. The relative error in the CR fraction is relative to the CORKSIKA cosmic fraction, which is very tiny (0.008) as shown in Table 8.7.

The relative detector variations is defined by

$$\sigma_{DET} = \frac{f_{q,0} - f_{q,i}}{f_{q,0}}, \tag{8.20}$$

where $f_{q,0}$ is the "central value" of the relative fraction of process q, and $f_{q,i}$ is the relative fraction of process q evaluated in the unisim MC. Observed the relative error of systematics vary between each channels. Tables 8.8, 8.10, 8.11, and 8.12 summarize the relative contribution of the total detector systematic uncertainty in each channel.

Table 8.8: The relative contribution of the total default detector systematic uncertainty in the "QE" channel.

Detector Sys variations	
cv	0.0
Space charge effect	1.93%
LArG4BugFix	0.33%
Longitudinal diffusionup	0.67%
Longitudinal diffusiondown	
Transverse diffusionup	0.015%
Transverse diffusiondown	
Squeeze Respons	0.37%
DIC	8.2%
Alterantive Dead Channel	0.65%
Saturated channels	0.02%
Electron lifetime	1.60%
PE noiseup	0.23%
PE noisedown	
Enhanced ext tpc	0.43%
birksrecomb	0.11%
nosieAmpup	0.19%
nosieAmpdown	
Total	14.7%

The detector systematic uncertainties show a large variation in the dynamic induced charge (DIC) sample. Hence, for tracks highly inclined (nearly orthogonal) to anode planes, (DIC) effects must be accounted for detailed in [59] , studies are done for the tracks moving toward the anode plane. This studies indicated some loses for the relative fraction of "QE" process for the tracks moving toward the anode plane, specifically in the interval $[0, \frac{\pi}{2})$ for the $|\Delta\varphi_{\mu p}|$ distribution as shown in Table 8.9. The top sub-histogram in Fig.8.2 is "QE" template generated for full (DIC) sample, while another one represents the "QE" template for tracks moved toward the anode plane. This is expected for "QE" process since there is some correlation in which a muon track moves toward the anode plane and the proton in the different direction, which a high fraction of time.

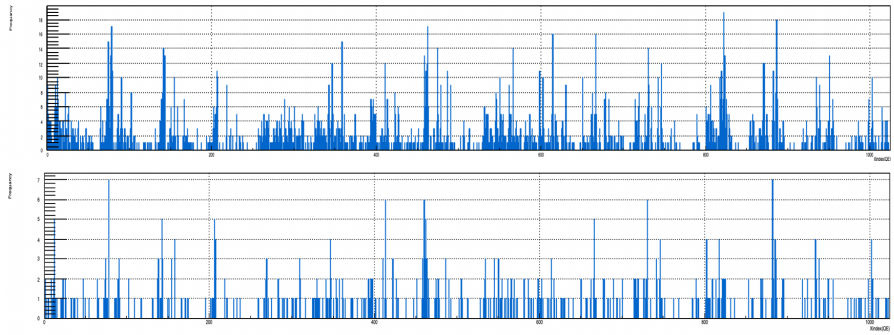

Figure 8.2: (a)The template index histogram for simulated "QE" events generated for full (DIC) sample, and (b) the template index histogram for simulated "QE" events generated for tracks moved toward the anode plane.

Table 8.9: The comparison between the relative error for the relative fraction of "QE" the full "DIC" sample and tracks moving toward the anode plane in "DIC" sample.

Head	"All tracks"	DIC sample-anode pointing
QE/Total	0.367	0.324

Table 8.10: The relative contribution of the total default detector systematic uncertainty in the "RES" channel.

Detector Sys variations	
cv	0.0
Space charge effect	4.26%
LArG4BugFix	0.02%
Longitudinal diffusionup	0.10%
Longitudinal diffusiondown	
Transverse diffusionup	0.31%
Transverse diffusiondown	
Squeeze Respons	0.18%
DIC	6.04%
Alterantive Dead Channel	0.002%
Saturated channels	0.33%
Electron lifetime	0.33%
PE noiseup	0.11%
PE noisedown	
Enhanced ext tpc	2.34%
birksrecomb	0.21%
nosieAmpup	1.55%
nosieAmpdown	
Total	15.78%

Table 8.11: The relative contribution of the total default detector systematic uncertainty in the "DIS" channel.

Detector Sys variations	
cv	0.0
Space charge effect	0.04%
LArG4BugFix	0.15%
Longitudinal diffusionup	0.28%
Longitudinal diffusiondown	
Transverse diffusionup	0.15%
Transverse diffusiondown	
Squeeze Respons	2.97%
DIC	3.83%
Alterantive Dead Channel	3.75%
Saturated channels	0.20%
Electron lifetime	11.28%
PE noiseup	0.34%
PE noisedown	
Enhanced ext tpc	0.36%
birksrecomb	3.51%
nosieAmpup	0.02%
nosieAmpdown	
Total	26.9%

Table 8.12: The relative contribution of the total default detector systematic uncertainty in the "MEC" channel.

Detector Sys variations	
cv	0.0
Space charge effect	0.10%
LArG4BugFix	0.82%
Longitudinal diffusionup	0.20%
Longitudinal diffusiondown	
Transverse diffusionup	0.01%
Transverse diffusiondown	
Squeeze Respons	0.04%
DIC	9.67%
Alterantive Dead Channel	0.24%
Saturated channels	0.33%
Electron lifetime	0.15%
PE noiseup	0.07%
PE noisedown	
Enhanced ext tpc	0.02%
birksrecomb	0.40%
nosieAmpup	0.47%
nosieAmpdown	
Total	12.52%

The covariance matrix for the default detector systematic uncertainty between process types q and $q^{'}$ for all systematic source j and $j^{'}$ as defined in Eq. 8.3

$$(E_{q,q'})_{DET} = \begin{bmatrix} 0.367\text{E-}02 & -0.180\text{E-}02 & -0.169\text{E-}03 & -0.155\text{E-}02 & -0.945\text{E-}06 \\ -0.180\text{E-}02 & 0.154\text{E-}02 & -0.986\text{E-}06 & 0.654\text{E-}03 & -0.216\text{E-}03 \\ -0.169\text{E-}03 & -0.986\text{E-}06 & 0.352\text{E-}03 & -0.116\text{E-}03 & 0.257\text{E-}06 \\ -0.156\text{E-}02 & 0.654\text{E-}03 & -0.116\text{E-}03 & 0.964\text{E-}03 & 0.253\text{E-}06 \\ -0.945\text{E-}06 & -0.216\text{E-}03 & 0.257\text{E-}06 & 0.253\text{E-}06 & 0.222\text{E-}03 \end{bmatrix} \tag{8.21}$$

The total correlation matrix for default detector uncertainty between process types q and $q^{'}$ for all systematic source j and $j^{'}$ as defined in Eq (8.4) is

$$(C_{q,q'})_{DET} = \begin{bmatrix} 1.0 & -0.761 & -0.148 & -0.831 & -0.105 \\ -0.761 & 1.0 & -0.134 & 0.540 & -0.370 \\ -0.148 & -0.134 & 1.0 & -0.200 & 0.092 \\ -0.831 & 0.540 & -0.200 & 1.0 & 0.055 \\ -0.105 & -0.369 & 0.092 & 0.055 & 1.0 \end{bmatrix} \tag{8.22}$$

8.4.4 Adjusted Detector Systematic Uncertainties

Table 8.13 summarizes the adjusted detector systematic uncertainties (the error and the relative error) for the relative fraction of each nucleon level process model. Because detector contributions dominate the systematic error budget, the modified procedure in their treatment results in considerable improvement, although the measurements remain systematics-limited.

Table 8.13: The adjusted detector systematic uncertainties (the error and the relative error) for the relative fraction of each nucleon level process model.

Head	Absolute Error	Relative error
QE/Total	0.042	10.2%
Res/Total	0.033	14.3%
DIS/Total	0.014	19.9%
MEC/Total	0.021	8.4%
Cosmic/Total	0.015	$*$105.3%

Tables 8.14, 8.15, 8.16, and 8.17 summarize the relative contribution of the total adjusted detector systematic uncertainty in each channel.

Table 8.14: The relative contribution of the total adjusted detector systematic uncertainty in the "QE" channel.

Detector Sys variations	
cv	0.0
Space charge effect	2.78%
LArG4BugFix	0.48%
Longitudinal diffusionup	0.96%
Longitudinal diffusiondown	
Transverse diffusionup	0.20%
Transverse diffusiondown	
Squeeze Respons	0.53%
DIC	2.94%
Alterantive Dead Channel	0.93%
Saturated channels	0.03%
Electron lifetime	006%
PE noiseup	0.32%
PE noisedown	
Enhanced ext tpc	0.61%
birksrecomb	0.16%
nosieAmpup	0.27%
nosieAmpdown	
Total	10.2%

Table 8.15: The relative contribution of the total adjusted detector systematic uncertainty in the "RES" channel.

Detector Sys variations	
cv	0.0
Space charge effect	5.1%
LArG4BugFix	0.02%
Longitudinal diffusionup	0.12%
Longitudinal diffusiondown	
Transverse diffusionup	0.59%
Transverse diffusiondown	
Squeeze Respons	0.22%
DIC	1.8%
Alterantive Dead Channel	0.002%
Saturated channels	0.39%
Electron lifetime	0.001%
PE noiseup	0.13%
PE noisedown	
Enhanced ext tpc	2.8%
birksrecomb	0.25%
nosieAmpup	1.8%
nosieAmpdown	
Total	13.2%

Table 8.16: The relative contribution of the total adjusted detector systematic uncertainty in the "DIS" channel.

Detector Sys variations	
cv	0.0
Space charge effect	0.06%
LArG4BugFix	0.21%
Longitudinal diffusionup	0.37%
Longitudinal diffusiondown	
Transverse diffusionup	2.75%
Transverse diffusiondown	
Squeeze Respons	4.03%
DIC	1.30%
Alterantive Dead Channel	5.09%
Saturated channels	0.27%
Electron lifetime	0.04%
PE noiseup	0.47%
PE noisedown	
Enhanced ext tpc	0.48%
birksrecomb	4.77%
nosieAmpup	0.02%
nosieAmpdown	
Total	19.85%

Table 8.17: The relative contribution of the total adjusted detector systematic uncertainty in the "MEC" channel.

Detector Sys variations	
cv	0.0
Space charge effect	0.15%
LArG4BugFix	1.22%
Longitudinal diffusionup	0.29%
Longitudinal diffusiondown	
Transverse diffusionup	0.87%
Transverse diffusiondown	
Squeeze Respons	0.06%
DIC	3.58%
Alterantive Dead Channel	0.35%
Saturated channels	0.49%
Electron lifetime	0.001%
PE noiseup	0.110%
PE noisedown	
Enhanced ext tpc	0.03%
birksrecomb	0.59%
nosieAmpup	0.70%
nosieAmpdown	
Total	8.4%

The covariance matrix for adjusted detector systematic uncertainty between process types q and $q^{'}$ for all systematic source j and $j^{'}$ as defined in Eq. 8.3

$$(E_{q,q'})_{DET} = \begin{bmatrix} 0.177\text{E-}02 & -0.294\text{E-}03 & -0.132\text{E-}03 & 0.858\text{E-}06 & -0.837\text{E-}06 \\ -0.294\text{E-}03 & 0.108\text{E-}02 & 0.909\text{E-}06 & 0.192\text{E-}03 & -0.196\text{E-}03 \\ -0.132\text{E-}03 & 0.909\text{E-}06 & 0.192\text{E-}03 & 0.192\text{E-}03 & 0.481\text{E-}06 \\ 0.857\text{E-}06 & 0.192\text{E-}03 & 0.116\text{E-}03 & 0.434\text{E-}03 & 0.356\text{E-}06 \\ -0.837\text{E-}06 & -0.196\text{E-}03 & 0.481\text{E-}06 & 0.356\text{E-}06 & 0.224\text{E-}03 \end{bmatrix} \tag{8.23}$$

The total correlation matrix for adjuested detector uncertainty between process types q and $q^{'}$ for all systematic source j and $j^{'}$ as defined in Eq (8.4) is

$$(C_{q,q'})_{DET} = \begin{bmatrix} 1.0 & -0.322 & -0.116 & -0.126 & 0.069 \\ -0.322 & 1.0 & 0.253 & 0.412 & -0.161 \\ -0.116 & 0.253 & 1.0 & 0.577 & -0.142 \\ -0.126 & 0.412 & 0.577 & 1.0 & 0.099 \\ 0.069 & -0.161 & -0.142 & 0.099 & 1.0 \end{bmatrix} \tag{8.24}$$

8.5 "Dirt"

As a result of the shape comparison in this analysis, observed the dirt fraction is consist with zero as shown in Table 8.18, so "Dirt" sample in the production model is ignored.

Table 8.18: The results of fitting the production model of simulated QE, RES, DIS, and MEC events plus off-beam data and Dirt to on-beam data.

Head	Output	
QE/Total	0.436	±0.025
Res/Total	0.179	±0.024
DIS/Total	0.055	±0.015
MEC/Total	0.259	±0.026
Cosmic/Total	0.056	±0.009
Dirt/Total	0.0048	±0.006
$\mathcal{L}$	649.727	
χ^2	1299.45	

8.6 Summary of Systematic Errors

Table 8.19 summarizes the total systematic uncertainties (the relative errors) for (the cross section, beam flux, and the default and adjusted detector systematic) and (absolute errors) for (the default and adjusted detector systematic) in each channel for phase space of inclusive CC proton production analysis.

Table 8.19: The total systematic uncertainties (the cross section, beam flux, and the default and adjusted detector systematic) in each channel for phase space of inclusive CC proton production analysis.

Head	**Xsec**	**Flux**		**Default DET**		**Adjusted DET**	
		Hadronic	**non Hadronic**	**Error**	**Relative error**	**Error**	**Relative error**
QE/Total	7.91%	0.286%	0.117%	0.061	14.7%	0.042	10.2%
Res/Total	8.72%	2.73%	0.32%	0.041	15.8%	0.032	14.2%
DIS/Total	18.1%	2.53%	0.502%	0.020	26.9%	0.014	19.9%
MEC/Total	5.53%	2.42%	0.232%	0.032	12.5%	0.021	8.4%
Cosmic/Total	8.73%	1.96%	0.528%	0.015	$*$104.7%	0.015	$*$105.2%

Chapter 9

Results

The results of the fitting procedure described in Chapter 7 to MicroBooNE on-beam data is offered in this chapter, including result with full errors in Section 9.1, projections of the kinematic variables to fitting result in Section 9.2, the significance of each process in Section 9.3, GENIE comparisons in Section 9.4, and generating a portable result in Section 9.5.

9.1 Result with Full Errors

Table 9.1 summarizes the diagonal elements of the systematic uncertainties in each channel for phase space of inclusive CC proton production analysis as discussed in Chapter 8.

Table 9.1: Summary of systematic errors on each sub-process due to uncertainties in the flux, cross section, and detector modelling. Both the total and the largest contribution for each systematic error type are given. Contributions are labelled by the following abbreviations and are described more fully in chapter 8.

source	flux		cross section		detector	
process	total	largest	total	largest	total	largest
QE	0.3%	π^+	7.9%	"IntraNukeNel"	10.2%	"DIC"
RES	2.7%	π^+	8.7%	"IntraNukeNel"	14.3%	"SCE"
DIS	2.6%	π^+	18%	"IntraNukeNinel"	19.9%	"AltDeadCha"
MEC	2.4%	π^+	5.5%	"IntraNukeNel"	8.4%	"DIC"

The relative fraction of the total systematic uncertainties (relative error)(the default detector systematic uncertainty, beam flux and the cross section) in each channel summarized in Table 9.2. The relative error in the CR fraction is relative to the CORKSIKA cosmic fraction, which is very tiny (0.008) as shown in Table 8.7. The systematic uncertainties dominate the error budget, indicating that there is little profit in this stage of the analysis to adding more data.

Table 9.2: Best-fit value, the statistical uncertainties (relative error), the total systematic uncertainties (the default detector systematic, beam flux and the cross section) (relative error) and the total of STAT and default SYS in each channel for phase space of inclusive CC proton production analysis.

Head	**Best fit**	**STAT**	**Default SYS**	**Total**
QE/Total	0.436	±5.82%	16.7%	17.7%
Res/Total	0.179	±13.32%	18.2%	22.6%
DIS/Total	0.055	±26.63%	32.5%	42.0%
MEC/Total	0.259	±10.06%	13.9%	17.2%
Cosmic/Total	0.056	±16.30%	∗105.10%	∗106.4%

Taking into account the modifications to MCC8 systematic errors related to the detector systematic as discussed in section 8.4.2 leads to this result, summarized in Table 9.3.

Table 9.3: Best-fit value plus bias correction, the statistical uncertainties(relative error) and the total systematic uncertainties (the adjusted detector systematic, beam flux and the cross section) (relative error)in each channel for phase space of inclusive CC proton production analysis.

Head	**Best fit+Bias Correction**	**STAT**	**Adjusted SYS**	**Total**
QE/Total	0.456	±5.82%	10.2%	14.2%
Res/Total	0.175	±13.32%	16.1%	20.9%
DIS/Total	0.055	±26.63%	27.0%	37.9%
MEC/Total	0.251	±10.06%	10.4%	14.4%
Cosmic/Total	0.056	±16.30%	∗105.64%	∗106.89%

Table 9.4 summarizes the results of fitting the production model of simulated QE, RES, DIS, and MEC events plus off-beam data to on-beam data, and Fig. 9.1 illustrates these results graphically. The fit yields a data-driven estimate of the CR background of approximately 5.6%. After correcting for this background the neutrino event type fractions can be compared directly to GENIE predictions.

Table 9.4: Event sub-process fractions. "Fit" refers to the results from the fit template, which includes a cosmic ray contribution. "Corrected" is the value obtained after adjusting the neutrino sub-process fractions by $1/(1 - f_{CR})$. "GENIE" is the GENIE prediction for the sub-process fractions.

Process	**Fit**	**Corrected**	**GENIE**
QE/Total	0.456 ± 0.0598	0.483 ± 0.0619	0.434
Res/Total	0.175 ± 0.0443	0.185 ± 0.0465	0.236
DIS/Total	0.055 ± 0.0228	0.058 ± 0.0235	0.056
MEC/Total	0.251 ± 0.0368	0.266 ± 0.0384	0.273
Cosmic/Total	0.056 ± 0.0181		

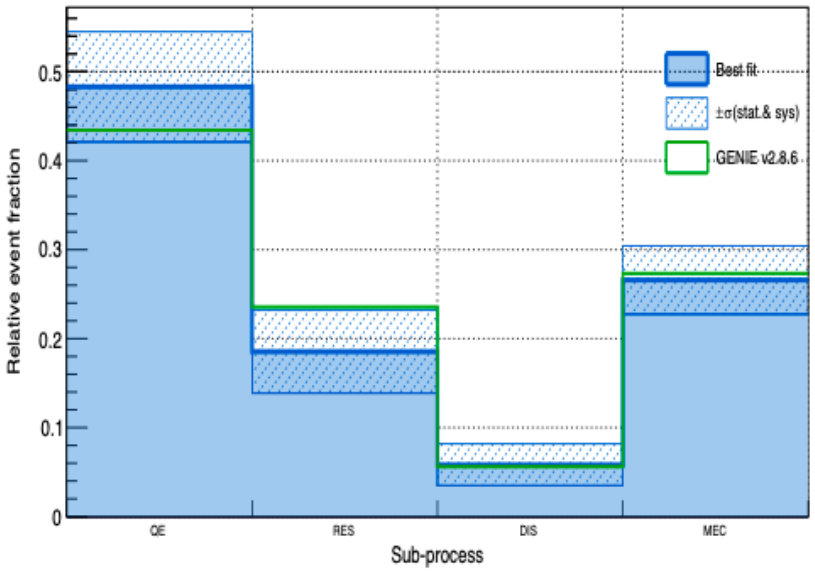

Figure 9.1: The solid histogram shows the best fit sub-process fractions for QE, RES, DIS, and MEC. The green bar shows the predicted fractions from GENIE v2.8.6. The shaded bands show the total uncertainty (statistical and systematic).

9.2 Projections of the Kinematic Variables to Fitting Result

The analysis employs coarse binning in each of the fine variables. Nevertheless, there is the ability to project the best-fit results, along with the GENIE defaults, onto any kinematic distribution, whether used in the fit or not, with any binning. Then, once can see how well a reweighting of sub-process fractions within a given GENIE tune can describe the shapes of these distributions.

By looking at "non-dynamical" distributions– vertex positions and azimuthal angles;there is also the ability to get a qualitative sense of how well the detector⊗flux model is working. The overall summary is that vertex distributions are well-described, whereas the azimuthal angles ϕ_μ and ϕ_p suffer the usual MCC8 issues due to the mismatch in DIC effects in MC and data. No evidence exists for significant CR contributions.

Because the best-fit fractions do not differ dramatically from GENIE defaults for a given tune, it is hard to see differences between best-fit and default in single distributions. For tune 1 and 3, the proton variables T_p and $\cos\theta_p$ are well described by the model. The more discriminating variables are T_μ, $\cos\theta_\mu$, and $|\Delta\phi_{\mu p}|$. For the muon variables, the models are more peaked in the forward direction than the data. Tune 3 describes the forward region better than Tune 1. However, the large QE fraction in tune 3 relative to tune 1 results in sharper $|\Delta\phi_{\mu p}|$ distribution than evident in data. Tune 1 actually does a better job with this distribution.

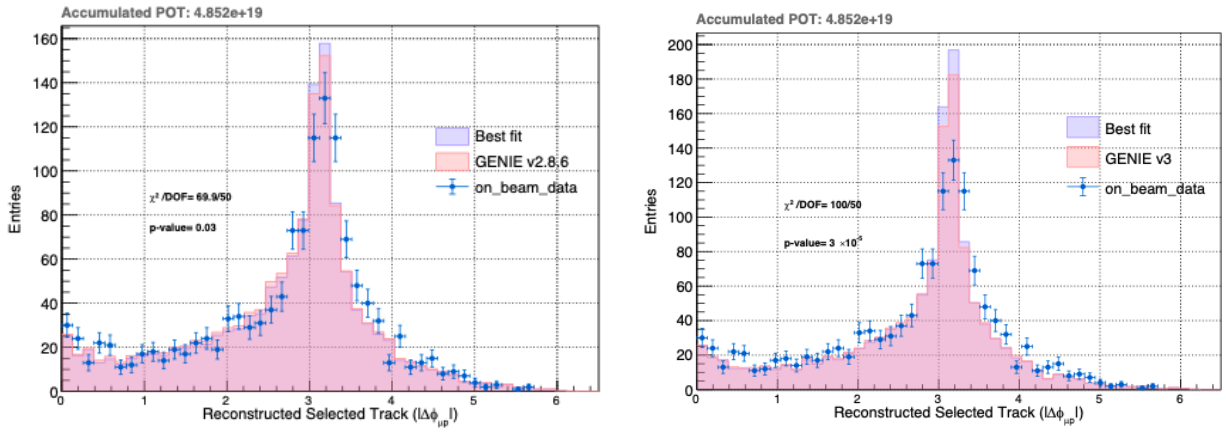

(a) (b)

Figure 9.2: Distributions of the difference in the muon azimuthal angle and the leading proton azimuthal angle $|\Delta\phi_{\mu p}|$ for simulated QE, RES, DIS, and MEC events plus off-beam as a result of projections to fitting result to on beam data (Blue), and GENIE default (Red)(a) Tune 1, and (b) Tune 3.

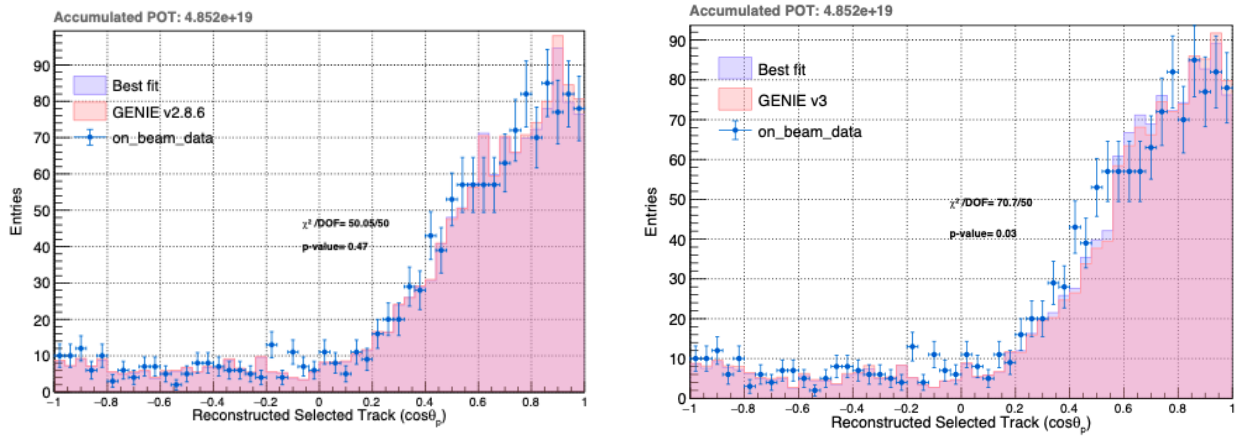

(a) (b)

Figure 9.3: Distributions of $\cos\theta_p$ for simulated QE, RES, DIS, and MEC events plus off-beam as a result of projections to fitting result to on beam data (Blue), and GENIE default (Red) (a) Tune 1, and (b) Tune 3.

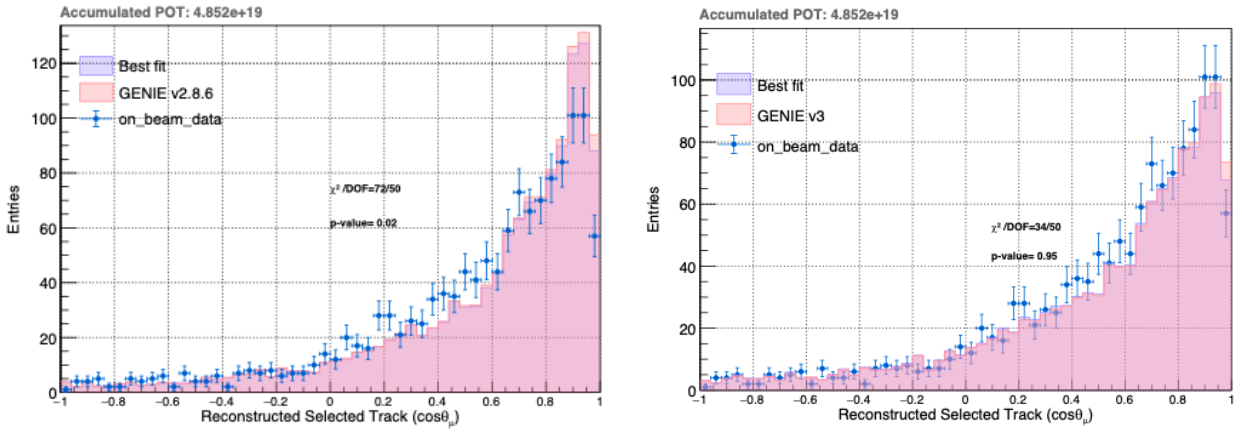

(a) (b)

Figure 9.4: Distributions of $\cos\theta_\mu$ for simulated QE, RES, DIS, and MEC events plus off-beam as a result of projections to fitting result to on beam data (Blue), and GENIE default (Red)(a) Tune 1, and (b) Tune 3.

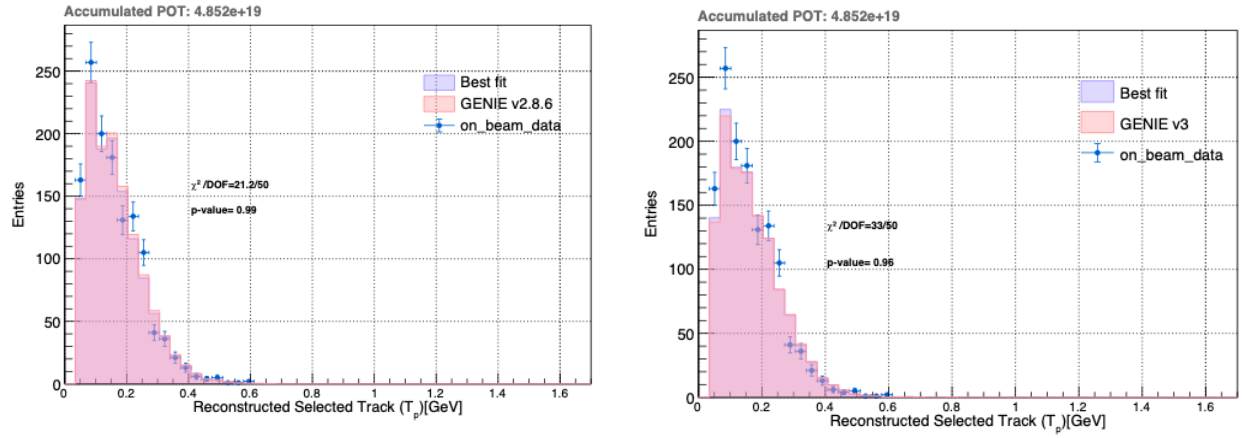

(a) (b)

Figure 9.5: Distributions of the proton kinetic energy T_p for simulated QE, RES, DIS, and MEC events plus off-beam as a result of projections to fitting result to on beam data (Blue), and GENIE default (Red)(a) Tune 1, and (b) Tune 3.

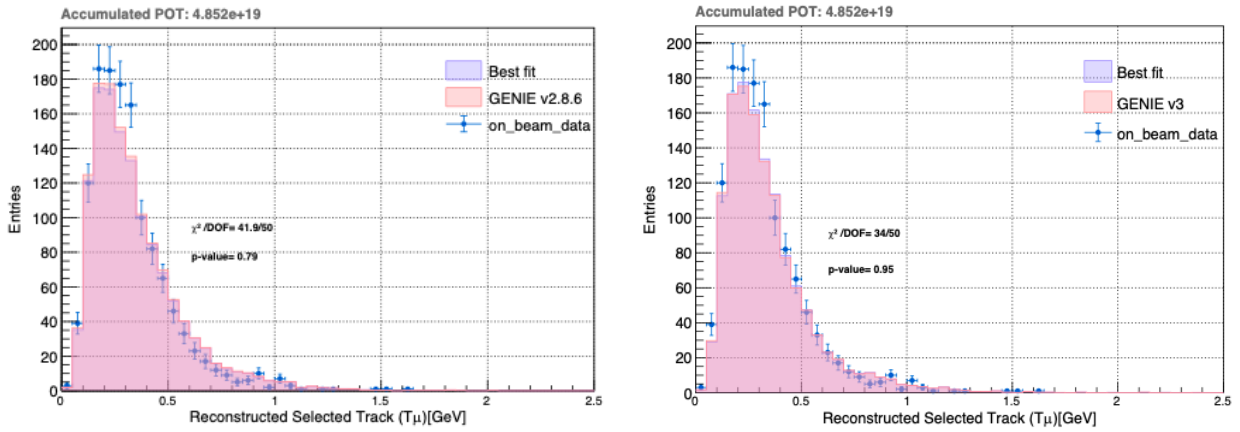

(a) (b)

Figure 9.6: Distributions of muon kinetic energy T_μ for simulated QE, RES, DIS, and MEC events plus off-beam as a result of projections to fitting result to on beam data (Blue), and GENIE default (Red)(a) Tune 1, and (b) Tune 3.

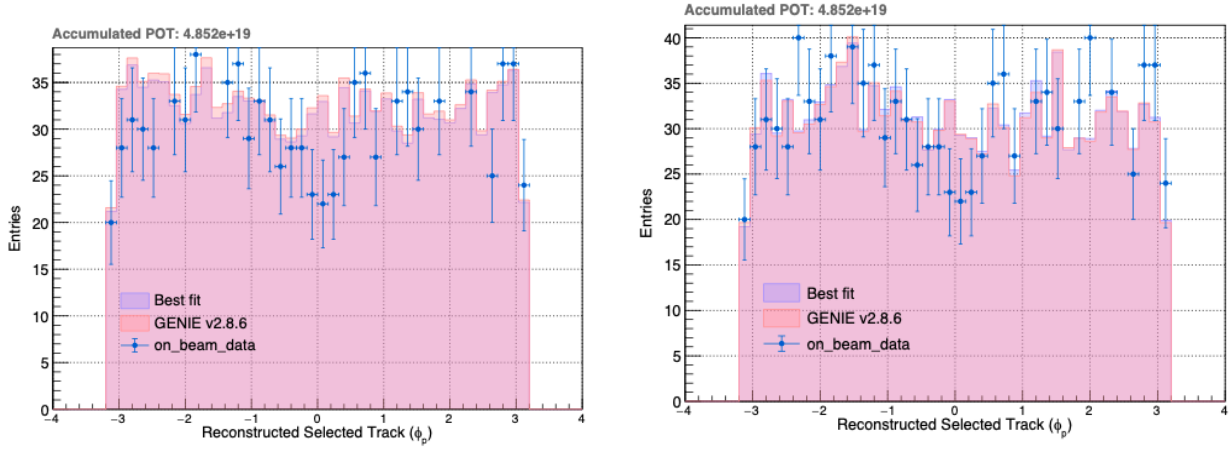

(a) (b)

Figure 9.7: Distributions of leading proton azimuthal angle ϕ_p for simulated QE, RES, DIS, and MEC events plus off-beam as a result of projections to fitting result to on beam data (Blue), and GENIE default (Red)(a) Tune 1, and (b) Tune 3.

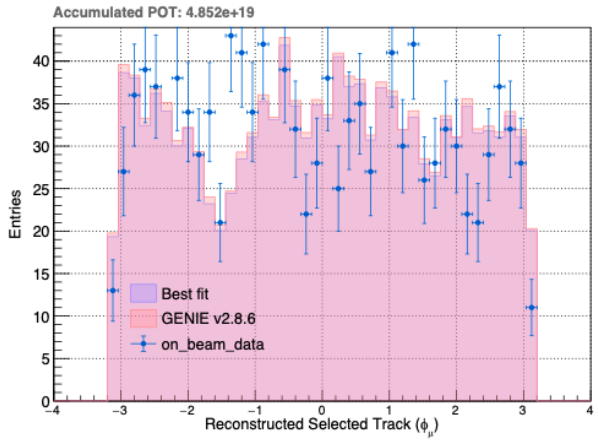

(a)

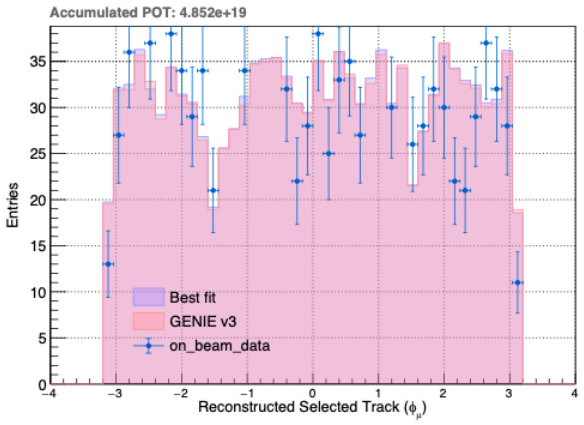

(b)

Figure 9.8: Distributions of muon azimuthal angle ϕ_μ for simulated QE, RES, DIS, and MEC events plus off-beam as a result of projections to fitting result to on beam data (Blue), and GENIE default (Red)(a) Tune 1, and (b) Tune 3

.

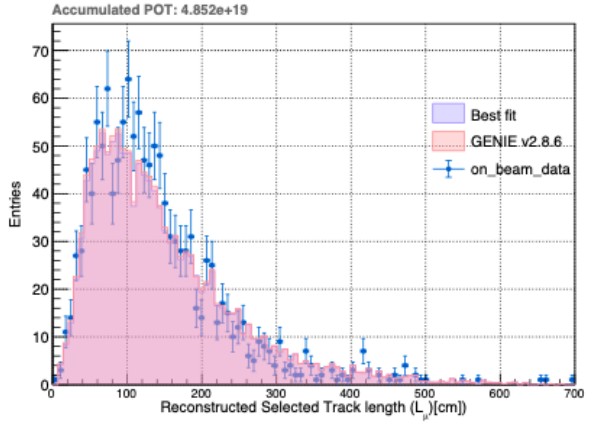

(a)

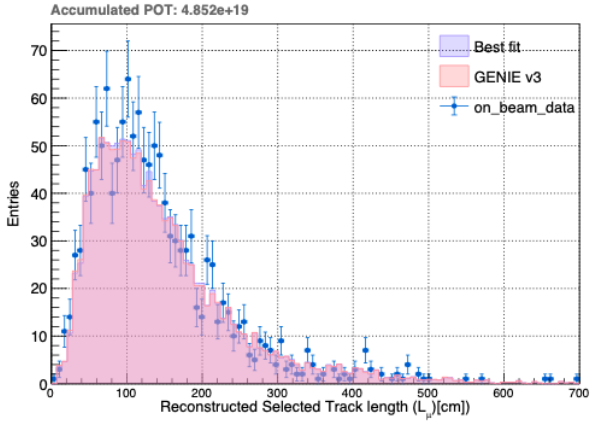

(b)

Figure 9.9: Distributions of muon length for simulated QE, RES, DIS, and MEC events plus off-beam as a result of projections to fitting result to on beam data (Blue), and GENIE default (Red)(a) Tune 1, and (b) Tune 3.

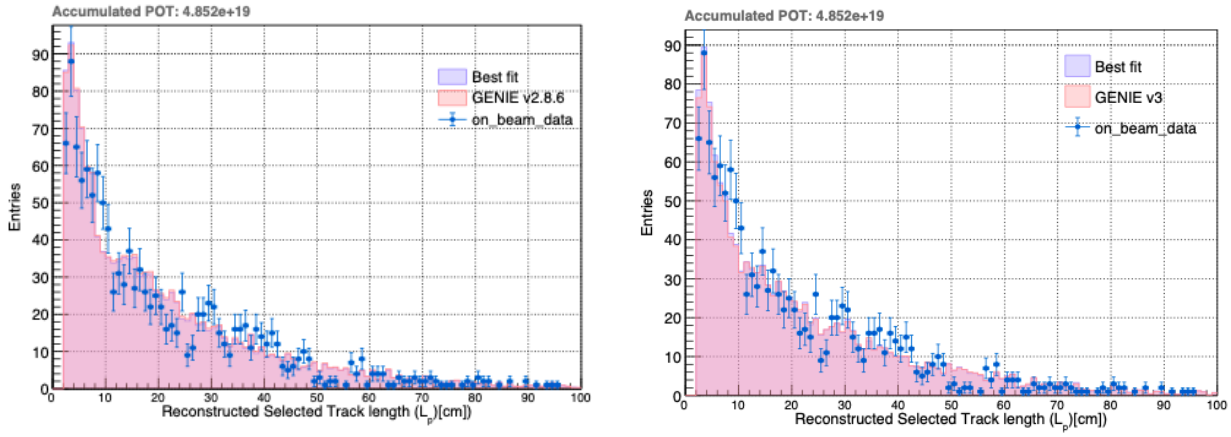

(a) (b)

Figure 9.10: Distributions of leading proton length for simulated QE, RES, DIS, and MEC events plus off-beam as a result of projections to fitting result to on beam data (Blue), and GENIE default (Red)(a) Tune 1, and (b) Tune 3.

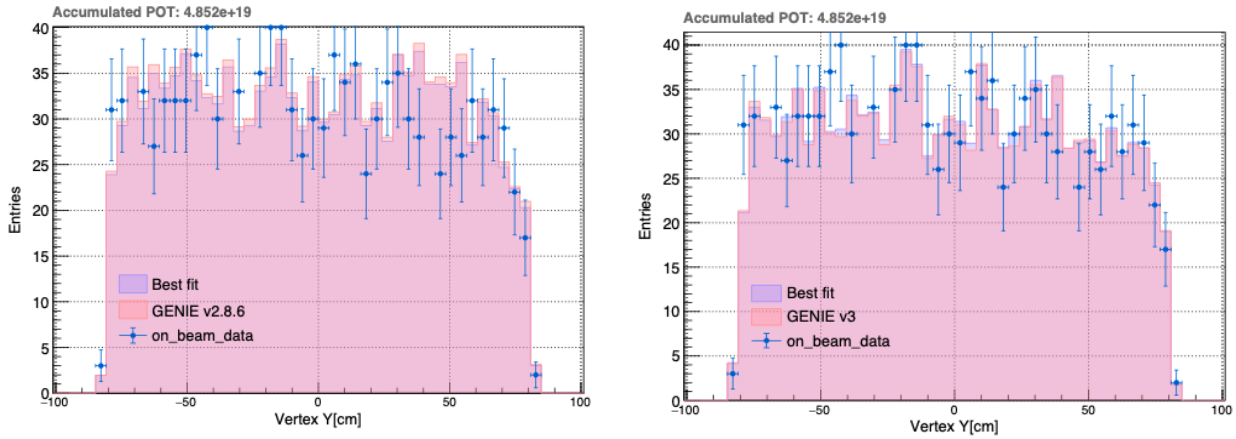

(a) (b)

Figure 9.11: Distributions of vertex in Y for simulated QE, RES, DIS, and MEC events plus off-beam as a result of projections to fitting result to on beam data (Blue), and GENIE default (Red)(a) Tune 1, and (b) Tune 3.

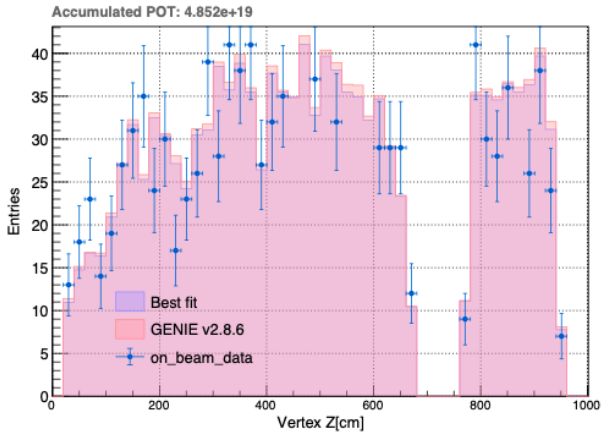

(a)

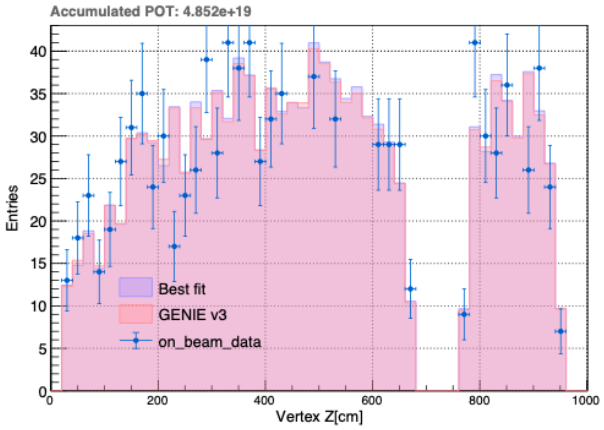

(b)

Figure 9.12: Distributions of vertex in Z for simulated QE, RES, DIS, and MEC events plus off-beam as a result of projections to fitting result to on beam data (Blue), and GENIE default (Red)(a) Tune 1, and (b) Tune 3.

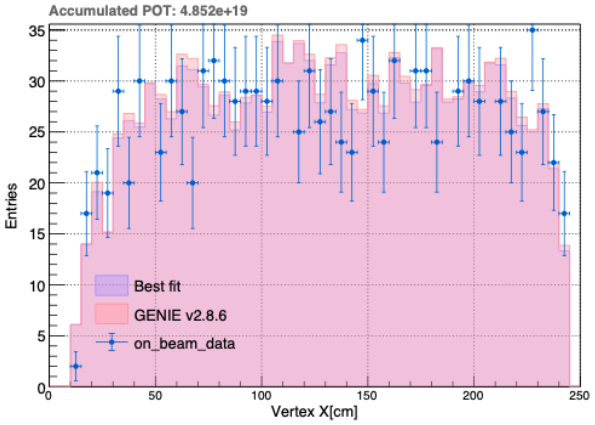

(a)

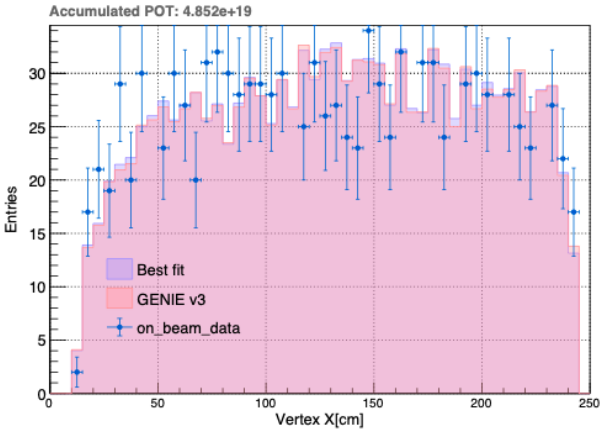

(b)

Figure 9.13: Distributions of vertex in X for simulated QE, RES, DIS, and MEC events plus off-beam as a result of projections to fitting result to on beam data (Blue), and GENIE default (Red)(a) Tune 1, and (b) Tune 3.

No tune describes all features of the data, even after readjusting the process fractions to the best-fit values. This statement must be tempered; however, by the presence of the large MCC8 systematics, which makes both tunes quantitatively consistent with the data within the errors.

9.3 Significance of each Process

After application of all systematic errors, the significance of each cross section contribution can be established, as discussed in Section 7.6.12. The significance χ^2 assume one degree of freedom of each of these processes ("QE", "RES", "DIS", and "MEC") contribution to the cross section are given in Table 9.5.

Table 9.5: The significance χ^2 assume one degree of freedom of each of these processes ("QE", "RES", "DIS", and "MEC") contribution to the cross section. " Default" and "adjusted " refer to the treatment of MCC8 errors.

Head	$\sqrt{\chi^2}$ default	$\sqrt{\chi^2}$ adjusted
QE/Total	6.0σ	7.5σ
Res/Total	3.6σ	4.0σ
DIS/Total	2.2σ	2.5σ
MEC/Total	6.1σ	7.3σ

The MEC contribution has 7.3 σ as shown in Table 9.5 taking into account statistical and systematic (including adjusted systematic errors related to the detector) errors. Thus, the cross section model requires a term to account for scattering from correlated nucleon pairs.

9.4 GENIE Comparisons

The significance of the χ^2 comparison between GENIE and date, discussed in Section 7.6.12, is 1.13 σ, which indicates consistency of GENIE with data.

9.5 Generating a Portable Result

The fitted event fractions apply to the sample of neutrino events that pass the cuts (CC-inclusive plus particle ID plus acolinearity) as described in section 7.4. In addition, the fractions apply to a particular cross section model. One can nonetheless provide these fractions in a way that would be useful to outside users. By replacing the actual experiment cuts are with this simple pair of requirements applied at truth level: $T_\mu > 100$ MeV, $T_p > 45$ MeV. This results in the truth-level fractions shown in Table 9.6, which are shown along with the truth-level event fractions for events passing the full set of cuts.

As one can see the event fractions are quite similar, which suggests that one can correct the measured fractions to a form that could be reproduced by the outside user that can run MicroBooNE GENIE MCC8 "tune 1" (v2.12.10 DefaultPlusMECWithNC, with "empirical MEC") and BNB flux file.

Table 9.6: Predicted Tune 1 GENIE (v2.12.10 DefaultPlusMECWithNC) fractions for events satisfying all selection criteria and for events satisfying simple 100 and 45 MeV truth level cuts on muon and proton kinetic energies, respectively.

Fraction	**full selection**	$\mathbf{T}_\mu > 100$ MeV, $\mathbf{T}_p > 45$ MeV
QE/Total	0.427	0.409
Res/Total	0.236	0.276
DIS/Total	0.06	0.074
MEC/Total	0.276	0.241

9.6 Conclusion

Using a sample of neutrino interactions with a muon and at least one proton present in the final state over full phase space leads to the following:

- The data support the picture that charged current scattering is dominated by a relatively small number of incoherent nucleon-level processes by testing the very foundational concept to GENIE: that the total cross section is dominated by a sum of incoherent sub-processes.

- Data can be satisfactorily described by two different GENIE v2 tunes, tune 1 and tune 3. Tunes 1 and 3 have very different QE and MEC fractions, although the sum of the two fractions is approximately the same. This is found to be true in data, where the MEC fraction under a tune 1 inerpretation is more than double that from a tune 3 interpretation. The process fractions are thus not universal at this stage of the theory development, but instead must be attached to a different version of the generator. Complicating the story further, one can only base the tune 3 discussions on the preliminary MCC8 version.

- A "MEC" contribution appears with high significance, (7.3 σ) taken into account statistical and systematic errors. This corporate quantitatively the need for multinucleon to the cross section in the BNB for less than 2 GeV energy range.

- One observes a possible discrepancy between GENIE and the data, which indication of a low contribution comes from the resonance cross section. However, when taken into account systematic, GENIE is consistent with data.

Bibliography

[1] C. Andreopoulos *et al.*, "The GENIE Neutrino Monte Carlo Generator: Physics and User Manual," (2015), arXiv:1510.05494.

[2] B. Abi et al. (DUNE Collaboration), "The DUNE far detector interim design report, Volume 1: Physics, technology and strategies," (2018), arXiv:1807.10334.

[3] B. Abi et al. (DUNE Collaboration), "The DUNE far detector interim design report, Volume 2: Single-phase module," (2018), arXiv:1807.10327.

[4] B. Abi et al. (DUNE Collaboration), "The DUNE far detector interim design report, Volume 3: Dual-phase module," (2018), arXiv:1807.10340.

[5] K. Abe *et al.* (HyperKamiokande Proto-Collaboration), "Hyper-Kamiokande Design Report," (2018), arXiv:1805.04163.

[6] M. Antonello et al. (LAr1-ND, ICARUS-WA104, MicroBooNE Collaborations), "A proposal for a three detector short-baseline neutrino oscillation program in the Fermilab Booster neutrino beam," (2015), arXiv:1503.01520.

[7] T. Golan, J. Sobczyk, and J. Zmuda, Nuclear Physics B, Proceedings Supplements 229-232, 499 (2012).

[8] O. Buss et al., Physics Reports 512, 1 (2012).

[9] E. Fermi, Z. Physik 88 161 (1934).

[10] M. et al. Tanabashi. Review of particle physics. Phys. Rev. D, 98:030001, Aug 2018.

[11] "Looking at Physics History." American Physical Society, https://www.aps.org/publications/capitolhillquarterly/20

[12] Bilenky-S. M. , "Neutrino. History Of a Unique Particle, "(2015) arxiv:1210.3065.

[13] Lipari, Paolo, "INTRODUCTION TO NEUTRINO PHYSICS - CERN," . https://cds.cern.ch/record/677618/files/p115.pdf.

[14] Zralek, "Are Neutrinos Dirac or Majorana Particles?," ArXiv.org, 28 Oct. 1999, https://arxiv.org/abs/hep-ph/9910357.

[15] Super-Kamiokande Collaboration, "Evidence for Oscillation of Atmospheric Neutrinos," Phys. Rev. Lett. 81 (1998), 1562.

[16] SNO Collaboration, "Measurement of the Rate of ν_e d$\rightarrow pp\, e^-$ Interactions Produced by 8B Solar Neutrinos at the Sudbury Neutrino Observatory," Phys. Rev. Lett. 87 (2001), 071301.

[17] SNO Collaboration, "Direct Evidence for Neutrino Flavor Transformation from Neutral-Current Interactions in the Sudbury Neutrino Observatory," Phys. Rev. Lett. 89 (2002), 011301.

[18] B. Pontecorvo, Sov. Phys. JETP 6 429 (1957).

[19] The MicroBooNE Collaboration "First muon-neutrino charged-currents, inclusive differential cross section measurement for microboone run 1 data," MICROBOONE-NOTE-1045-PUB.

[20] The MicroBooNE Collaboration "Design and Construction of the MicroBooNE Detector," JINST 12, no. 02, P02017 (2017) doi:10.1088/1748-0221/12/02/P02017 [arXiv:1612.05824 [physics.ins-det]].

[21] D. Heck *et al.*, "CORSIKA: A Monte Carlo code to simulate extensive air showers," JINST 12, no. 02, P02017 (2017) doi:10.1088/1748-0221/12/02/P02017 [arXiv:1612.05824 [physics.ins-det]].

[22] R. Brun *et al.*, "GEANT Detector Description and Simulation Tool," doi:10.17181/CERN.MUHF.DMJ1

[23] E. D. Church, "LArSoft: A Software Package for Liquid Argon Time Projection Drift Chambers," arXiv:1311.6774 [physics.ins-det].

[24] MiniBooNE Collaboration "Unexplained Excess of Electron674 Like Events From a 1-GeV Neutrino Beam," arXiv:1311.6774 [physics.ins-det].

[25] Teppei Katori, and Janet M. Conrad "Beyond standard model searches in the MiniBooNE experiment," arXiv:1404.7759

[26] MiniBooNE Collaboration "Noise Characterization and Filtering in the MicroBooNE Liquid Argon TPC," JINST 12, no. 08, P08003 (2017) doi:10.1088/1748- 0221/12/08/P08003 [arXiv:1705.07341 [physics.ins-det]].

[27] J. S. Marshall and M. A. Thomson, "The Pandora Software Development Kit for Pattern Recognition, " Eur. Phys. J. C 75, no. 9, 439 (2015) doi:10.1140/epjc/s10052015-3659-3 [arXiv:1506.05348 [physics.data-an]].

[28] MicroBooNE Collaboration "The Pandora multi-algorithm approach to automated pattern recognition of cosmic-ray muon and neutrino events in the MicroBooNE detector, " [arXiv:1708.03135 [physics.hep-ex]], accepted by Eur. Phys. J. C.

[29] MicroBooNE Collaboration "Cosmic Shielding Studies at MicroBooNE," MICROBOONE-NOTE-1005-PUB.

[30] MicroBooNE Collaboration "Measurement of cosmic-ray reconstruction efficiencies in the MicroBooNE LArTPC using a small external cosmic-ray counter," JINST 12, no. 12, P12030 (2017) doi:10.1088/1748-0221/12/12/P12030 [arXiv:1707.09903 [hep-ex]].

[31] The MicroBooNE Collaboration "Selection of numu charged–current induced interactions with $N > 0$ protons and performance of events with $N = 2$ protons in the final state in the MicroBooNE detector from the BNB," MICROBOONE-NOTE-1056-PUB.

[32] The MicroBooNE Collaboration "Selection of numu Events for the MicroBooNE Deep Learning Low Energy Excess Analysis," MICROBOONE-NOTE-1051-PUB.

[33] The MiniBooNE Collaboration "Neutrino flux prediction at MiniBooNE," In: Phys. Rev. D.79 (2009), p. 072002.

[34] R. Carr, L. Yates, and J. Zennamo, "Tech Note: Detector Systematics Samples Available in Summer 2018," MicroBooNE Document 16028-v3.

[35] Yichen Li *et al.* "Measurement of Longitudinal Electron Diffusion in Liquid Argon," Nucl. Instrum. Meth. A816 (2016),160-170, arXiv:1508.07059.

[36] M. Del Tutto, "Deeper Look at the Detector Variations for the NuMu CC Inclusive Analysis," MicroBooNE Document 14940-v2.

[37] A. Aguilar-Arevalo, B. Brown, L. Bugel, G. Cheng, E. Church, J. Conrad, R. Dharma- palan, Z. Djurcic, D. Finley, R. Ford, et al., Physical Review Letters 110, 161801 (2013).

[38] F. Halzen and A. D. Martin. Quarks And Leptons: Introductory Course in Modern Particle Physics. Wiley, 1984.

[39] C. H. Llewellyn Smith, "Neutrino Reactions at Accelerator Energies, " Phys. Rept., vol. 3, pp. 261–379, 1972. doi: 10.1016/0370-1573(72)90010-5.

[40] R. A. Smith and E. J. Moniz, "Neutrino Reactions on Nuclear Targets, " Nucl. Phys., vol. B43, p. 605, 1972, [Erratum: Nucl. Phys.B101,547(1975)]. doi: 10.1016/0550-3213(75)90612-4,10.1016/0550-3213(72)90040-5.

[41] D. Rein and L. M. Sehgal, "Neutrino Excitation of Baryon Resonances and Single Pion Production," Annals Phys., vol. 133, pp. 79–153, 1981. doi: 10.1016/0003-4916(81)90242-6.

[42] A. Bodek, H. S. Budd, and M. E. Christy, "Neutrino Quasielastic Scattering on Nuclear Targets: Parametrizing Transverse Enhancement (Meson Exchange Currents)," Eur. Phys. J., vol. C71, p. 1726, 2011. doi: 10.1140/epjc/s10052-011-1726-y. arXiv: 1106.0340 [hep-ph].

[43] U. K. Yang and A. Bodek, "Parton distributions, and higher twist effects at high x," Phys. Rev. Lett., vol. 82, pp. 2467-2470, 1999. doi: 10.1103/ PhysRevLett.82.2467. arXiv: hep-ph/9809480 [hep-ph].

[44] T. Katori, AIP Conf. Proc. 1663, 030001 (2015).

[45] A. A. Aguilar-Arevalo *et al.*, "Neutrino flux prediction at MiniBooNE," In: Phys. Rev. D 79 (7 Apr. 2009), p. 072002. doi: 10.1103/PhysRevD.79.072002. url: https://link.aps.org/doi/10.1103/PhysRevD.79.072002.

[46] The MicroBooNE Collaboration, "Booster Neutrino Flux Prediction at MicroBooNE," MICROBOONE-NOTE- 1031-PUB.

[47] M.Tuops, "First Results from MicroBooNE," MicroBooNE Document

[48] The MicroBooNE Collaboration, "Noise Characterization and Filtering in the MicroBooNE Liquid Argon TPC," In: Journal of Instrumentation 12.08 (Aug. 2017), P08003–P08003. doi: 10.1088/1748-0221/12/08/p08003. url: https://doi.org/10.1088

[49] B. C. Brown, P. Adamson, D. Capista, W. Chou, I. Kourbanis, D. K. Morris, K. Seiya, G. H. Wu, and M.-J. Yang, Physical Review Special Topics-Accelerators and Beams 16, 071001 (2013).

[50] J. A. Formaggio and G. P. Zeller, "From eV to EeV: Neutrino cross sections across energy scales," In: Rev. Mod. Phys. 84 (3 Sept. 2012), pp. 1307–1341. doi: 10.1103/RevModPhys. 84.1307. url: https://link.aps.org/doi/10.1103/RevModPhys.84.1307.

[51] The MicroBooNE Collaboration, "MicroBooNE low-energy excess signal prediction from unfolding MiniBooNE Monte-Carlo and data," MICROBOONE-NOTE-1043-PUB.

[52] The ArgoNeuT Collaboration, "Demonstration of MeV-Scale Physics in Liquid Argon Time Projection Chambers Using ArgoNeuT," https://arxiv.org/pdf/1810.06502.pdf

[53] R. Carr, L. Yates, and J. Zennamo, "Tech Note: Detector Systematics Samples Available in Summer 2018", MicroBooNE Document 16028-v3.

[54] Yichen Li *et al.* "Measurement of Longitudinal Electron Diffusion in Liquid Argon," Nucl. Instrum. Meth. A816 (2016),160-170, arXiv:1508.07059.

[55] A. Ashkenazi, S. Gardiner, A. Mastbaum, A. Papadopoulou, "Neutrino Interactions Modeling Note", MicroBooNE DocDB 20554-v4.

[56] B. P. Roe, Nucl. Instrum. Meth. 570, 159 (2007).

[57] Libo Jiang, Nicholas Suarez, Steve Dytman, and Andy Furmanski "Charged Current one Muon and N Proton(N$\geq$ 1) Selection and 2 Kinematic Properties Analysis in MicroBooNE " , MicroBooNE DocDB 15426.

[58] M.Alrashed, T.Bolton, G.Song, "Initial Phase Space Analysis of Inclusive CC Proton Production," MicroBooNE Document 17797-v2.

[59] The MicroBooNE Collaboration, "Study of Space Charge Effects in MicroBooNE," MICROBOONE-NOTE-1018-PUB.

[60] Xiao Luo, "Neutrino interactions in MicroBooNE," MicroBooNE Document 6205-v3.

[61] X.-G. Lu, L. Pickering, S. Dolan, G. Barr, D. Coplowe, Y. Uchida, D. Wark, M. O. Wascko, A. Weber, and T. Yuan, "Measurement of nuclear effects in neutrino interactions with minimal dependence on neutrino energy," Phys. Rev. C, 94:015503, Jul 2016.

[62] Super-Kamiokande Collaboration, "A Measurement of atmospheric neutrino oscillation parameters by SUPER-KAMIOKANDE," Phys.Rev. D71 (2005) 112005, arXiv:hep-ex/0501064.

[63] KamLAND Collaboration, "Measurement of neutrino oscillation with KamLAND: Evidence of spectral distortion," Phys.Rev.Lett. 94 (2005) 081801, arXiv:hep-ex/0406035.

[64] T2K Collaboration, "Indication of Electron Neutrino Appearance from an Accelerator-produced Off-axis Muon Neutrino Beam," Phys.Rev.Lett. 107 (2011) 041801, arXiv:1106.2822 [hep-ex].

Appendix A

Further Cross-Check

This appendix applied further cross check.

A.1 Difference between Corsika and EXT cosmics

The underlying issue here is whether the template of CR events that overlap neutrino events have the same templates as the off-beam CR events. Therefore, selecting BNB+Corsika events where the RECO vertex is very different from the neutrino vertex. These are presumably CR events. One observes that the difference between the RECO vertex and the neutrino vertex is very small as shown in Fig. A.1 within this model. Figure A.3 shows the distribution of the difference between the RECO vertex and the neutrino vertex in each of the nucleon level processes. The CR events that overlap neutrino events is estimated from the tail of the difference between the RECO vertex and the neutrino vertex distribution as shown in Fig. A.2. Then, the template for these CR events that overlap neutrino events is created and is denoted "X_{CR}^{MC}" as shown in Fig. A.4, which is consistent with the off-beam CR events template "X_{CR}" as shown in Fig. 7.8. Then, adding the corresponding term is to the fit. As a result, the fraction of Corsika events are very small (0.0146), so there are not many of these events. Table A.1 summarized this study. All CR is well modeled by off-beam data. The requirement of two fully contained tracks with particle ID requirements strongly suppresses CR, and the acolinearity requirement knocks it down even more.

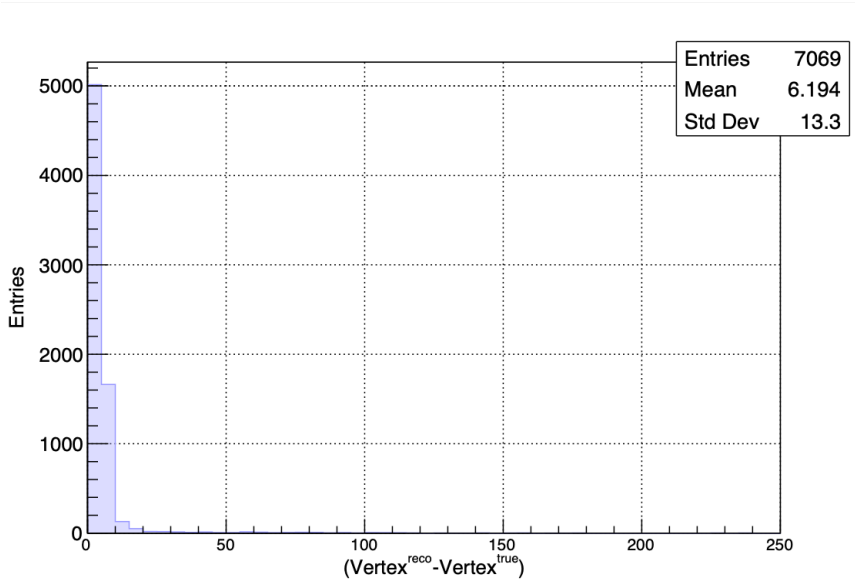

(a)

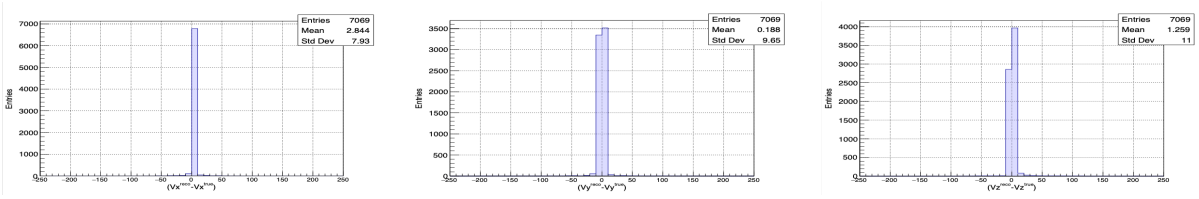

(b) (c) (d)

Figure A.1: Distribution of (a) the difference between the RECO vertex and the neutrino vertex, in (b)ΔV_x, (c) ΔV_y, and (d) ΔV_z.

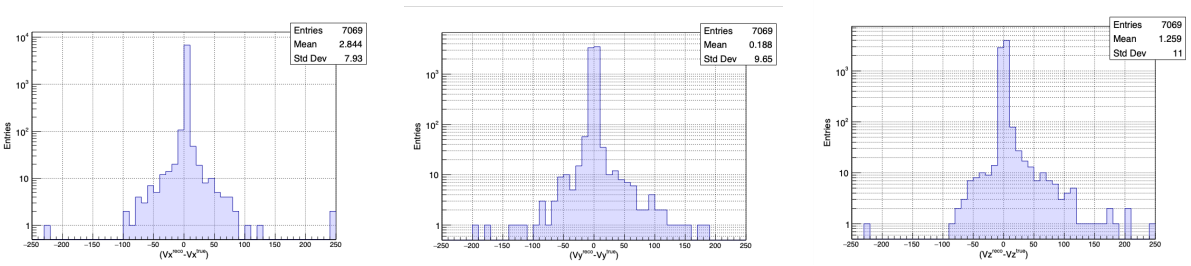

(a) (b) (c)

Figure A.2: Distribution of the difference between the RECO vertex and the neutrino vertex, in is in logarithmic scale for(a)ΔV_x, (b) ΔV_y, and (c) ΔV_z.

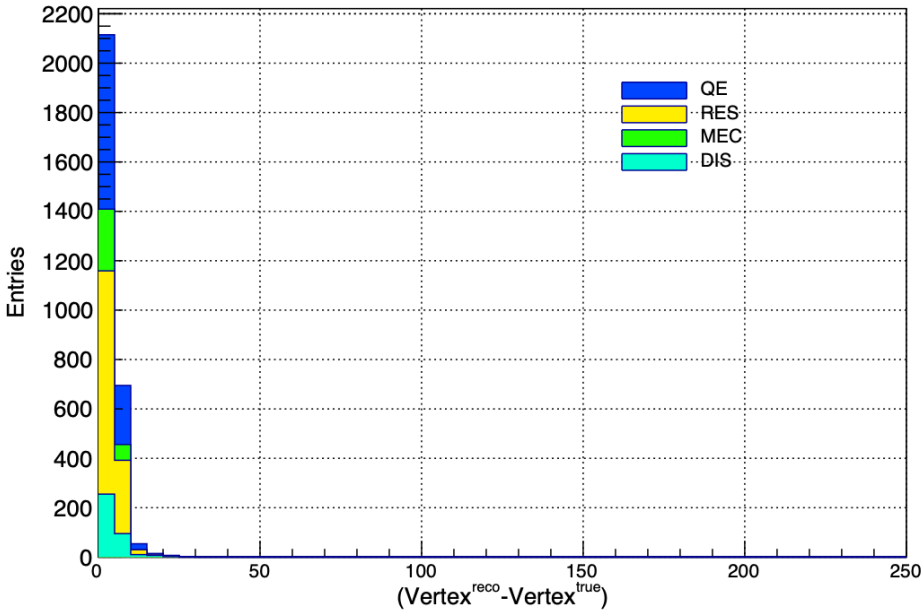

Figure A.3: Distribution of the difference between the RECO vertex and the neutrino vertex of simulated QE, RES, DIS, and MEC events.

Table A.1: The results of fitting the production model of simulated QE, RES, DIS, and MEC events plus off-beam data and CR from MC to on-beam data.

Head	Output	
QE/Total	0.433	±0.025
Res/Total	0.176	±0.024
DIS/Total	0.052	±0.015
MEC/Total	0.255	±0.026
Cosmic/Total	0.054	±0.009
CR^{MC}/Total	0.0146	±0.010
$\mathcal{L}$	649.05	
χ^2	1298	
Non-zero bins	956	

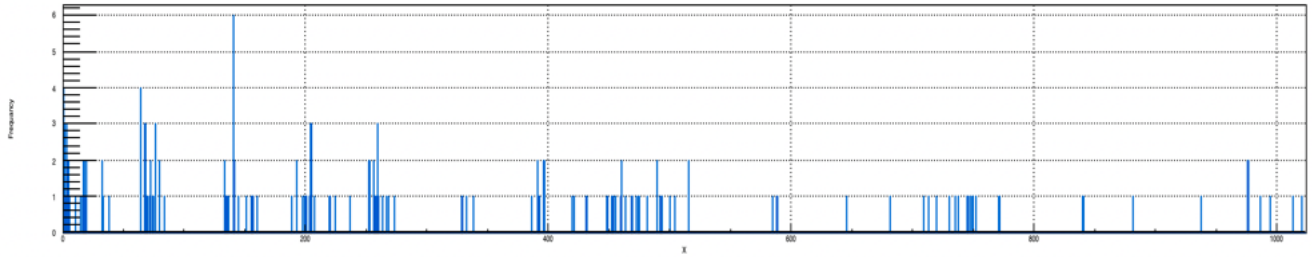

Figure A.4: The index histogram for "CR", "X_{CR}^{MC}".

A.2 The relative efficiencies of each topology type

If either the muon or proton has $\phi = 0$ or π, the companion object will also be in a relatively poor acceptance region for the QE topology. On the other hand, for QE events, if one track is good, then the other will be too. For other topologies, one good track could still leave the other in the bad region. Hence there is some compensation, even if the bad region results in complete loss of a track (which it does not– the bad efficiency region is more accurately ϕ near 0 or π when $\cos\theta$ is near 0). To see this schematically, define ϵ_B as the relative efficiency for a track in the bad region compared to one in the good region, f as the fraction of muon tracks in the bad region, and g_X the fraction of events where the proton is in the bad region when the muon is not for process $X \neq QE$. Then, the process efficiencies are, schematically:

$$\epsilon_{QE} = f\epsilon_B^2 + (1-f)\,, \tag{A.1}$$

$$\epsilon_X = f\epsilon_B + (1-f)\,g_X\epsilon_B + (1-f)\,(1-g_X)\,, \tag{A.2}$$

for a wide range of ϵ_B, f, and g_X, the efficiencies ϵ_{QE} and ϵ_X are within 10% of each other, or less. A systematic error is then the uncertainty in the MC modelling of this efficiency difference. Figure A.5 shows the distributions of (left) the muon azimuthal angle ϕ_μ and (right) the leading proton azimuthal angle ϕ_p for simulated QE, RES, DIS, and MEC events plus off-beam as a result of projections to fitting result to on beam data after applying the cut on ϕ_μ near $\phi_\mu = 0$ or π. Figure A.6 shows the distributions of the difference in the muon azimuthal angle and the leading proton azimuthal angle $\Delta\phi_{\mu p}$ for simulated QE, RES, DIS, and MEC events plus off-beam as a result of projections to fitting result to on beam data with the cut on ϕ_μ. Table A.2 shows the results of fitting the production model of simulated QE, RES, DIS, and MEC events plus off-beam data to on-beam data with the cut on ϕ_μ near $\phi_\mu = 0$ or π, which indicates a tiny shift the relative fraction of each nucleon level process model. All of these cross section templates are distinguishable even after applying this cut as shown in Table A.3. Note the number of degrees of freedom is taken to be the number of bins that have at least one entry.

Table A.2: The results of fitting the production model of simulated QE, RES, DIS, and MEC events plus off-beam data to on-beam data with the cut on φ_μ near $\phi_\mu = 0$ or π.

Head	Output	
QE/Total	0.44	± 0.029
Res/Total	0.16	± 0.024
DIS/Total	0.062	± 0.015
MEC/Total	0.21	± 0.026
Cosmic/Total	0.082	± 0.009
$\mathcal{L}$	718.843	
χ^2	1437.68	
Non-zero bins	903	

Table A.3: χ^2 distance test shows these templates are distinguishable, and p-value with cut in φ_μ

Head	χ^2 Distance	ndf	p-value
"QE-RES"	1343.88	766	2.8×10^{-34}
"QE-DIS"	1027.24	642	2.7×10^{-20}
"QE-MEC"	1461.29	781	7.7×10^{-44}
"RES-MEC"	777.858	693	0.14×10^{-1}
"RES-DIS"	558.603	559	0.5
"MEC-DIS"	693.183	596	0.4×10^{-2}

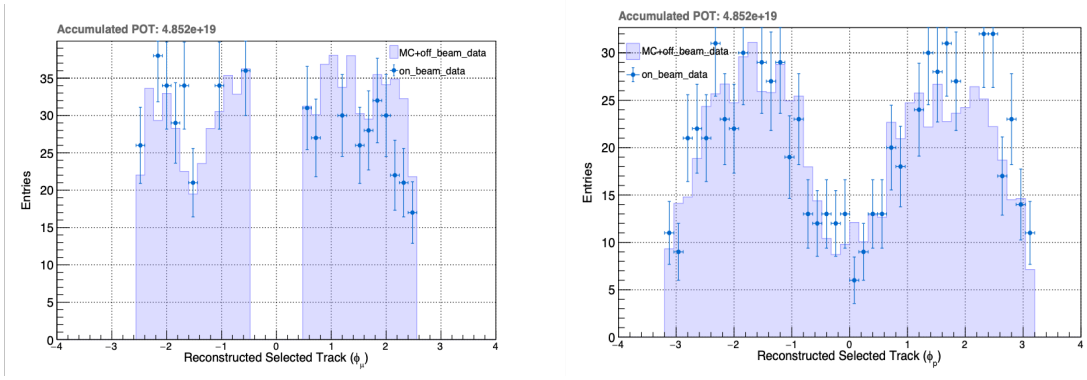

(a) (b)

Figure A.5: Distributions of: (a)the muon azimuthal angle ϕ_μ and (b) the leading proton azimuthal angle ϕ_p for simulated QE, RES, DIS, and MEC events plus off-beam as a result of projections to fitting the result to on beam data with the cut on ϕ_μ in Tune 1.

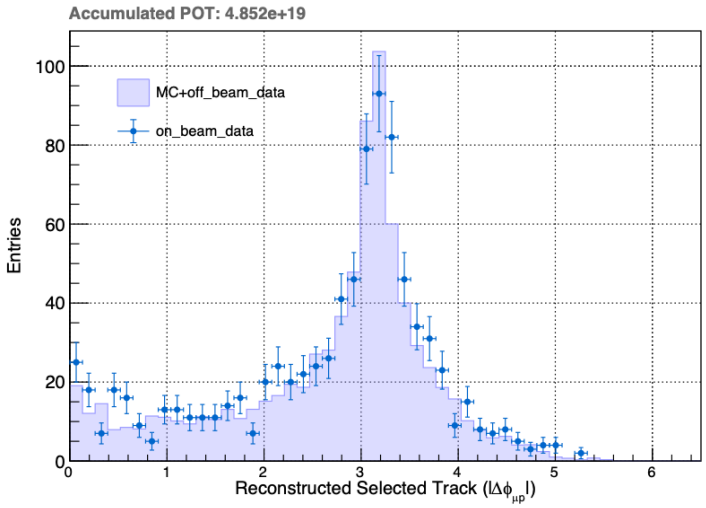

Figure A.6: Distributions of the difference in the muon azimuthal angle and the leading proton azimuthal angle $\Delta\phi_{\mu p}$ for simulated QE, RES, DIS, and MEC events plus off-beam as a result of projections to fitting the result to on beam data with the cut on ϕ_μ in Tune 1.

Furthermore, the azimuthal variable is the difference $\phi_\mu - \phi_p$, and so the $\phi = 0, \pi$ features are averaged over. The individual ϕ_μ, ϕ_p are shown in Fig. 9.8 - 9.7 . The acceptance features are there. The inclusive CC analysis has bad agreement with the model, roughly speaking, at high T_μ and high $\cos\theta_\mu$. In these templates, these are a little hard to pick out. However, Tables A.4 , A.5, A.6, and A.7 summarized the results of fitting the production model of simulated QE, RES, DIS, and MEC events plus off-beam data to on-beam data for each quartile of the full index histogram with 256 bins each as shown in Fig. 7.13 -A.7. High T_μ are in bins $768 - 1023$ (the "bottom plot" when the template is split into four histograms with 256 bins each). If this block is broken up into 16 groups of 16 bins, then the high $\cos\theta_\mu$ events are the rightmost four bins in each of these groups.

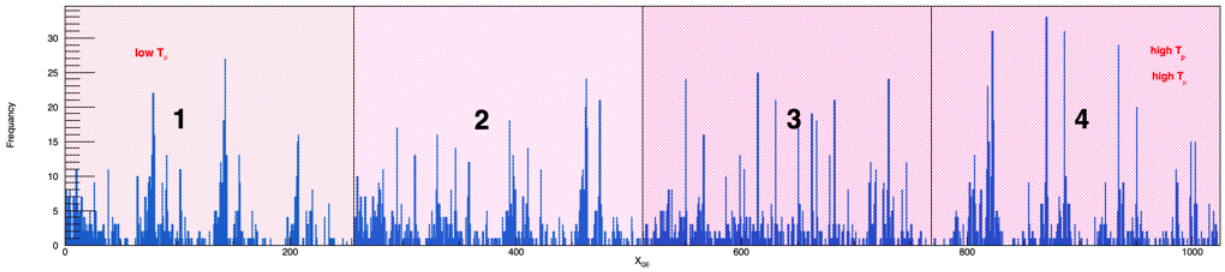

Figure A.7: The index histogram for simulated (a) QE events "X_{QE}".

Table A.4: The results of fitting the production model of simulated QE, RES, DIS, and MEC events plus off-beam data to on-beam data for 1^{st} quarter from index histogram $[0 - 256)$.

Head	Output	
QE/Total	0.41	±0.048
Res/Total	0.25	±0.058
DIS/Total	0.05	±0.036
MEC/Total	0.20	±0.054
Cosmic/Total	0.08	±0.024
$\mathcal{L}$	86.02	
χ^2	172.04	
Non-zero bins	237	

Table A.5: The results of fitting the production model of simulated QE, RES, DIS, and MEC events plus off-beam data to on-beam data for 2^{nd} quarter from index histogram $[256 - 512)$.

Head	Output	
QE/Total	0.49	±0.049
Res/Total	0.16	±0.038
DIS/Total	0.05	±0.026
MEC/Total	0.22	±0.046
Cosmic/Total	0.06	±0.019
$\mathcal{L}$	169.45	
χ^2	338.91	
Non-zero bins	252	

Table A.6: The results of fitting the production model of simulated QE, RES, DIS, and MEC events plus off-beam data to on-beam data for 3^{rd} quarter from index histogram $[512 - 768)$.

Head	Output	
QE/Total	0.43	±0.048
Res/Total	0.16	±0.044
DIS/Total	0.04	±0.028
MEC/Total	0.31	±0.048
Cosmic/Total	0.04	±0.013
$\mathcal{L}$	233.75	
χ^2	467.49	
Non-zero bins	249	

Table A.7: The results of fitting the production model of simulated QE, RES, DIS, and MEC events plus off-beam data to on-beam data for 4^{th} quarter from index histogram $[768 - 1024)$.

Head	Output	
QE/Total	0.40	±0.056
Res/Total	0.13	±0.057
DIS/Total	0.07	±0.028
MEC/Total	0.35	±0.069
Cosmic/Total	0.007	±0.008
$\mathcal{L}$	146.922	
χ^2	293.844	
Non-zero bins	218	

Appendix B

Further Details of Fitting Procedure

B.1 Fitting Strategies in Details

1. Characterizing the $\mu-$ p final state completely by five kinematic variables (T_μ, T_p , $\cos\theta\mu$, $\cos\theta p$, $\Delta\varphi_{\mu p}$). Figure B.1 shows the most common distribution in MicroBooNE of the kinematic variables for the selected reconstructed track (using the CC inclusive selection as described in [19]), using the particle ID recommendation for the separation of muons and protons as described in [31]. Briefly, considering muon with χ^2 score is greater than 88, while proton with χ^2 score is less than 88.

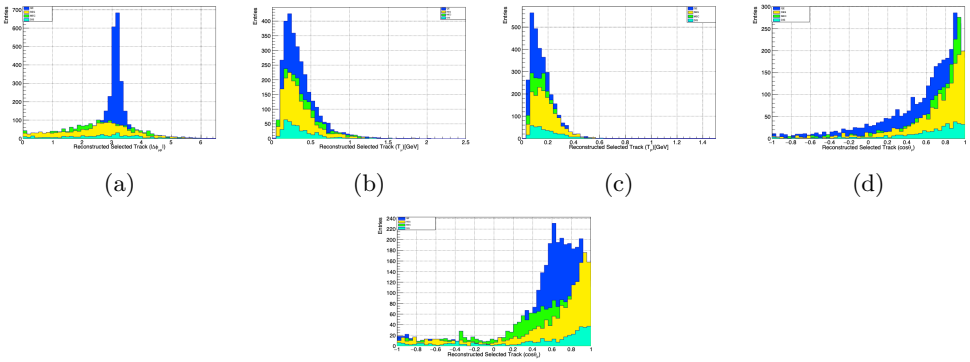

(a) (b) (c) (d)

(e)

Figure B.1: Distributions of: (a) the difference in the muon azimuthal angle and the leading proton azimuthal angle, (b) the muon kinetic energy, (c) the leading proton kinetic energy, (d) $\cos\theta_\mu$, and (e) $\cos\theta_p$ for selected reconstructed track.

2. Applying Two Maps

   (a) The first map is taking the continuous variables to the integer bin numbers. To illustrate that, taking the continuous variables (T_μ, T_p , $\cos\theta_\mu$, $\cos\theta_p$, $\Delta\varphi_{\mu p}$) to the integer bin numbers (iT_μ,iT_p , $i\cos\theta_\mu$, $i\cos\theta_p$, $i\Delta\varphi_{\mu p}$) by setting the bin boundaries as shown in the Table B.1,

each bin has the same number of events. Figure B.6 shows successfully defining bins to equally partition a nominal model.

For the first bin

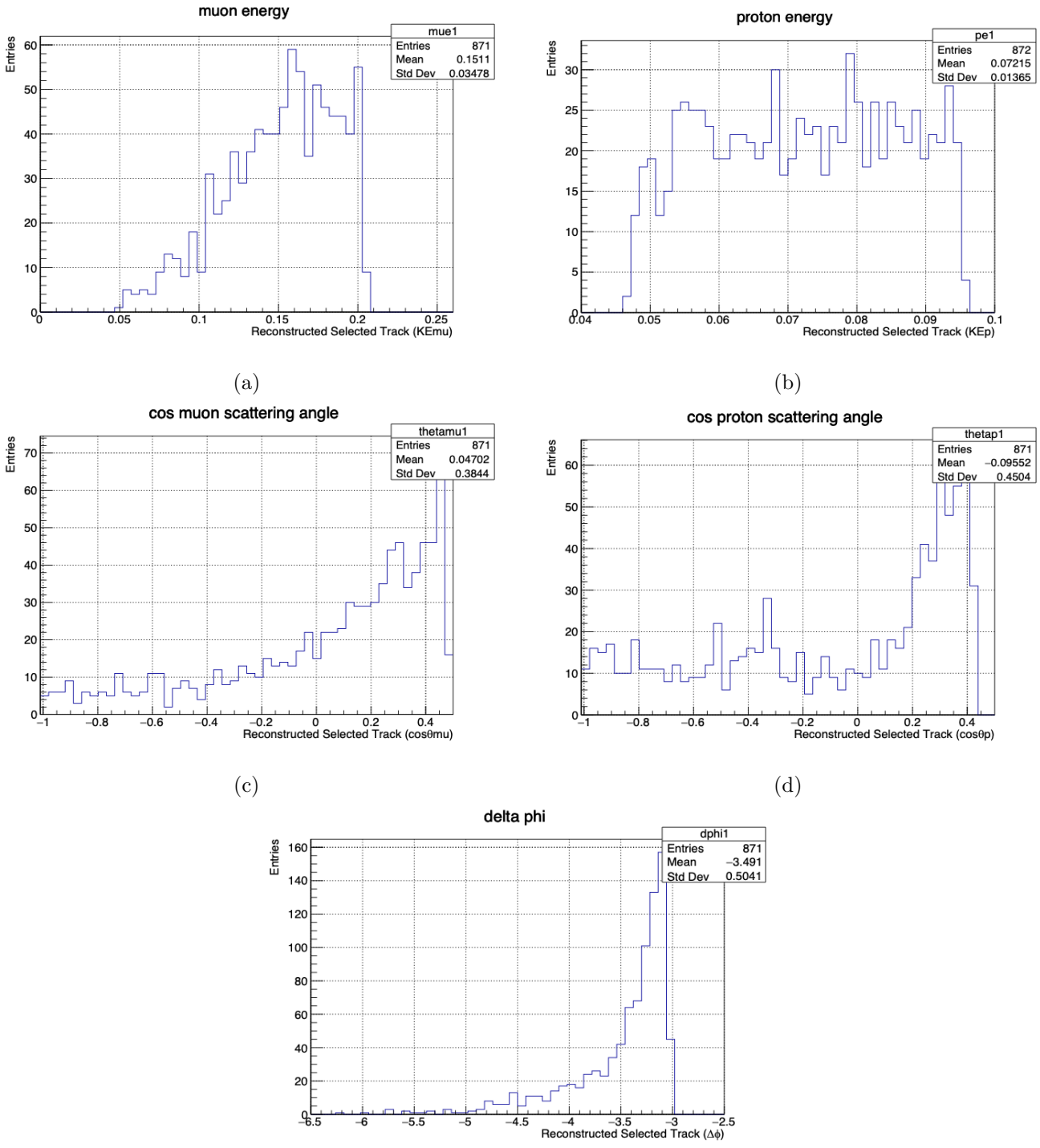

Figure B.2: Distributions of: (a) the muon kinetic energy, (b) the leading proton kinetic energy, (c) $\cos\theta_\mu$, (d) $\cos\theta_p$, and (e) the difference in the muon azimuthal angle and the leading proton azimuthal angle for selected reconstructed track for the first bin.

For the second bin

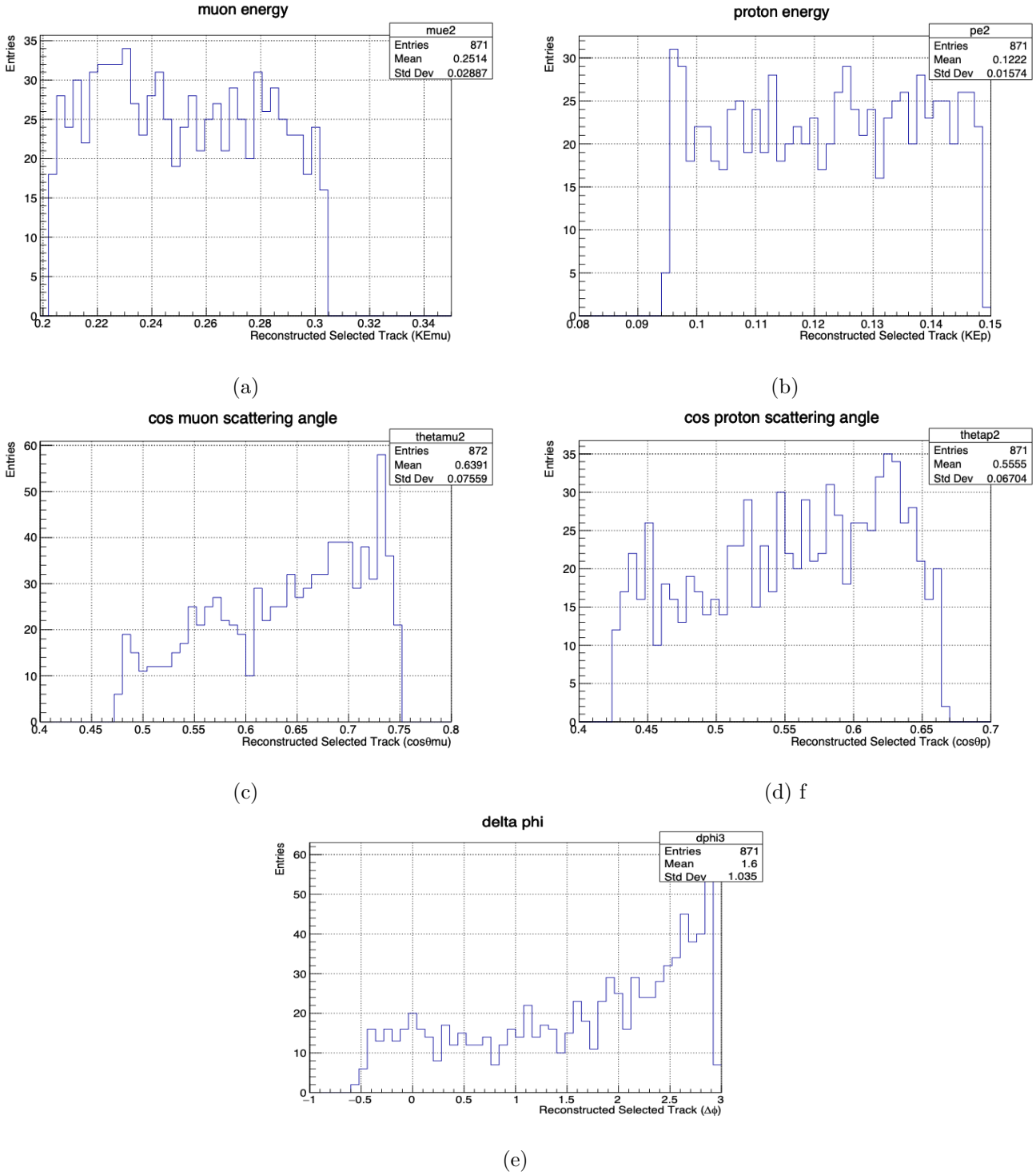

Figure B.3: Distributions of: (a) the muon kinetic energy, (b) the leading proton kinetic energy, (c) $\cos\theta_\mu$, (d) $\cos\theta_p$, and (e) the difference in the muon azimuthal angle and the leading proton azimuthal angle for selceted reconstructed track for the second bin.

For the third bin

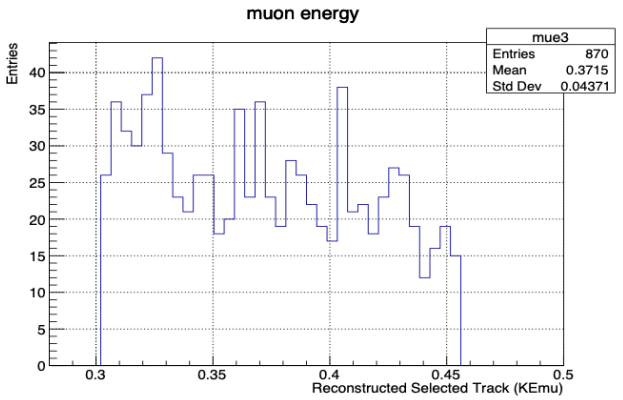

(a)

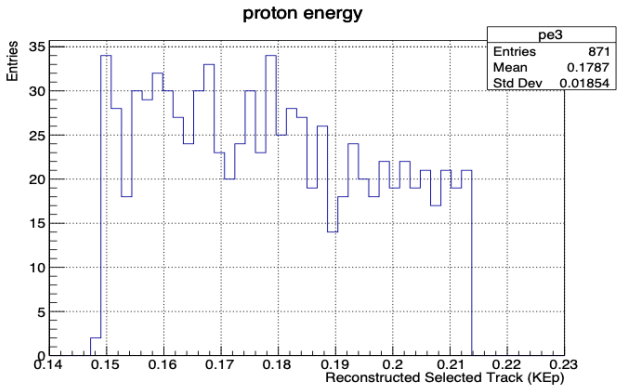

(b)

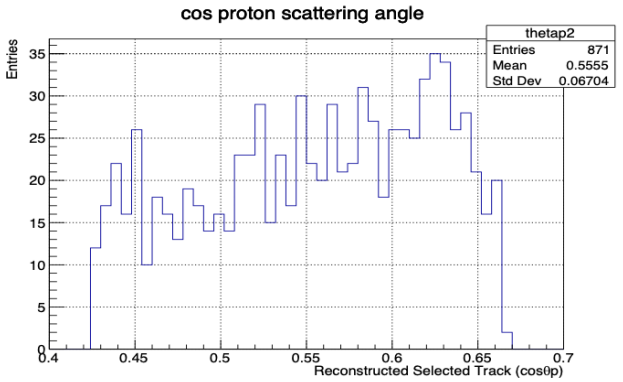

(c)

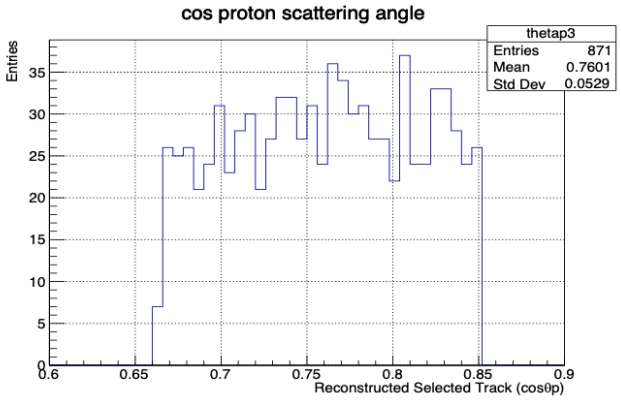

(d)

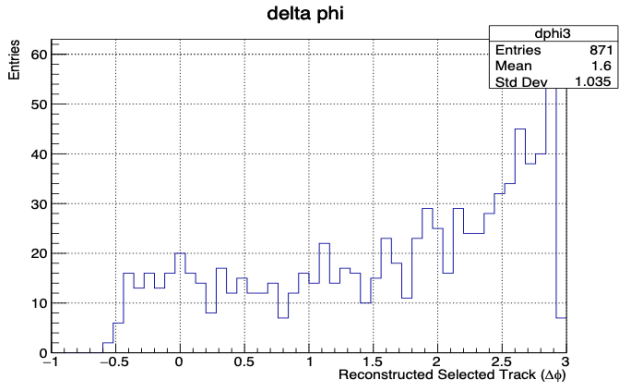

(e)

Figure B.4: Distributions of: (a) the muon kinetic energy, (b) the leading proton kinetic energy, (c) $\cos\theta_\mu$, (d) $\cos\theta_p$, and (e) the difference in the muon azimuthal angle and the leading proton azimuthal angle for selected reconstructed track for the third bin.

For the fourth bin

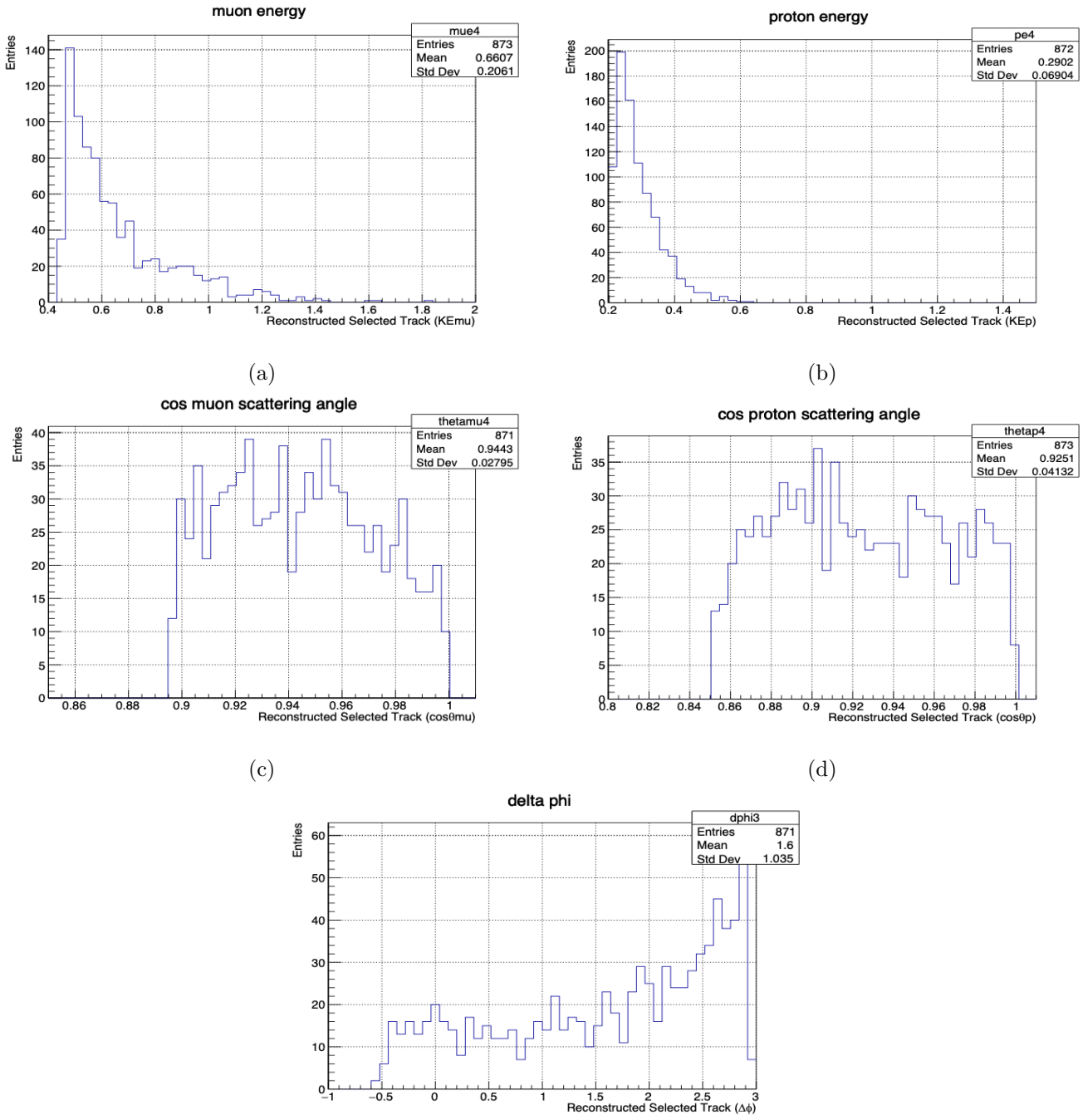

Figure B.5: Distributions of: (a) the muon kinetic energy, (b) the leading proton kinetic energy, (c) $\cos\theta_\mu$, (d) $\cos\theta_p$, and (e) the difference in the muon azimuthal angle and the leading proton azimuthal angle for selected reconstructed track for the fourth bin.

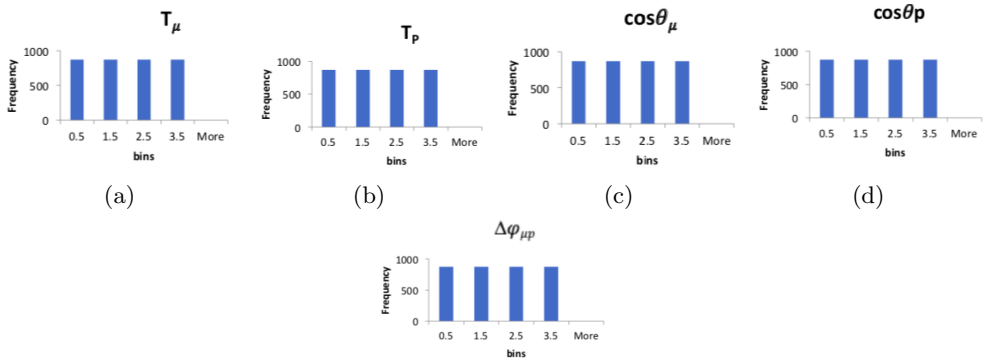

(a) (b) (c) (d)

(e)

Figure B.6: Demonstration that bins successfully to equally partition a nominal model.

(b) The second map is taking the "five vector" $[iT_\mu\ ,\ iT_p\ ,\ i\cos\theta_\mu\ ,\ i\cos\theta_p\ ,\ i\Delta\varphi_{\mu p}]$ to the "1-vector" Index as shown in Fig. B.7, indices are incremented from most significant to the least significant T_μ, T_p, $\cos\theta_p$, $\cos\theta_\mu$, and $\Delta\varphi_{\mu p}$ by using this relation

$$\begin{aligned} index = {} & 256 \times bin\left(T_\mu\right) + 64 \times bin\left(T_p\right) \\ & + 16 \times bin\left(\cos\theta_\mu\right) + 4 \times bin\left(\cos\theta_p\right) + bin\left(\left|\Delta\phi_{\mu p}\right|\right), \end{aligned}$$

Where $bin\left(x\right) = 0, 1, 2,$ or 3 is the bin index for a given variable in the 5-dimensional histogram. Then, calculating the Xindex, which is the "five object"

$$Xindex = index + 0.5. \tag{B.1}$$

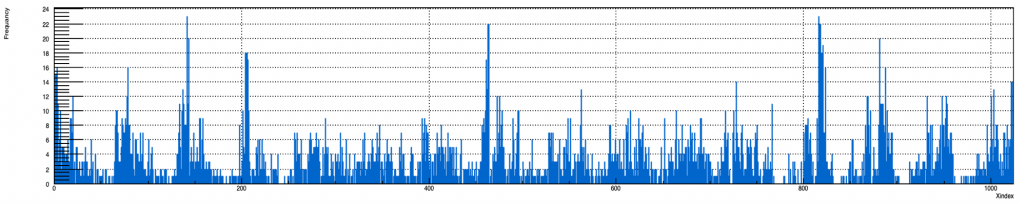

Figure B.7: The index histogram for fake data of the closure test.

Showing how well the model fits the data can be challenging in the full 5D procedure. Projection is possible, but the full distribution is "flattened" the 5D histogram into a single 1024 bin histogram.

```
NegLogLike five_log(*five_qe, *five_res, *five_dis, *five_mec, *five_x, 0.5);
```

Where $five_{qe}$, $five_{res}$, $five_{dis}$, and $five_{mec}$ represent the two maps of "QE", "RES","DIS", and "MEC" templates, respectively, while $five_x$ represents the two maps for data.

Table B.1: Bin definitions for inclusive CC proton production 5D phase space, the closure test in Tune 1.

	Bin 1	Bin 2	Bin 3	Bin 4
T_μ	[0.0, 0.2037)	[0.2037,0.3031)	[0.3031, 0.456)	[0.456, 2.0)
T_p	[0.0, 0.0953)	[0.0953,0.1487)	[0.1487,0.2137)	[0.2137, 1.5)
$\cos\theta_\mu$	[-1.0, 0.476)	[0.476, 0.749)	[0.749, 0.8972)	[0.8972, 1.0)
$\cos\theta_p$	[-1.0, 0.424)	[0.424, 0.6643)	[0.6643, 0.852)	[0.852, 1.0)
$\lvert\Delta\varphi_{\mu p}\rvert$	[-6.5, - 3.03)	[-3.03, -0.534)	[-0.534, 2.926)	[2.926, 6.5)

3. Creating a new histogram and going through each bin and filling it by just using the "predicte()" function in "NeglogLike" class

4. Calculating "χ^2"

```
double five_chi = five_plot.Chi2Test(five_x, "UU CHI2");
```

Where "UU" is experiment experiment comparison (unweighted- unweighted).

B.2 Fitting Results of the Closure Test

Table 7.8 shows the fitting result for the closure test, in this fitting result as shown in Fig. B.8, bins for which the model production is zero, are ignored, the data is usually zero for this bin as well. The overall goodness of fit is acceptable.

Figure B.9 (a) shows the 256 bin represents the lowest muon energy bin. Each group a 64 moving across the histogram in turn represent a proton energy bin. The left group of 64 bin is low energy muon plus low energy proton in the ("LEE region"). The right group of 64 bin is low energy muon with high energy protons. These are relatively high inelasticity momentum transfer events. Furthermore, each quarter of a group of 64 represents a $\cos\theta_\mu$ bin going from -1 to 1. One can see that the high T_p, low T_μ tends to have "backward muons", as would be expected.

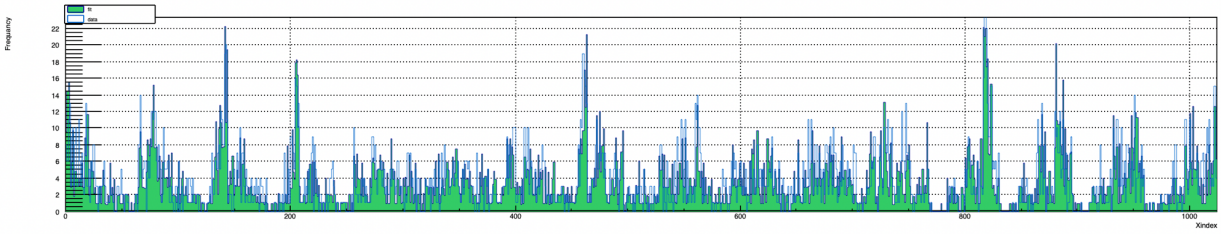

Figure B.8: The index histogram of fitting the production model of simulated QE, RES, DIS, and MEC events to fake data.

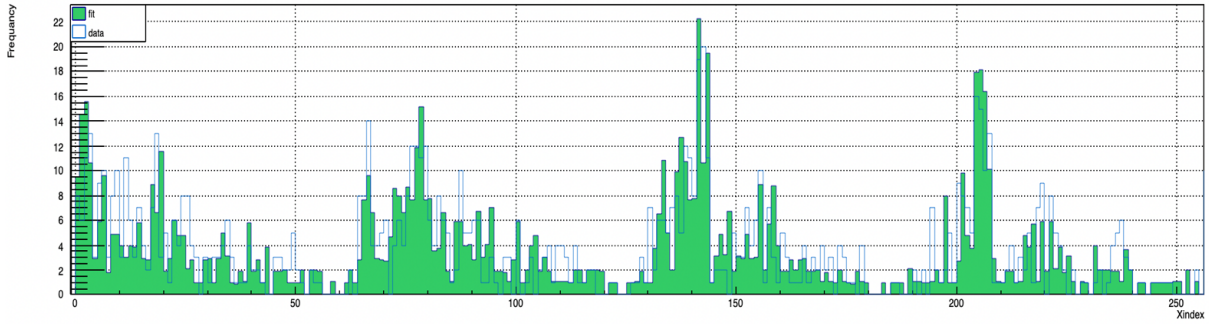

(a)

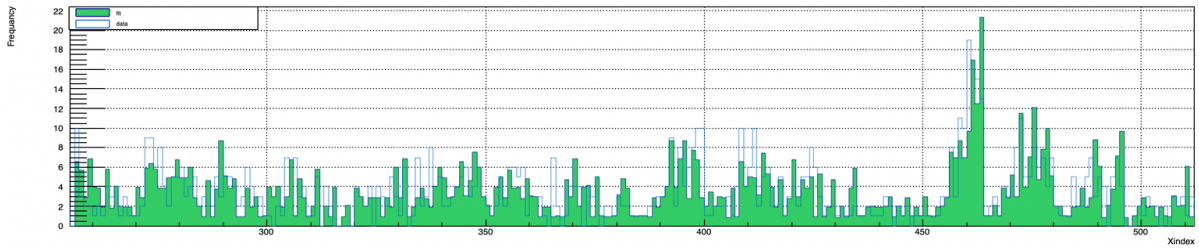

(b)

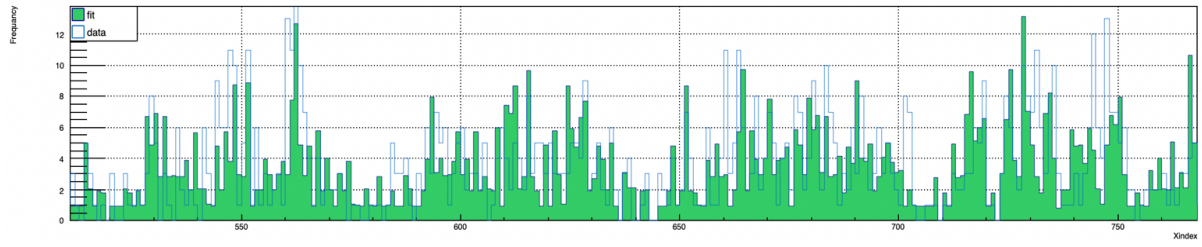

(c)

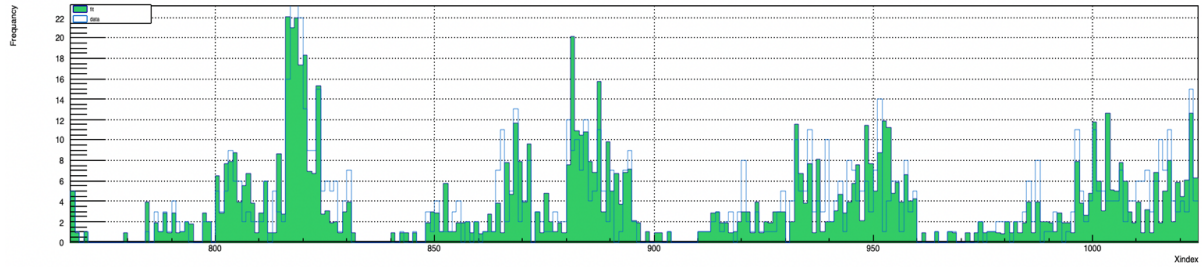

(d)

Figure B.9: The sub-histograms of fitting the production model of simulated QE, RES, DIS, and MEC events to fake data.

Interpretation of these histograms requires some practice. Each histogram has a pattern of “peaks”, “valleys”, and “deserts”. The location and relative height of the peak is determined by the cross section model convolved with the flux and detector model.

B.3 Conclusion

- The advantage of this idea will include the direct access to the underlying cross section, full use of event kinematics, and elimination of unnecessary complications from correcting for efficiency and resolution.
- The disadvantage is the model dependence and complicated systematic error studies.
- This closure test confirms the promise of the full 5D fit formalism.

Appendix C

Additional Distributions

C.1 The Acceptance and Efficiency Curve

Figure C.1 shows the acceptance curve as a function of muon kinetic energy T_μ, proton kinetic energy T_p, muon scattering angle variable $\cos\theta_\mu$, the proton scattering angle variable $\cos\theta_p$, and the difference in the muon azimuthal angle and the leading proton azimuthal angle $\Delta\phi_{\mu p}$. Fig. C.2 shows the efficiency curve as a function of muon kinetic energy T_μ, proton kinetic energy T_p, muon scattering angle variable $\cos\theta_\mu$, the proton scattering angle variable $\cos\theta_p$, and the difference in the muon azimuthal angle and the leading proton azimuthal angle $\Delta\phi_{\mu p}$.

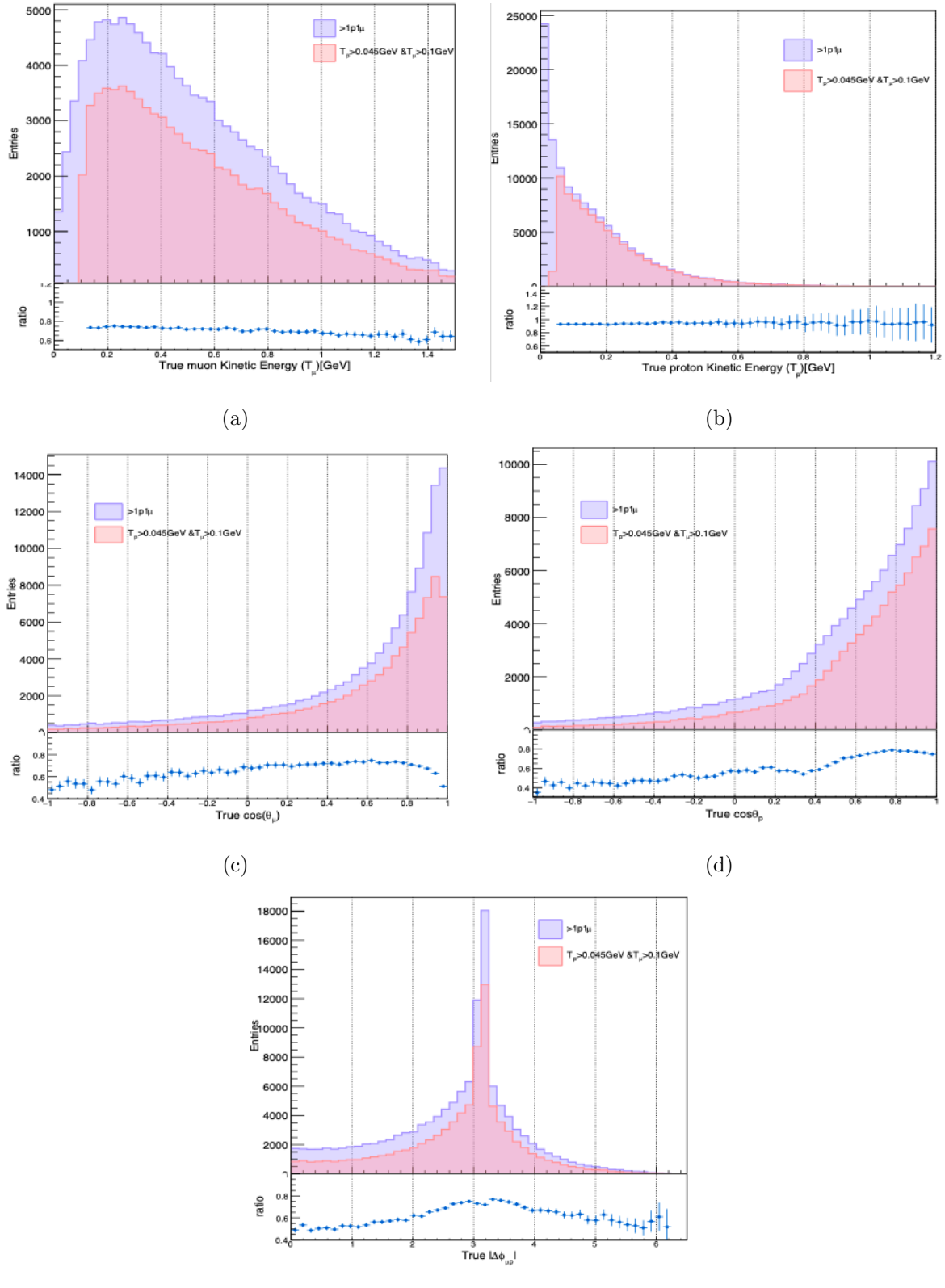

Figure C.1: Distributions and their acceptance as a function of (a) muon kinetic energy T_μ, (b) proton kinetic energy T_p, (c) muon scattering angle variable $\cos\theta_\mu$, (d) the proton scattering angle variable $\cos\theta_p$, and (e) the difference in the muon azimuthal angle and the leading proton azimuthal angle $\Delta\phi_{\mu p}$ for $> 1p\mu$ event on truth-level (red) and cut on truth-level event selection $T_\mu > 100$ MeV, $T_p > 45$ MeV (blue).

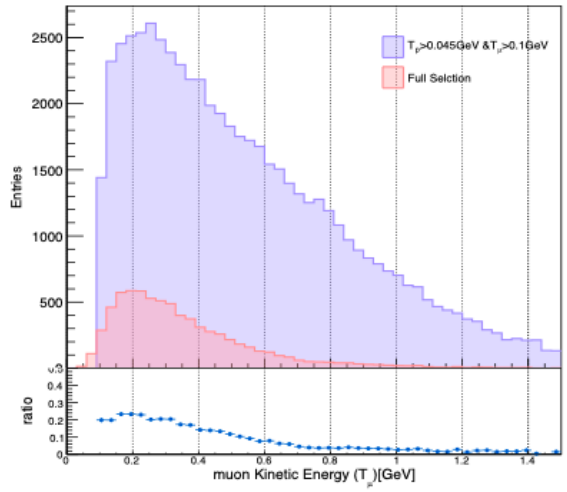

(a)

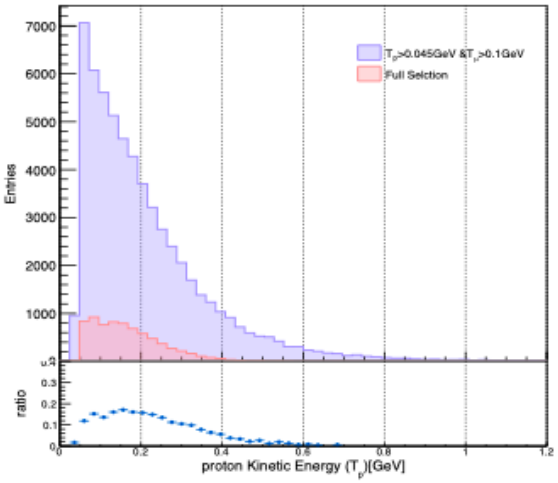

(b)

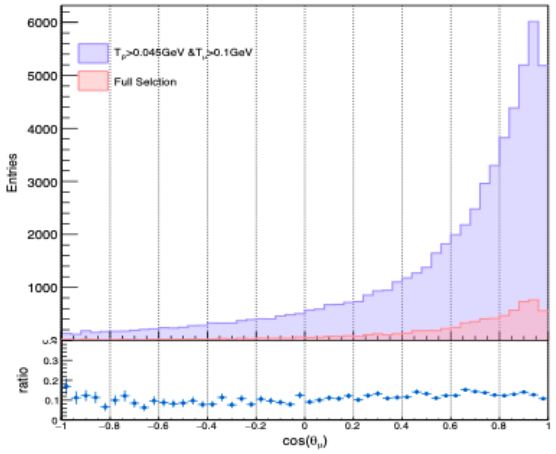

(c)

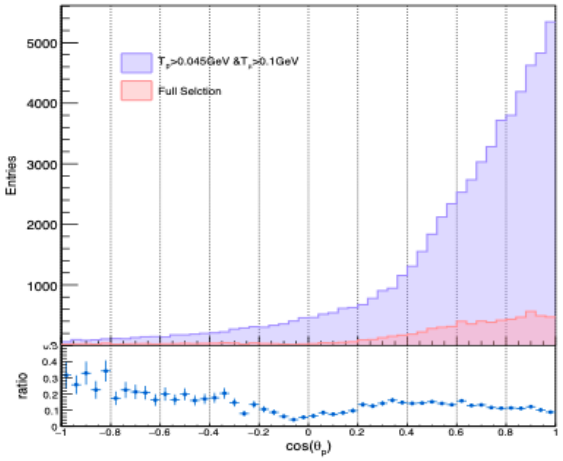

(d)

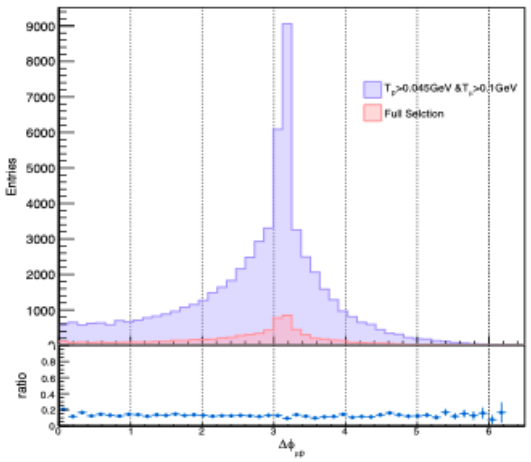

(e)

Figure C.2: Distributions and their efficiency as a function of (a) muon kinetic energy T_μ, (b) proton kinetic energy T_p, (c) muon scattering angle variable $\cos\theta_\mu$, (d) the proton scattering angle variable $\cos\theta_p$, and (e) the difference in the muon azimuthal angle and the leading proton azimuthal angle $\Delta\phi_{\mu p}$ for the event selection(red) and cut on truth-level event selection(blue).

C.2 The Effect of Removing the MEC sub-process from the Production Model

Figure C.3 shows the effect of removing a sub-process, “MEC ” from the production model, which the projections of the kinematic variables to the fitting result, which is less agreement with data than Fig. 9.2.

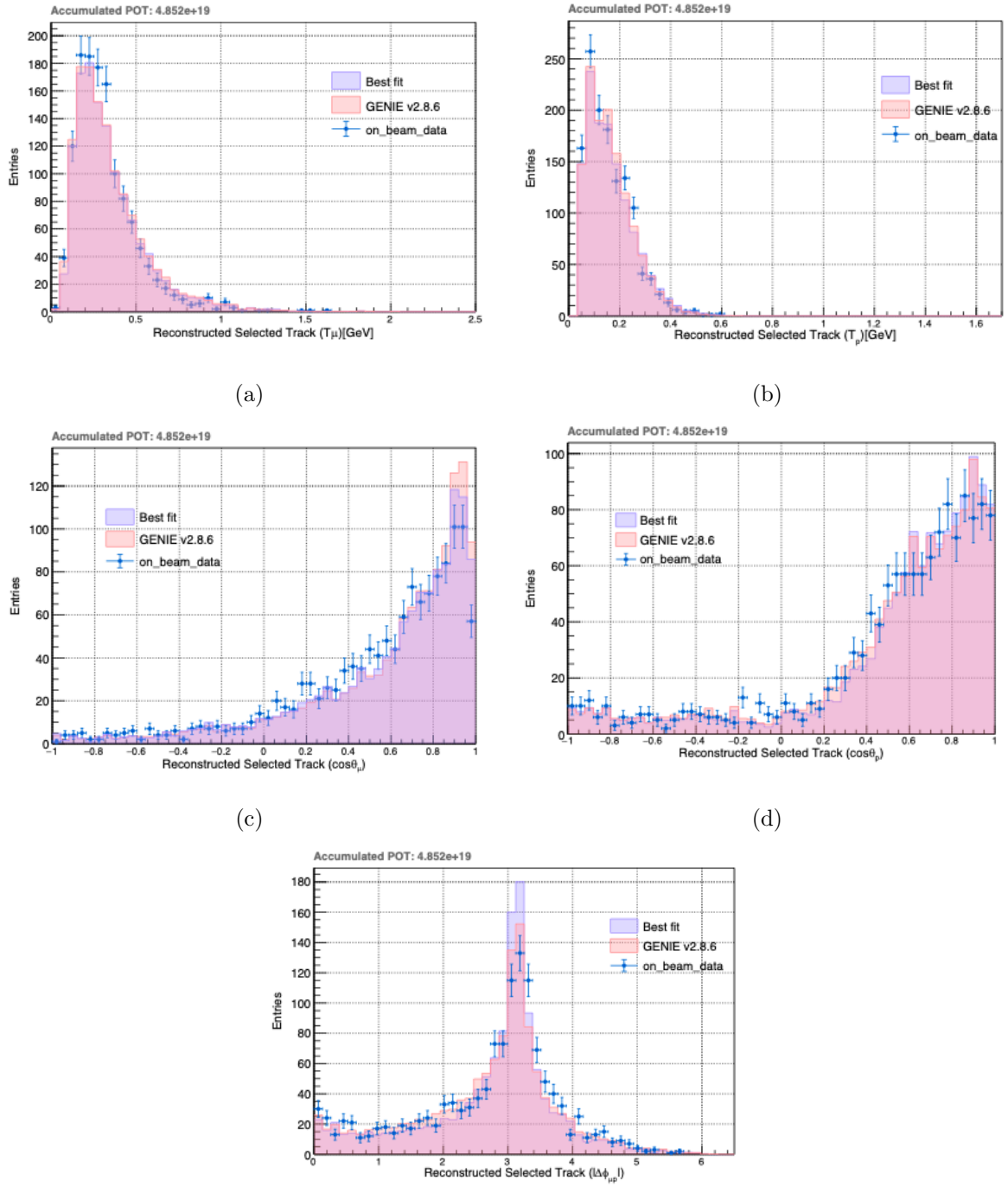

Figure C.3: Distributions of simulated just QE, RES, and DIS events (without MEC events) plus off-beam as a result of projections to fitting result to on beam data (Blue), and GENIE default (Red) in Tune 1, (a) the muon kinetic energy, (b) the leading proton kinetic energy, (c) $\cos\theta_\mu$, (d) $\cos\theta_p$, and (e) the difference in the muon azimuthal angle and the leading proton azimuthal angle for selceted reconstructed track.

C.3 Sub-process contribution to the projection of Kinematic Variables

Figures C.4 -C.5 -C.6 -C.7 -C.8 -C.9 -C.10 (a) show the distributions of some kinematic variables of simulated QE, RES, DIS, and MEC events, and (b) compare on beam data events to simulated QE, RES, DIS, and MEC events plus off-beam data.

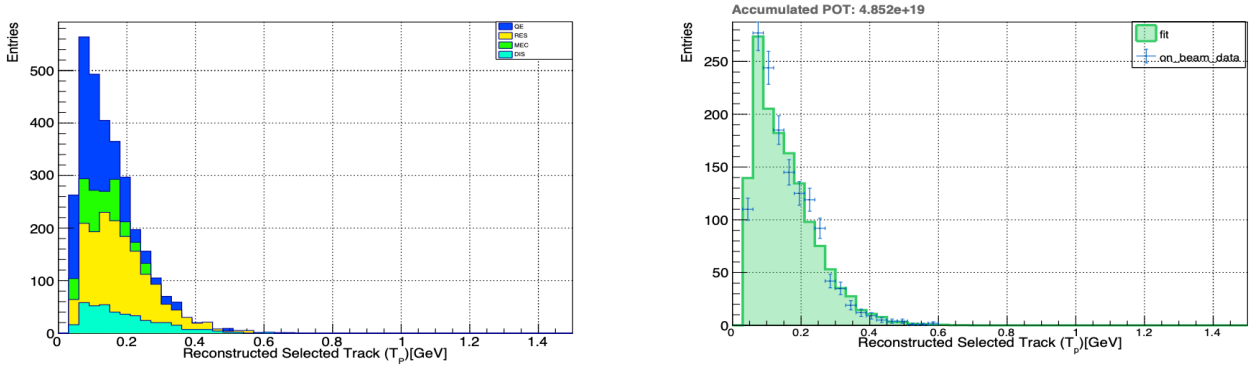

(a) (b)

Figure C.4: Distribution of the proton kinetic energy T_p for (a) simulated QE, RES, DIS, and MEC events, and (b) for the simulated events plus off-beam data and on-beam data.

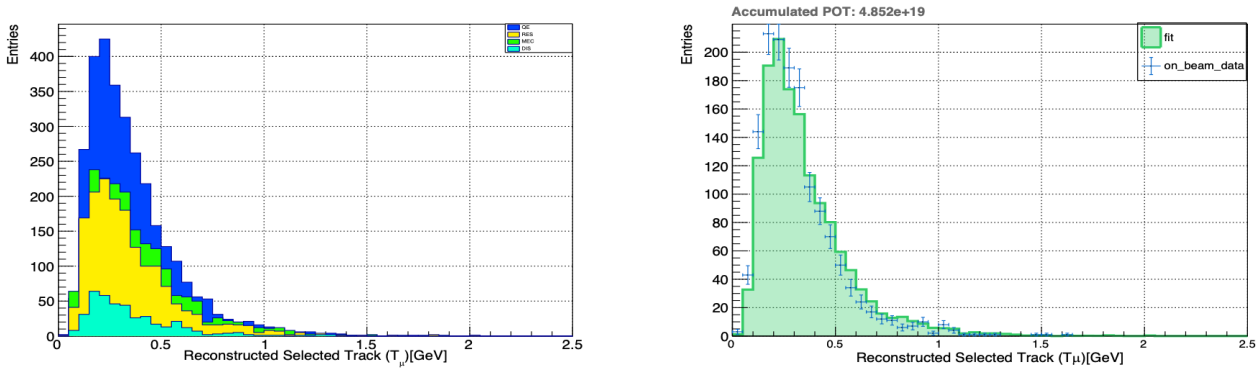

(a) (b)

Figure C.5: Distributions of the muon kinetic energy T_μ for (a) simulated QE, RES, DIS, and MEC events, and (b) for the simulated events plus off-beam data and on-beam data.

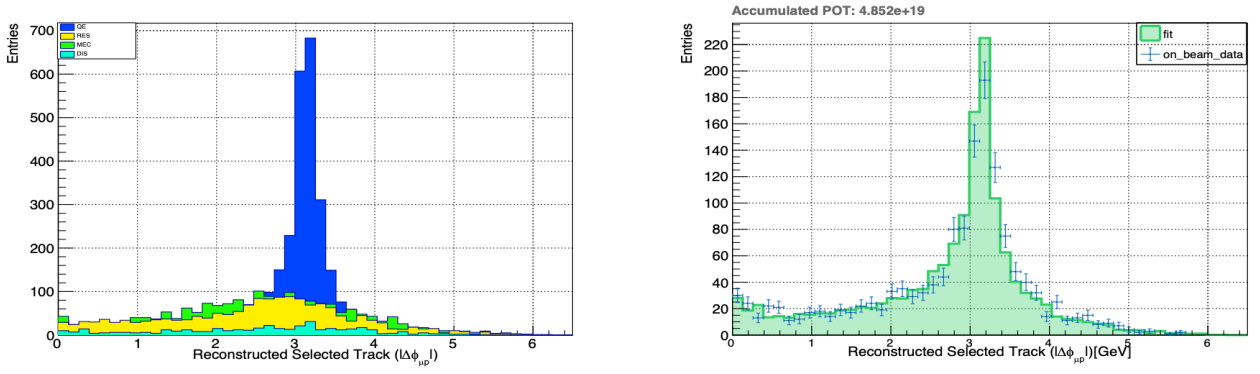

(a) (b)

Figure C.6: Distributions of the difference in the muon azimuthal angle and the leading proton azimuthal angle $\Delta\phi_{\mu p}$ for (a) simulated QE, RES, DIS, and MEC events, and (b) for the simulated events plus off-beam data with on-beam data.

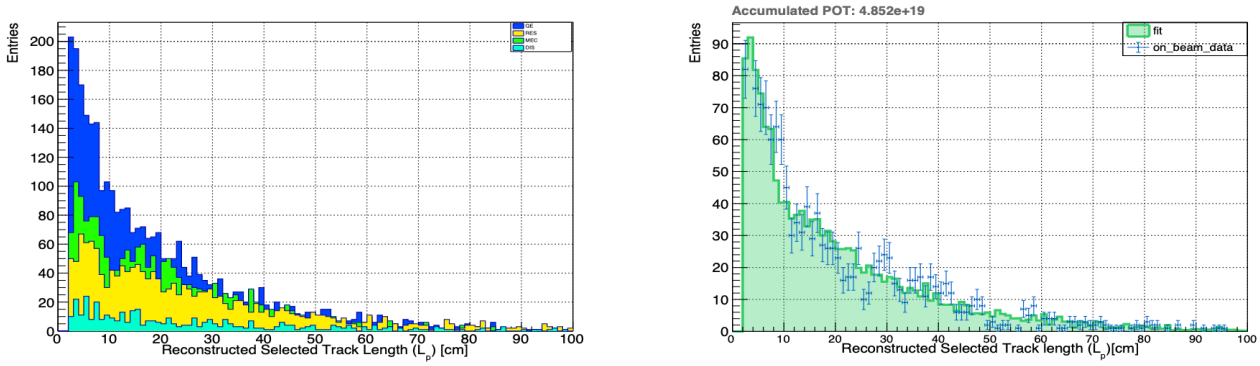

(a) (b)

Figure C.7: Distributions of the leading proton track length L_p for (a) simulated QE, RES, DIS, and MEC events, and (b) for the simulated events plus off-beam data and on-beam data.

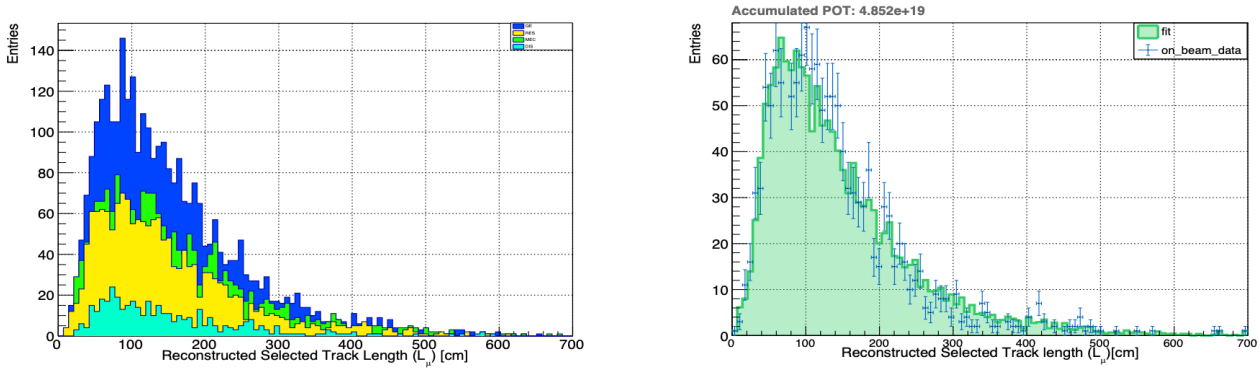

(a) (b)

Figure C.8: Distribution of the leading proton track length L_μ for (a) simulated QE, RES, DIS, and MEC events, and (b) for the simulated events plus off-beam data and on-beam data.

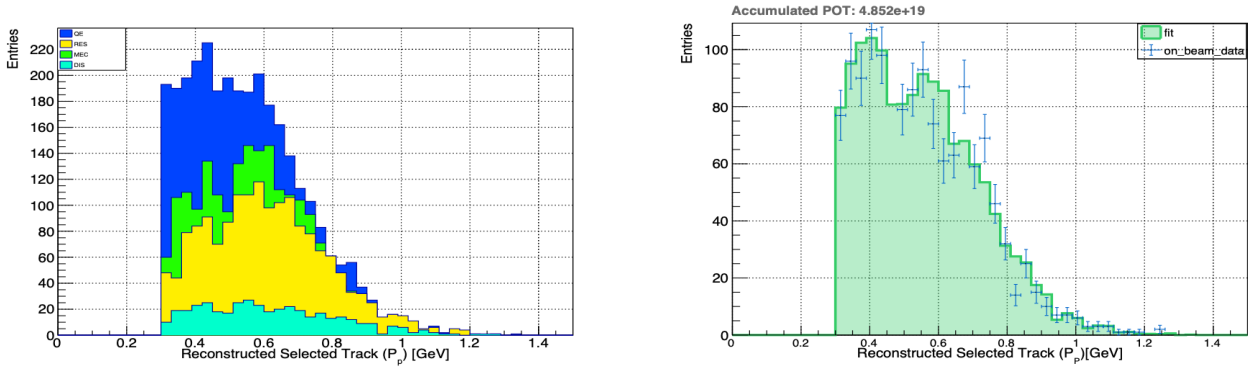

(a) (b)

Figure C.9: Distribution of the leading proton momentum P_p for (a) simulated QE, RES, DIS, and MEC events, and (b) for the simulated event plus off-beam data and on-beam data.

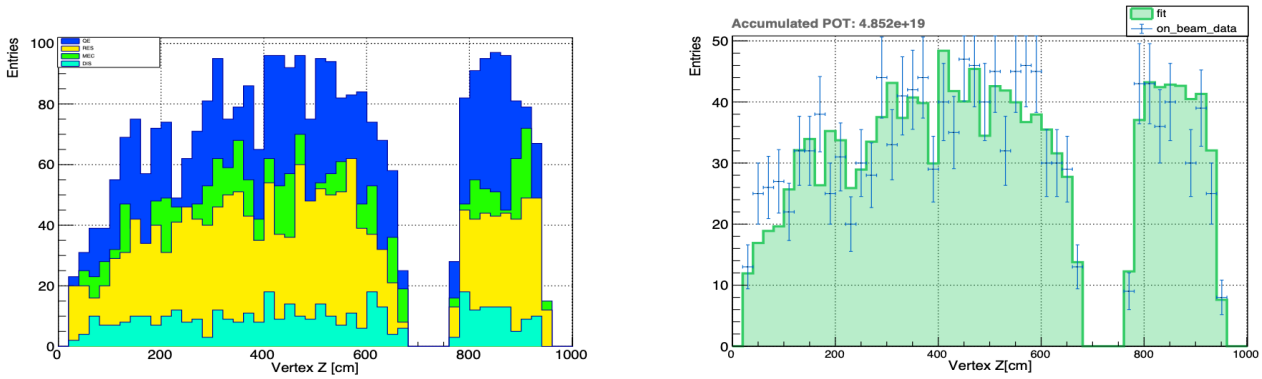

(a) (b)

Figure C.10: Distribution of Vertex Z for (a) simulated QE, RES, DIS, and MEC events, and (b) for the simulated event plus off-beam data and on-beam data.

List of Abbreviations

ArgoNeuT	Argon Neutrino Test.
ASIC	Application Specific Integrated Circuit.
BNB	Booster Neutrino Beamline.
CC	Charged Current.
CP	Conjunction Parity.
DIC	Dynamically Induced Charge.
DIS	Deep Inelastic Scattering.
DAQ	Data Acquisition system.
DIS	Deep Inelastic Scattering.
FSIs	Final State Interactions.
GEANT	GEometry ANd Tracking simulation toolkit.
DUNE	Deep Underground Neutrino Experiment.
LArTPC	Liquid Argon Time Projection Chamber.
LINAC	LINear ACcelerator machine.
MC	Monte Carlo.
MEC	Meson Exchange Current.
MicroBooNE	Micro Booster Neutrino Experiment.
MiniBooNE	Mini Booster Neutrino Experiment.
MIP	Minimum Ionizing Particles
NC	Neutral Current.
PE	Photo Electron.

PMTs	Photo Multiplier Tubes.
PMNS	Pontecorvo–Maki–Nakagawa–Sakata mixing matrix.
POT	Protons on Target.
QE	Quasi-Elastic.
RES	RESonant interaction.
RFG	relativistic Fermi gas.
RMS	Root Mean Square.
SM	Standard Model.
Super-K	Super-Kamiokande Experiment.
SNO	Sudbury Neutrino Observatory Experiment.
TPB	TetraPhenyl Butadiene.
TPC	Time Projection Chamber.